New reconstruction strategies for polyenergetic X-ray computed tomography

by

Cristóbal Martínez Sánchez

A dissertation submitted by in partial fulfillment of the requirements for the degree of Doctor of Philosophy in

Multimedia and communications interuniversity PhD program

Universidad Carlos III de Madrid

Advisors:

Mónica Abella García
Manuel Desco Menéndez

Tutor:

Mónica Abella García

October 2021

This thesis is distributed under license “Creative Commons **Atributtion - Non Commercial - Non Derivatives**”.

A mis padres

Acknowledgements

En primer lugar, quería agradecer a mi directora de tesis, Mónica, por confiar en mí todo este tiempo, por su ayuda durante la realización de esta tesis y por intentar contagiarme la capacidad para fijarse en los detalles más nimios. Gracias también a mi director de tesis, Manolo, por sus consejos y su oportunidad para trabajar en este gran grupo.

Gracias a Javi (informático) por todo el soporte que nos ha dado, tanto con el uso de sus servidores como los infinitos cambios en FUX-sim y Raptor.

Thanks to Professor Fessler and Professor Chan, for giving me the opportunity to work in their laboratories and being so nice with me.

Gracias a todas las generaciones del equipo de rayos X desde el primero con Claudia, Inés, Álvaro, Ramón y Alba hasta el último con Patri, Nik, Ale, Carlos, Agustín y Aída, pasando por Manuel, Paco (Aarón), Alejandro del Valle y Nerea. Sin su apoyo no hubiera sido capaz de realizar esta tesis.

Gracias al resto del pasillo del BiiG: Estibaliz, David Pérez, David García, Mónica García, Rafa; a los técnicos de abajo: Guille, Ángelica y Miguel; y a los compañeros del hospital: Sandra, Yolanda, Dani, Trajana, Mario, María, Bea, Esther, Jorge, etc.

Gracias a mi familia, en especial a mis padres que siempre me han dado la libertad de seguir el camino que quisiera. A mis hermanos, Iñaki, por enseñarme el camino de la ciencia, y Ana, por aguantarme durante tanto tiempo en Madrid. A mis abuelas, tías y primos.

Gracias a Carmen por aguantar las noches que me he pasado en vela, por los "repásame este abstract a ver si está bien el inglés, por los "no puedo limpiar ni hacer la cena, hazlo tú por favor", por los nervios y los agobios, etc. Esta tesis también tiene tu impronta.

Gracias al resto de personas que también han estado a mi lado: Martín, Ramírez, Carlitos, Avis, Mafias, De la Torre, Rizo, Deocal, Sergio, Ramón Salcedo, Charli Martinez, Juan Ignacio, Eloy, Roy, Moreno etc.

Espero que no olvidarme de nadie, pero si alguién lo echa en falta, está intrinsecamente agradecido.

Published and submitted content

Journal articles

1. Abella M.*, Martínez C.*, Vaquero JJ, Desco M., Fessler JA. *Simplified Statistical Image Reconstruction for X-ray CT with Beam-Hardening Artifact Compensation.* IEEE Transactions on Medical Imaging. 2019. Impact Factor: 6.685 (Q1). DOI: https://doi.org/10.1109/tmi.2019.2921929.

    - Author contributions: Cristóbal Martínez was responsible for software development, data acquisition, data analysis, and writing the paper.
    - Contribution partially included in chapter 3, 4 and 6.

2. Martínez C.*, De Molina C.*, Desco M., Abella M. *Optimization of a calibration protocol for quantitative radiography.* Medical Physics. 2021. Impact Factor: 4.071 (Q1). DOI: https://doi.org/10.1002/mp.14638.

    - Author contributions: Cristóbal Martínez was responsible for software development, data acquisition, data analysis, and writing the paper. * denotes that authors contributed equally to this work.
    - Contribution partially included in chapter 3, 4 and 6.

3. Abella M.*, Martínez C.*, Garcia I., Moreno P., De Molina C., Desco, M. *Tolerance to geometrical inaccuracies in CBCT systems: A comprehensive Study.* Medical Physics. Impact Factor: 4.071 (Q1). DOI: https://doi.org/10.1002/mp.15065.

    - Author contributions: Cristóbal Martínez was responsible for software development, data creation, data analysis, and writing the paper. * denotes that authors contributed equally to this work.
    - Contribution partially included in chapter 1.

4. Martínez C., Fessler JA., Desco M., Abella M. *Simple Beam-Hardening Correction Method (2DLinBH) based on 2D linearization.* Submitted to Physics in Medicine & Biology. 2021. Impact Factor: 3.609 (Q2).

- Author contributions: Cristóbal Martínez was responsible for software development, data acquisition, data analysis, and writing the paper. * denotes that authors contributed equally to this work.
- Contribution partially included in chapter 3, 4 and 6.

Conference proceedings

1. Martínez C., de Molina C., Desco M., Abella M. *Simple method for beam-hardening correction based on a 2D linearization function*. 4th International Conference on Image Formation in X-Ray Computed Tomography, Bamberg, Germany, July, 2016. Poster.

   - Author contributions: Cristóbal Martínez was responsible for software development, data acquisition, data analysis, and writing the paper.
   - Contribution partially included in chapter 3.

2. Martínez C., de Molina C., Desco M., Abella M. *Calibration free method for beam hardening compensation: preliminary results*. 2017 IEEE Nuclear Science Symposium and Medical Imaging Conference, Atlanta, USA. Poster.

   DOI: https://doi.org/10.1109/NSSMIC.2017.8532863.

   - Author contributions: Cristóbal Martínez was responsible for software development, data acquisition, data analysis, and writing the paper.
   - Contribution partially included in chapter 3.

3. Martínez C., Fessler JA., Desco M., Abella M. *Statistical image reconstruction with sample-based beam-hardening compensation for X-ray CT*. Proc. 5th International Conference on Image Formation in X-ray CT, pp. 11-4, 2018. Oral Communication.

   - Author contributions: Cristóbal Martínez was responsible for software development, data acquisition, data analysis, and writing the paper.
   - Contribution partially included in chapter 3.

4. Martínez C., Fessler JA., Desco M., Abella M. *Segmentation-free statistical method for polyenergetic X-ray computed tomography with a calibration step*. 6th International Conference on Image Formation in X-ray CT. 2020. Poster.

   - Author contributions: Cristóbal Martínez was responsible for software development, data acquisition, data analysis, and writing the paper.
   - Contribution partially included in chapter 3.

5. Martínez C., Del Cerro CF., Desco M., Abella M. *New method for correcting beam-hardening artifacts in CT images via deep learning.* 16th Virtual International Meeting on Fully 3D Image Reconstruction in Radiology and Nuclear Medicine. 2021. Poster. Fully 3D Award nominee.

    - Author contributions: Cristóbal Martínez was responsible for software development, data acquisition, data analysis, and writing the paper.
    - Contribution partially included in chapter 3 and 5.

6. Martínez C., Ballesteros N., de Molina C., Desco M., Abella M. *Corrección del efecto de endurecimiento basado en una linealización 2D*. 2018. XXXV Congreso Anual de la Sociedad Española de Ingeniería Biomédica (CASEIB). Oral communication.

    - Author contributions: Cristóbal Martínez was responsible for software development, data acquisition, data analysis, and writing the paper.
    - Contribution partially included in chapter 3 and 5.

7. Martínez C., Sakaltras N., Desco M., Abella M. *Método para la corrección de radiación dispersa a través de un beam-stopper en radiografía plana.* 2018. XXXVI Congreso Anual de la Sociedad Española de Ingeniería Biomédica (CASEIB). Oral Communication.

    - Author contributions: Cristóbal Martínez was responsible for software development, data acquisition, data analysis, and writing the paper.
    - Contribution partially included in chapter 3 and 5.

8. Martínez C., de Molina C., Desco M., Abella M. *Free calibration method for beam hardening correction in small animal studies*. 1st young Spanish Molecular Imaging Network. Poster.

    - Author contributions: Cristóbal Martínez was responsible for software development, data acquisition, data analysis, and writing the paper.
    - Contribution partially included in chapter 3 and 5.

9. Martínez C., de Molina C., Desco M., Abella M. *Recovering density values on small animal X-ray imaging through beam hardening compensation: preliminary results*.European Molecular Imaging Meeting - EMIM 2018. Poster.

    - Author contributions: Cristóbal Martínez was responsible for software development, data acquisition, data analysis, and writing the paper.
    - Contribution partially included in chapter 3 and 5.

10. Martínez C., Ballesteros N., de Molina C., Desco M., Abella M. *Calibration free method for beam hardening compensation: preliminary results*. 2nd young Spanish Molecular Imaging Network. 2018. Poster.

    - Author contributions: Cristóbal Martínez was responsible for software development, data acquisition, data analysis, and writing the paper.
    - Contribution partially included in chapter 3 and 5.

11. Martínez C., Desco M., Abella M. *New simple statistical method with beam-hardening correction for quantitative image in preclinical*. European Molecular Imaging Meeting - EMIM 2020. Poster. Best poster award in the session.

    - Author contributions: Cristóbal Martínez was responsible for software development, data acquisition, data analysis, and writing the paper.
    - Contribution partially included in chapter 3 and 5.

12. Martínez C., de Molina C., Desco M., Abella M. *Corrección empírica del artefacto de endurecimiento de haz exento de calibración*. XXXIV Congreso Anual de la Sociedad Española de Ingeniería Biomédica (CASEIB). Oral communication.

    - Author contributions: Cristóbal Martínez was responsible for software development, data acquisition, data analysis, and writing the paper.
    - Contribution partially included in chapter 3 and 5.

13. Martínez C., Del Cerro CF., Desco M., Abella M. *Nuevo método para la obtención de imágenes TAC libres de endurecimiento de haz vía aprendizaje automático*. 2020. XXXVIII Congreso Anual de la Sociedad Española de Ingeniería Biomédica (CASEIB). Oral communication.

    - Author contributions: Cristóbal Martínez was responsible for software development, data acquisition, data analysis, and writing the paper.
    - Contribution partially included in chapter 3 and 5.

Transfer to the industry

All the proposed method have been incorporated in the new prototypes of a high resolution micro-CT scanner for small-animal and a prototype of a C-arm in veterinary imaging.

Other research merits

Conference proceedings

1. Martínez A., Polo R. de Molina C., Martinez C., Blas JG, Desco M. *X-Ray Scatter Correction Method for Planar Radiography Based on a Beam Stopper: a Simulation Study*. 2016 IEEE Nuclear Science Symposium and Medical Imaging Conference. Poster.

2. Sakaltras N., Tovar FA, Martínez C., Del Cerro CF., Desco M., Abella M. Proc. *Compensacion de radiación dispersa en radiografía digital a través del aprendizaje automático: resultados preliminares.* XXXVIII Congreso Anual de la Sociedad Española de Ingeniería Biomédica (CASEIB). 2020. Oral communication.

Abstracts

1. de Molina C., Martínez C., Desco M., Abella M. *Calibration set-up for Dual Energy capabilities in a Real Digital Radiography System*. 1st young Spanish Molecular Imaging Network. Poster.

2. Martínez A., Martínez C., Desco M., Abella M. *X-Ray scatter correction in 2D radiography using a beam-stopper: a simulation study*. European Molecular Imaging Meeting - EMIM 2018. Poster. Best poster award in the session.

Research projects

- **RADCOV19: Nuevo sistema de diagnósitico radiológico pulmonar para COVID-19.**
  FONDO SUPERA COVID-19 - RADCOV19.
  IP: Mónica Abella García.
  CRUE Universidades, CSIC and Banco Santander (Fondo Supera).

- **Reconstrucción tomográfica para sistemas de rayos X de baja dosis mediante aprendizaje automático y dispositivos gráficos.**
  DEEPCT-CM-UC3M.

IP: Mónica Abella García, Francisco Javier Garcia Blas.
Universidad Carlos III de Madrid

- **Obtención de imagen 3D con sistemas de tomografía de rayos X y sistemas de arco en C.**
  2018/00169/001.
  IP: Mónica Abella García .
  Fundación para la Investigación Biomédica del Hospital Gregorio Marañón. 34.000 €

- **Nuevo sistema de tomografía por rayos X portátil.**
  DTS17/00122.
  IP: Manuel Desco Menéndez.
  Instituto de Salud Carlos III, 84.920 €.

- **Nuevos escenarios de tomografía por rayos X (NEXT).**
  DPI2016-79075-R.
  IP: Mónica Abella Garcia.
  Ministerio de Economía, Industria y Competitividad. (Universidad Carlos III de Madrid). 147.620 €.

- **Evaluación de protocolos de adquisición para un nuevo sistema de rayos X multipropósito.**
  2017/00550/001 .
  IP: Mónica Abella García y Francisco Javier García Blas.
  Financiado por la entidad Sociedad Española de Electromedicina Calidad S.A. 14.900 €.

- **Avances en Imagen Radiológica (AIR).**
  TEC2013-47270-R.
  IP: Mónica Abella Garcia and Manuel Desco Menéndez.
  Ministerio de Economía y Competitividad. 160.204 €.

Abstract

X-ray computed tomography (CT) provides a 3D representation of the attenuation coefficients of patient tissues, which are roughly decreasing functions of energy in the usual range of energies used in clinical and preclinical scenarios (from 30 KeV to 150 KeV). Commercial scanners use polychromatic sources, producing a beam having a range of photon energies, because no X-ray lasers exist as a usable alternative. Due to the energy dependence of the attenuation coefficients, low-energy photons are preferably absorbed, causing a shift of the mean energy of the X-ray beam to higher values; this effect is known as beam hardening. Classical reconstruction methods assume a monochromatic source and do not take into account the polychromatic nature of the spectrum, producing two artifacts in the reconstructed image: 1) cupping in large homogeneous areas and 2) dark bands between dense objects such as bone. These artifacts hinder a correct visualization of the image and the recovery of the true attenuation coefficient values.

A fast correction of the beam-hardening artifacts can be performed with the so-called post-processing methods, which use the information of a segmentation obtained in a preliminary reconstruction. Nevertheless, this segmentation may fail in low-dose scenarios, leading to an increase of the artifacts. An alternative for these scenarios is the use of iterative methods that incorporate a beam-hardening model, at a cost of higher of computational time compared to post-processing methods. All previously proposed methods require either knowledge of the X-ray spectrum, which is not always available, or the heuristic selection of some parameters, which have been shown not to be optimal for the correction of different slices in heterogeneous studies.

This thesis is framed in a research line focused on improving radiology systems of the Biomedical Imaging and Instrumentation Group (BiiG) from the Bioengineering and Aerospace Department of Universidad Carlos III de Madrid. This research line is carried out in collaboration with the Unidad de Medicina y Cirugía experimental of Hospital Gregorio Marañón through Instituto de Investigación Sanitaria Gregorio Marañón, the Electrical Engineering and Computer Science (EECS) department of the University of Michigan and SEDECAL, a Spanish company among the ten best world companies in medical imaging that exports medical devices to 130 countries. As part of this research line, a high-resolution micro-CT was developed for small-animal samples, which operates

at low voltages, leading to strong beam-hardening artifacts. This scanner allows preclinical studies to be carried out, which can be divided into cross-sectional and longitudinal studies. Since cross-sectional studies consist of one acquisition at a specific point in time, radiation dose is not an issue, allowing for the use of standard-dose protocols with good image quality. In contrast, longitudinal studies consist of several acquisitions over time, so it is advisable to use low-dose protocols, despite the reduction of signal to noise ratio and the risk of artifacts in the image. This thesis presents a bundle of reconstruction strategies to cope with the beam-hardening effect in different dose scenarios, overcoming the problems of methods previously proposed in the literature.

Since image quality is not an issue in the standard-dose scenarios, the speed of the strategies becomes a priority, advising for post-processing strategies. The main advantage of the proposed post-processing strategy is the inclusion of empirical models of the beam-hardening effect, either through a simple calibration phantom or through the information provided by the sample, which eliminates the need of the knowledge of the spectrum or tunning parameters. The evaluation against previously proposed correction methods with real and simulated data showed a good artifact compensation for a standard-dose scenario (cross-sectional studies), while not optimum in a low-dose scenario, as expected. For longitudinal studies, where the reduction of dose delivered to the sample is advisable, this thesis presents an iterative method that incorporates the mentioned experimental beam-hardening models. The evaluation with real and simulated data and different dose scenarios showed excellent results but with the known drawback of high computational time. Finally, a deep-learning approach was explored with the idea of looking for a joint solution that would require low-computational time and, at the same time, compensate the beam-hardening artifacts regardless the dose scenario. The chosen architecture is U-net++, based on an encoder-decoder, with the mean-squared error as the cost function. Results in real data showed a good compensation of the beam-hardening and low-dose artifacts with a considerable reduction of time, rising the interest of further exploring this path in the future.

The incorporation of these reconstruction strategies in real scanners is straightforward, only requiring a small modification of the calibration step already implemented in commercial scanners. The methods are being transferred to the company SEDECAL for their implementation in the new generation of micro-CT scanners for preclinical research and a multipurpose C-arm for veterinary applications.

Contents

List of Figures

List of Tables

Chapter 1

Motivation and context of the thesis

The medical imaging modality used nowadays for more than 55% is Radiography, despite its two main limitations: (1) being a projection image, the tissues are shown overlapped with no depth information of the different structures and masking of low-density structures behind the bones; and (2), it is a non-quantitative image, so we can see the shape but no the exact density of the tissues. These problems are solved by Computed Tomography (CT), introduced by Cormack [1] and Hounsfield [2], which enables to obtain a 3D representation of the tissue attenuation properties. In addition to its clinical applications in human studies, CT is widely used in animal imaging for preclinical research. One of the disadvantages of CT is the increase of ionizing radiation dose delivered to the sample due to the need of acquiring several radiographs around the patient or the animal.

Commercial scanners use polychromatic sources, producing a beam having a range of photon energies, because no X-ray lasers exist as a usable alternative. Due to the energy dependence of the attenuation coefficients, low-energy photons are preferably absorbed, causing a shift of the mean energy of the X-ray beam to higher values; this effect is known as beam hardening. Since attenuation coefficients are energy dependent, different projection measurements will 'see' the same object as having different attenuation values, leading to data inconsistencies in the Radon sense. Classical reconstruction methods assume a monochromatic source and do not take into account the polychromatic nature of the spectrum, producing two artifacts in the reconstructed image that hinder quantitative values: 'cupping' in homogeneous areas (Figure 1.1, top) and 'dark bands' or 'shadows' between bones (Figure 1.1, bottom).

Several strategies can be found in the literature to compensate for the beam-hardening effect. Physical filters are generally used to pre-harden the beam before reaching the sample, but this is not enough to remove the artifacts. Another method, implemented in most commercial scanners, is the water-linearization, which models the object as homogeneous and corrects only the cupping artifact [4]. To correct both cupping and dark bands, post-processing methods generally model the object as composed of soft tissue and

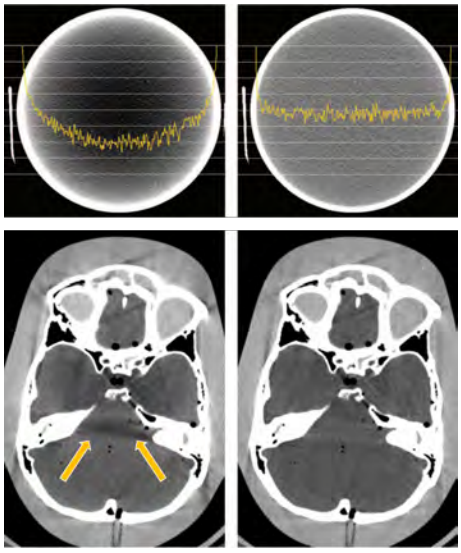

Figure 1.1: Top: Cylinder phantom with (left) and without (right) cupping artifact. Bottom: Head acquisition with (left) and without (right) dark band artifacts. Source: [3].

bone, which are segmented in a preliminary reconstruction. Many methods use this information and the knowledge of the spectrum to analytically calculate the corresponding monochromatic projections and produce an image free of artifacts [5, 6]. Nevertheless, the characterization of the spectrum is not infrequently available. To avoid the need for the knowledge of the spectrum, the beam-hardening effect can be approximated with a polynomial model that linearly combines the attenuation produced by the soft tissue and bone traversed [6, 7, 8]. However, this polynomial model does not completely characterize the beam-hardening effect of the sample and may produce a suboptimal correction in volumes with different combinations of bone and soft tissue.

The current trend in X-ray imaging is to reduce the dose to the patient following the ALARA (As Low As Reasonably Achievable) principle. The main strategies are based on 1) the reduction of the photons and 2) the reduction of projections. Nevertheless, the former decreases the signal to noise ratio and the latter generates the so-called streak artifacts in the reconstructed images. These artifacts and noise hinder the separation of the tissues in the segmentation step of post-processing methods, which may result in a suboptimal model. Iterative reconstruction methods are a good alternative to deal with these low-dose studies since they can incorporate a model of the noise and a regularization term to deal with the streaks. We can find in the literature iterative methods that incorporate a model of the polychromatic source to also account for the beam-hardening effect. However, the polychromatic model proposed in these methods is generally based on the knowledge of the spectrum [9, 10, 11] or a polynomial approximation, which may lead to nonphysical negative values [12].

Computational time for iterative methods is high compared to analytical reconstruc-

tion methods followed by post-processing corrections. One possible alternative is the use of Deep-Learning (DL) approaches [13, 14, 15] to obtain a joint solution that would require low-computational time and, at the same time, compensate the beam-hardening artifacts regardless the dose scenario. As far as we know, there is only one work in the literature attempting to use DL to correct the beam-hardening artifacts [16]. However, the high complexity of the proposed architecture limits the volume size due to memory constraints, hindering its use in clinical and preclinical applications.

The work of this thesis is framed in a research line of the Biomedical Imaging and Instrumentation Group (BiiG) from the Bioengineering and Aerospace Department of *Universidad Carlos III de Madrid* in collaboration with the *Hospital General Universitario Gregorio Marañón* through the *Instituto de Investigación Sanitaria Gregorio Marañón*. This research line is focused on the improvement of radiology systems, covering from the design of the system and the optimization of the acquisition to the final reconstructed image. As part of this research line, a high resolution micro-CT was developed for small-animal samples [17] (see Figure 1.2, left), currently commercialized by the Sociedad Española de Electromedicina y Calidad S.A. (SEDECAL). Since this scanner is focused on small animals, the range of energies is low compared to that in clinical studies, which leads to strong beam-hardening artifacts (see Figure 1.2, center and right). This scanner allows preclinical research to be carried out, which make use of cross-sectional and longitudinal studies. Cross-sectional studies consist of one acquisition at a specific point in time, thus, radiation dose is not an issue and allows the use of standard-dose protocols. These data have good image quality, which enable the use of post-processing correction methods. In contrast, since longitudinal studies consist of several acquisitions over time, it is advisable to use low-dose protocols prone to noise and artifacts. In this case, iterative methods deal with the noise and artifacts at the expense of high computational time. Alternatively, it would be interesting to find a single reconstruction strategy that combined the speed of the post-processing methods with the robustness against noise of the iterative methods, which could be addressed with Deep Learning.

Part of the work included in this thesis was carried out in collaboration with Professor Jeffrey A. Fessler from EECS department at University of Michigan. This collaboration, including a four-month visit, is currently continuing for the completion of three pending joint publications.

1.1 Objectives

The general objective of this thesis is the research of a bundle of new reconstruction strategies that incorporate beam-hardening compensation for the different acquisition protocols used in a preclinical CT scanner (standard and low-dose scenarios), overcoming the limi-

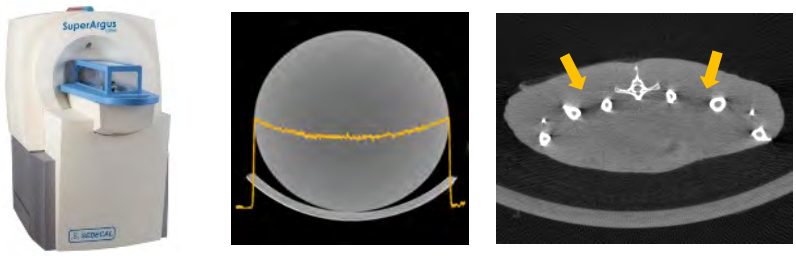

Figure 1.2: Left: ARGUS-CT developed by the SEDECAL company. Center and right: Cupping and dark bands artifacts in images acquired with the ARGUS-CT scanner.

tations found in previous literature. The specific objectives are:

- Research and development of a fast reconstruction strategy with beam-hardening compensation for standard-dose scenarios.
- Research and development of a reconstruction strategy with beam-hardening compensation able to cope with noise and streaks present in low-dose scenarios.
- Exploration of the use of a Deep-Learning approach to obtain a single fast reconstruction strategy with beam-hardening compensation optimum for both standard and low-dose scenarios.
- Validation of the proposed reconstruction strategies on simulated data and rodent data acquired with a preclinical scanner under standard and low-dose conditions.

1.2 Thesis outline

The document is comprised of eight chapters:

- Chapter 1 presents the motivation, the objectives and the outline of the manuscript.
- Chapter 2 presents an introduction to X-ray image reconstruction and Deep Learning.
- Chapter 3, after a review of the literature, describes the proposed reconstruction strategies with beam-hardening compensation. It is divided into three sections: (1) strategies for standard-dose scenarios, based on analytical reconstruction followed by post-processing, (2) strategies for low-dose scenarios, based on iterative reconstruction, and (3) a Deep-Learning approach valid for both standard and low-dose scenarios.
- Chapter 4 describes the methodology followed to evaluate the proposed method and the implementation of previously proposed methods used for comparison.

- Chapter 5 presents the results in simulated and real data for the two different scenarios.
- Chapter 6 presents the discussion, conclusions, and future work.

Chapter 2

Background[1]

This chapter explains the basic concepts of X-ray reconstruction and introduces the main concepts of Deep Learning.

2.1 X-ray tomography reconstruction

Tomographic imaging produces a 3D image from radiographs acquired around the sample where each voxel of the volume represents the attenuation coefficient of the tissues. The problem consists of the estimation of the image from the projections. Many schemes have been proposed to solve this problem in the literature and, depending on the approach, they can be divided into analytical and iterative methods (Figure 2.1)

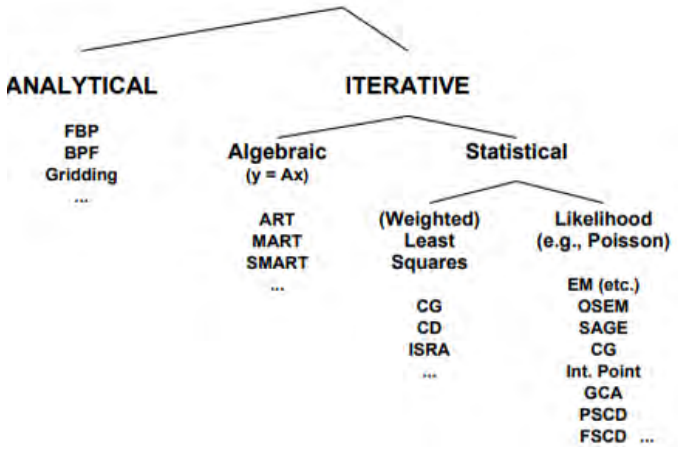

Figure 2.1: Types of reconstruction algorithm. Source: [19]

[1]Part of the content of this chapter has been published in [18].

2.1.1 Analytical reconstruction method

Analytical methods are based on an idealized mathematical model that discretizes the continuous space. The first mathematical algorithm for reconstructing the images from the projections was developed by the German Physicist J. Radon in 1917. But, it was not applied in the medical field until the invention of the Computed Tomography in 1972. The projections can be rewritten using the Radon transform as:

$$P_\theta = \int_{-\infty}^{\infty}\int_{-\infty}^{\infty} f(x,y)\delta(xcos\theta + ysin\theta - t)dxdy, \tag{2.1}$$

where $f(x,y)$ is a 2D slice of the attenuation map to reconstruct and (x,y) the position of each pixel in the slice. A new rotational coordinates system is defined with t corresponding to each ray and θ to the projection angle.

The solution of the problem is based on the inverse formula of the Radon transform through the central slice theorem, represented in Figure 2.2 for a 2D case. This theorem states that the Fourier transforms of a parallel projection of an image $f(x,y)$ taken at angle θ gives a slice of the 2D transform, $F(u,v)$, subtending an angle θ with the u-axis [20].

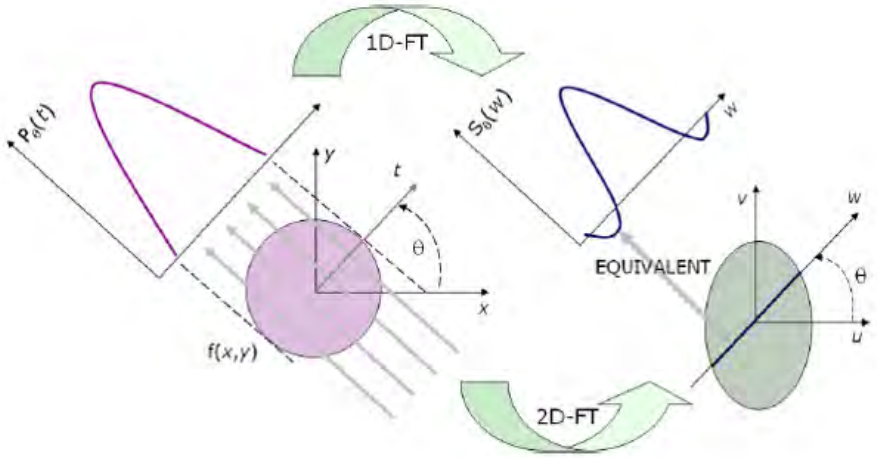

Figure 2.2: Central slice theorem. Source: [21].

Direct Fourier Methods

Once enough number of projections are obtained (i.e. from 0 to 180º in case of parallel-beam geometry), the 2D Fourier transform of the object can be approximated and it can be reconstructed with the inverse 2D Fourier transform:

$$f(x,y) = \int_{-\infty}^{\infty}\int_{-\infty}^{\infty} F(u,v)e^{j2\pi(ux+vy)}dudv, \tag{2.2}$$

where $u = \omega cos\theta$ and $v = \omega sin\theta$.

If the number of projections was infinite, the space corresponding to the 2D Fourier transform of the image would be fully sampled, leading to a perfect reconstruction. Nevertheless, the number of projections is limited, and the samples must be regridded to a Cartesian coordinate system with an interpolation [22]. Unfortunately, this interpolation is inaccurate in the frequencies far away from the center, shown in Figure 2.3, and it results in artifacts in the reconstructed image.

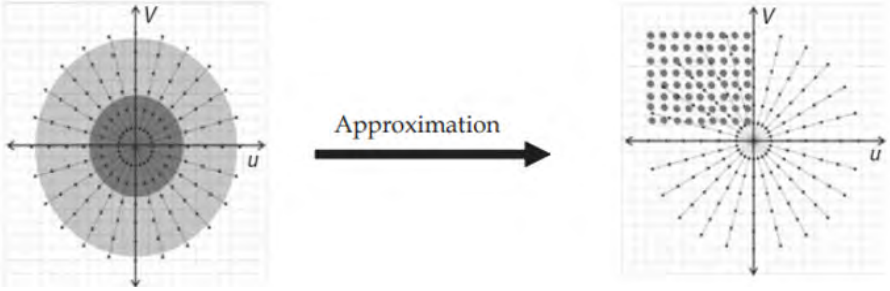

Figure 2.3: Approximation of the 2D Fourier transform from the polar (left) to the square (right) coordinates system. Source: [23].

Filtered Backprojection algorithm (FBP)

This method avoids the interpolation rewriting the inverse Fourier transform, equation 2.2, in polar coordinates:

$$f(x,y) = \int_0^{2\pi} \int_0^{\infty} F(\omega,\theta) e^{j2\pi\omega(xcos\theta+ysin\theta)} d\omega d\theta. \tag{2.3}$$

From the property $P_\theta = P_{\theta+\pi}$ and the relation given by $t = xcos\theta + ysin\theta$, the previous equation can be rewritten as:

$$f(x,y) = \int_0^{\pi} \int_0^{\infty} F(\omega,\theta)|\omega| e^{j2\pi\omega t} d\omega d\theta, \tag{2.4}$$

where, applying the central slice theorem and substituting the 2D Fourier transform of $f(x,y)$ for the 1D Fourier transform of the projection:

$$f(x,y) = \int_0^{\pi} \int_{-\infty}^{\infty} P_\theta(\omega)|\omega| e^{j2\pi\omega t} d\omega d\theta. \tag{2.5}$$

where, $|\omega|$ is the equivalent to a ramp filter. The previous equation can also be shown as:

$$f(x,y) = \int_0^{\pi} Q_\theta(x\cos\theta + y\sin\theta) \tag{2.6}$$

where

$$Q_\theta = \int_{-\infty}^{\infty} P_\theta(\omega)|\omega| e^{j2\pi\omega t} d\omega. \tag{2.7}$$

Since the previous equations consider a continuous space, the implementation of the method in real data started with the discretization of the image into pixels. This discretization also leads to a transformation of the integrals in equation 2.6 into summatories:

$$f(x,y) = \frac{\pi}{K} \sum_{i=1}^{K} Q_{\theta_i}(x \cos\theta_i + y \sin\theta_i) \tag{2.8}$$

where K indicates the number of acquisition angles of the measured data. This summatory is also known as backprojection and it is based on the spreading of the measured data along each ray, i, of the acquisition. In summary, the basic steps to reconstruct an image using FBP are:

1. Collect the line integrals by obtaining the projections.
2. Perform the 1D Fourier transform of each line integral.
3. Multiply each 1D Fourier transform by a ramp function.
4. Perform the 1D inverse Fourier transform of each filtered line integral.
5. Backproject the data.

Nevertheless, there are some issues to take into account for a practical implementation of this algorithm. Since it is impossible to create an ideal ramp filter, this operation may produce a bias in the image that must be corrected [24]. Besides, the discretization of the image hinders a perfect backprojection of the data; thus, many approaches have been proposed in the literature. The most basic is pixel-driven, which assumes that the values of the image matrix are located at the center of each pixel [25]. Although this approximation is easy to implement, it can cause artifacts in the projection [26]. Finally, as mentioned before, the analytical reconstruction methods consider an idealized acquisition process characterized by an infinite number of projections, data without noise, monoenergetic sources, etc. This assumption can lead to artefactual or noisy reconstructed images using acquisitions out of this idealized context, such as low-dose or limited-data acquisitions.

2.1.2 Iterative methods

Iterative reconstruction methods face the reconstruction problem considering the image as an array of unknowns. All of them recover the image values based on three major steps (see Figure 2.4):

1. The projection of the estimated or initial image.
2. The estimation of the correction term, which is based on the comparison of the original acquisition and the projection of the estimated image.

3. The backprojection of the correction image and the addition to the previous estimated image.

These three majors steps are repeated until the algorithm reaches a fixed number of iterations or the correction term is small enough. The initial image to start the iteration process can be an empty image or an analytical reconstruction. Nevertheless, the closer the initial image is to the solution, the faster the method will converge.

Although the iterative methods are conceptually simpler than the analytical methods, the need for several projections and backprojections increases the computational cost and time. Nevertheless, despite these disadvantages, they can be easily adapted to non-standard geometries, introduce the physics of the acquisition, or enable the use of object constraints (e.g., non-negativity, prior information, ...).

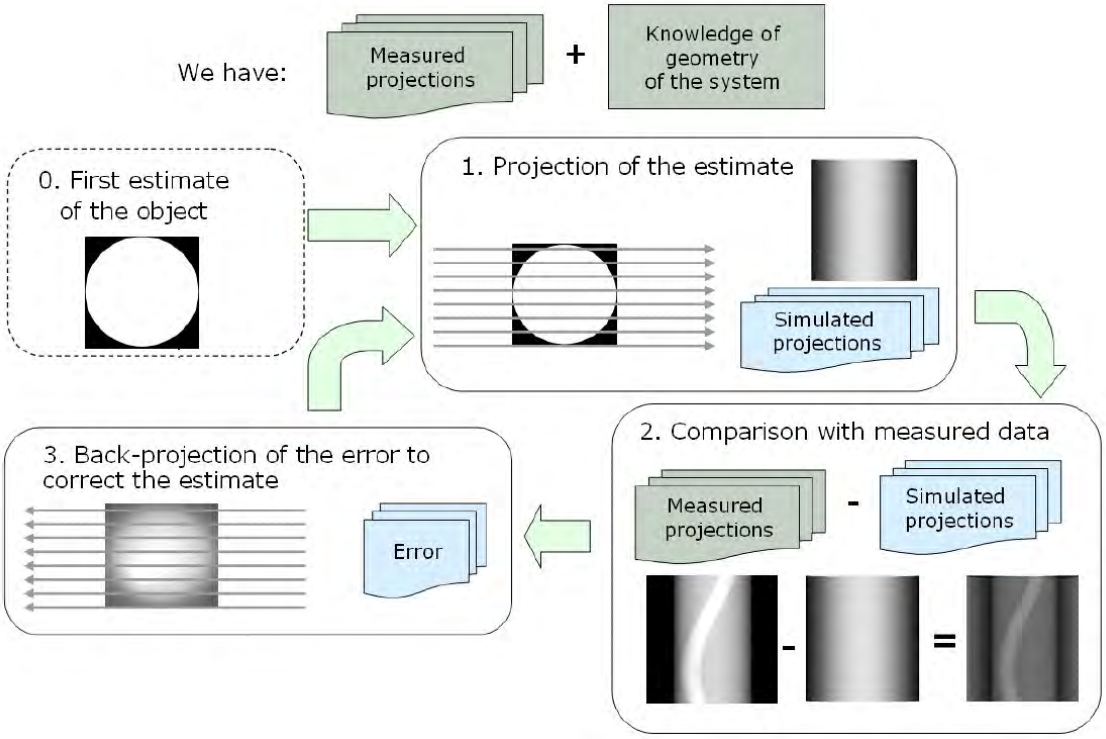

Figure 2.4: General scheme of an iterative method. Source: [21].

Algebraic methods

These methods solve the following linear equation from an algebraic point of view:

$$y = Af, \tag{2.9}$$

where y are the projections, A the contribution of each voxel of the image, the so-called system matrix, and f the image to reconstruct. The previous equation can be rewritten as:

$$\begin{aligned} a_{11}f_1 + a_{12}f_2 + ... + a_{1n}f_n &= y_1 \\ a_{21}f_1 + a_{22}f_2 + ... + a_{2n}f_n &= y_2 \\ &... \\ a_{m1}f_1 + a_{m2}f_2 + ... + a_{mn}f_n &= y_m, \end{aligned} \tag{2.10}$$

where f_n is the value of the n-th voxel in the volume, y_m is the value measured in the detector for the ray m-th and a_{mn} the contribution of the n-th voxel to the pixel y_m due to the ray m-th.

The algebraic methods are based on the work described by Kaczmarz in 1937 that Tanabe further developed [27]. Equation 2.9 derives a grid representation of an image with n degrees of freedom and the desired image can be considered as a single point in an n-dimensional space; considering this space, the single equations of 2.10 represent a hyperplane and, when only exists a unique solution, the intersection of all these hyperplanes is the single point of the desired image (Figure 2.5). Although these methods model the geometry better than analytical methods, they neglect the physics of the acquisition results in noisy images for low-dose acquisitions.

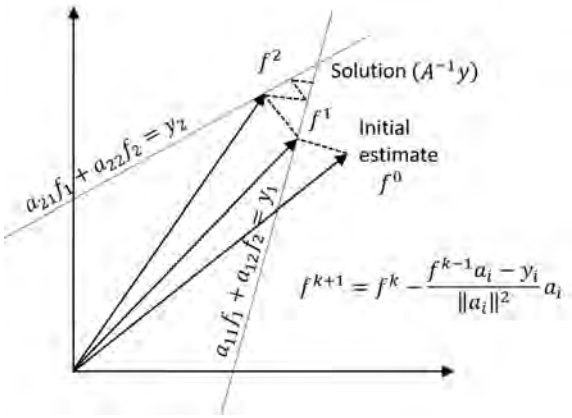

Figure 2.5: The ART method for a two unknowns case [20].

Statistical methods

Statistical methods incorporate the statistics of the acquired photons inside the reconstruction process. They assume the noise model and attempt to find the image values that make the acquisition the most probable. The simplest approach is modeling the logarithmic projections as a Gaussian distribution. However, this assumption is only partially valid in high-dose acquisitions [28]. In low-dose acquisitions, the quantity of photons that reach the detector, the pre-logarithmic image, is usually modeled as an independent Poisson distribution [29], setting the mean of the distribution as the number of photons received by the detector. Nevertheless, previous approximations have to account for the

background events such as scatter or crosstalk [30], being necessary to adapt the Poisson distribution to a shifted Poisson distribution:

$$Y_i \sim Poisson\{I_0 e^{-[A\mu]_i} + r_i\}, \tag{2.11}$$

where r_i denotes the background events previously mentioned, μ the attenuation coefficient and I_0 the number of photons emitted by the X-ray source. Although the above equation is a good approximation for the acquisition noise, it does not count on some extra events as electronic noise. For this reason, more sophisticated methods with a combination of two distributions, such as Poisson and Gaussian, have been proposed [28, 31, 32].

All the previously cited methods take into account the statistics of the noise in the detection process but ignore other processes such as the geometric model or the physical model in the measured object. The methods that include some of these assumptions are usually known as MBIR (model-based iterative reconstruction) [33].

The geometric modeling can improve the spatial resolution by eliminating some assumptions, such as the infinitely small focal spot or detector pixels [33]. Furthermore, since statistical methods need several projections and backprojections, a more accurate geometric modeling than voxel-driven is necessary. In this regard, the use of distance-driven algorithms reduces the artifacts caused by the latter by mapping the boundaries of each pixel of the image and the detector onto a common axis [34].

Regarding the physical model, most reconstruction algorithms assume a monochromatic source where all the source photons have the same energy. Since they ignore the beam-hardening effect, resulting reconstructed images will reduce the noise, but they will present beam-hardening artifacts such as cupping and dark bands. Therefore, various methods have included the relationship between the polychromatic spectrum and the tissues in the algorithm [9, 10, 35].

The previous reconstruction algorithms solve the equations using the maximum likelihood (ML) [10, 35] or least squares (LS) principles [36, 37]. The likelihood measures the chance of producing a specific result by an event that has already happened and the maximization of this function will lead to the image values that makes the acquisition most probable [33]. The algorithms usually use the natural logarithm of the likelihood (log-likelihood) because it maintains the same maximum values and makes the formulations more accessible [38].

The simplest method to solve the maximum-likelihood, is to perform the derivative and set it to zero:

$$\nabla L(\mu) = 0, \tag{2.12}$$

where L is the likelihood of the function. However, this solution is restricted to problems where there are closed-form solutions to the system of equations. Classic optimization

algorithms initialize the image and perform several updates to converge in a certain direction to find the optimum solution:

$$\mu^{k+1} = \mu^k + \alpha^k d^k, \tag{2.13}$$

where α^k is the step size and d^k is the direction to find the optimum solution. This kind of algorithm comprises two steps, (1) the calculus of the step size, α^k, and (2) the direction of the search, d^k. The classification of these algorithms is based on how they determine the step size and the direction of the search. Most known are gradient ascent, steepest ascent and conjugate gradients, which are the point of departure of more complex algorithms [39, 40].

Another approach to gradient-based methods is the use of the optimization transfer principle [10, 35]. This principle states that we can replace a problematic function, $\Phi(\mu)$, with a surrogate function, $\phi(\mu)$ that it is easier to maximize or minimize [38] (Figure 2.6). The surrogate function has to satisfy the following conditions:

$$\phi(\mu^n; \mu^n) = \Phi(\mu^n), \tag{2.14}$$

$$-\nabla_\mu \phi(\mu; \mu^n)|_{\mu=\mu^n} = -\nabla_\mu \Phi(\mu; \mu^n)|_{\mu=\mu^n}, \tag{2.15}$$

$$\phi(\mu; \mu^n) \leq \Phi(\mu), \forall \mu \geq 0. \tag{2.16}$$

One of the most used surrogates is the parabola:

$$\phi(\mu; \mu^n) \triangleq \Phi(\mu) + \Phi'(\mu)(\mu - \mu^n) - \frac{c}{2}(\mu - \mu^n)^2, \tag{2.17}$$

where c is named as curvature. The choice of this curvature has to ensure that the above conditions are satisfied and also affects the speed of convergence. Many examples of curvatures in computed tomography can be found in [41].

Although using these methods produces better images, the need for several projections and backprojections highly increases the reconstruction time. Therefore, it hinders their implementation in clinical and pre-clinical applications. The acceleration of the methods can be performed by the use of ordered subsets, initially introduced in emission tomography [42]. The ordered-subset technique divides the projections into sets and the correction term is obtained for each of these sets instead of the complete range of projections [43].

2.2 Visualization of the CT images

As previously mentioned, the reconstructed 3D volumes represent the attenuation coefficient of the tissues. Nevertheless, the recovered attenuation values depend on the energy

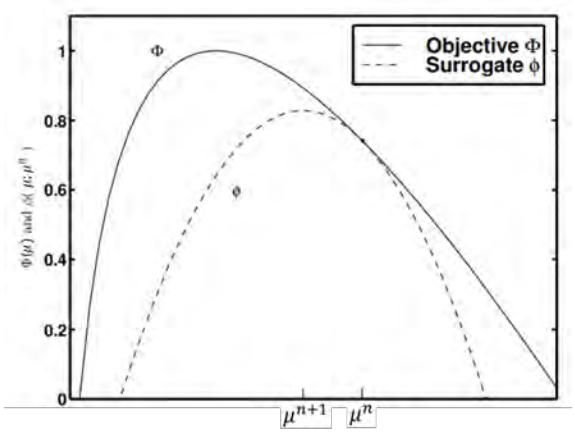

Figure 2.6: Illustration of optimization transfer in 1D. Source: [38].

acquisition, hindering the comparison among CT studies. The standardization of the attenuation eases this comparison and can be performed using the Hounsfield Units (HU) scale. The transformation of the attenuation values to these units follows the equation:

$$HU = 1000 \times \frac{\mu_t - \mu_w}{\mu_w - \mu_{air}} \tag{2.18}$$

where μ_{air}, μ_w and μ_t are the attenuation values of the air, water and tissue to transform, respectively. Nevertheless, the previous equation only standardizes the attenuation values of the air and soft tissue since it does not take into account the attenuation of the bone in the equation 2.18.

2.3 Artifacts in CT image

Artifacts are related to the systematic inconsistencies between the obtained attenuation of the reconstructed image and the true attenuation coefficients of the object [3]. These artifacts usually reduce the visual quality of the image and hinder the recovery of the true attenuation values. According to Barret and Keat [3] the artifacts can be divided into three groups:

- Physics-based artifacts, related to the physical interaction of the photons in the acquisition.
- Patient-based artifacts, which derive from the motion caused by the patient or the presence of metallic implants.
- Scanner-based artifacts, which result from defects in the scanner, such as misalignments between the theoretical and the real geometrical parameters.

2.3.1 Physics-based artifacts

Partial volume. Each voxel of a CT image reproduces the attenuation of the tissues present in the sample. However, due to the limited resolution of the scanners, the resulting value in each pixel is the mean value of all the tissues in that voxel. Therefore, all material edges are blurred at some point depending on the difference in the attenuation (Figure 2.7, left).

Photon starvation. This artifact appeared when the X-ray beam traverses a highly attenuating area and the number of photons that reached the detector is insufficient. It results in projections with high noise levels, which the reconstruction process transform into streaks (Figure 2.7, right). The current of the tube can be increased to avoid these artifacts but the patient will suffer an unnecessary dose when the beam is not traversing the high attenuating areas.

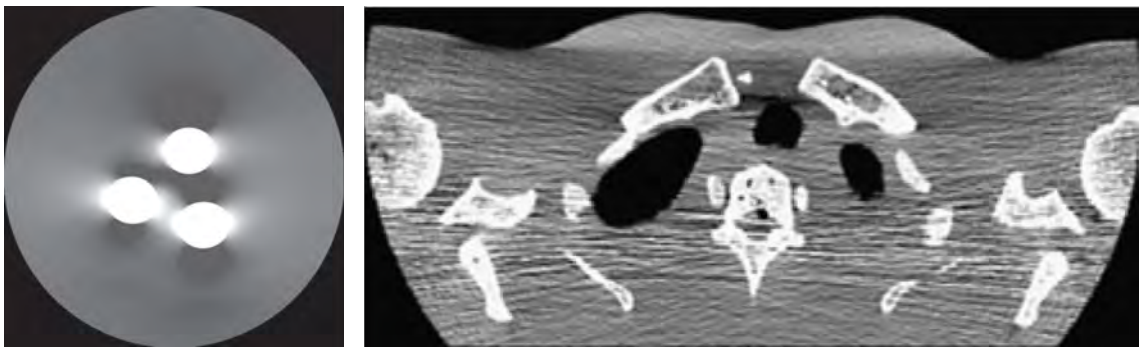

Figure 2.7: Phantom with partial volume artifact surrounding the bone inserts (left) and shoulder acquisition with photon starvation artifacts (right). Source: [3].

Undersampling. The number of projections along a certain span angle is one of the most important factors in image quality. A significantly wide step angle between the projections results in streaks in heterogeneous samples due to the missing information between those spaces (Figure 2.8, left).

2.3.2 Patient-based artifacts

Metallic materials. The presence of metal objects mainly causes two different effects in the acquired projections: strong beam-hardening effect and photon starvation. These two effects lead to severe streaks and incomplete information of the attenuation around the metallic implant (see Figure 2.8, center). They appear due to the high density of the metal, which needs a higher voltage than the ones provided by a medical scanner.

Patient motion. Patient motion produces incoherence of the acquired projections, leading to streaks and blurring artifacts in the reconstructed images as shown in the right panel of Figure 2.8.

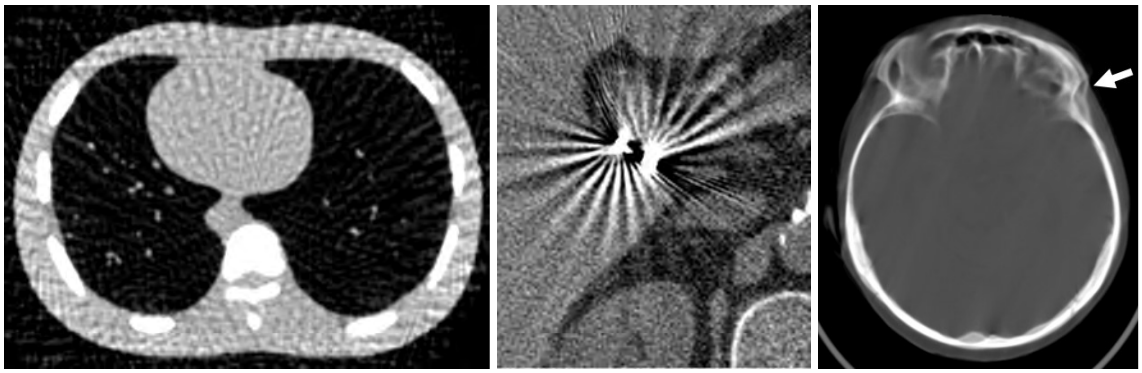

Figure 2.8: Undersampling artifacts in a chest study (left), metallic implant inside the belly (center) and head with motion artifact (right). Source:[3, 44]

.

2.3.3 Scanner-based artifacts

Ring artifacts. The wrong behavior of one pixel of the detector will cause a consistent error at each projection of the acquisition, leading to the appearance of rings in the reconstructed image (Figure 2.9, left).

Cone-beam artifacts. Due to the geometry of the cone-beam scanner, at the end and the bottom of the detector, only part of the object is sampled. This undersampling causes an artifact similar to partial volume with a blurring of the different slices (Figure 2.9, right).

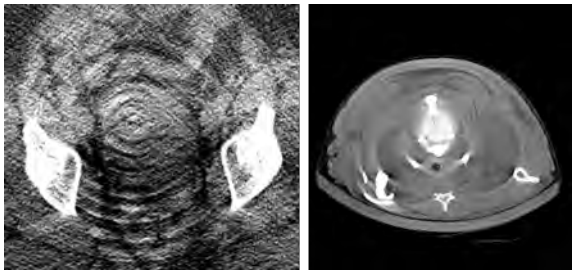

Figure 2.9: Pelvis acquisition with ring artifacts (left) and rat acquisition with cone-beam effect (right). Source: [3, 44].

Geometrical-missalignments artifacts Geometrical parameters can be described as detector misalignments, displacements of the detector in the vertical and horizontal di-

rections (shift), rotation of the flat panel with respect to its central point (skew), and inclinations with respect to its vertical and horizontal axes (roll and tilt, respectively). Any misalignment of the X-ray source can also be translated to a detector misalignment. Variations in the source-detector distance (SDD) can be described as changes in the source-object distance (SOD) or variations in the detector-object distance (DOD), both of which would result in similar effects on the reconstructed image. Effects of these missalignments on the reconstructed images are shown in Figure 2.10. A deep study of the effect of these missalignments and the tolerances to each one can be found in [18].

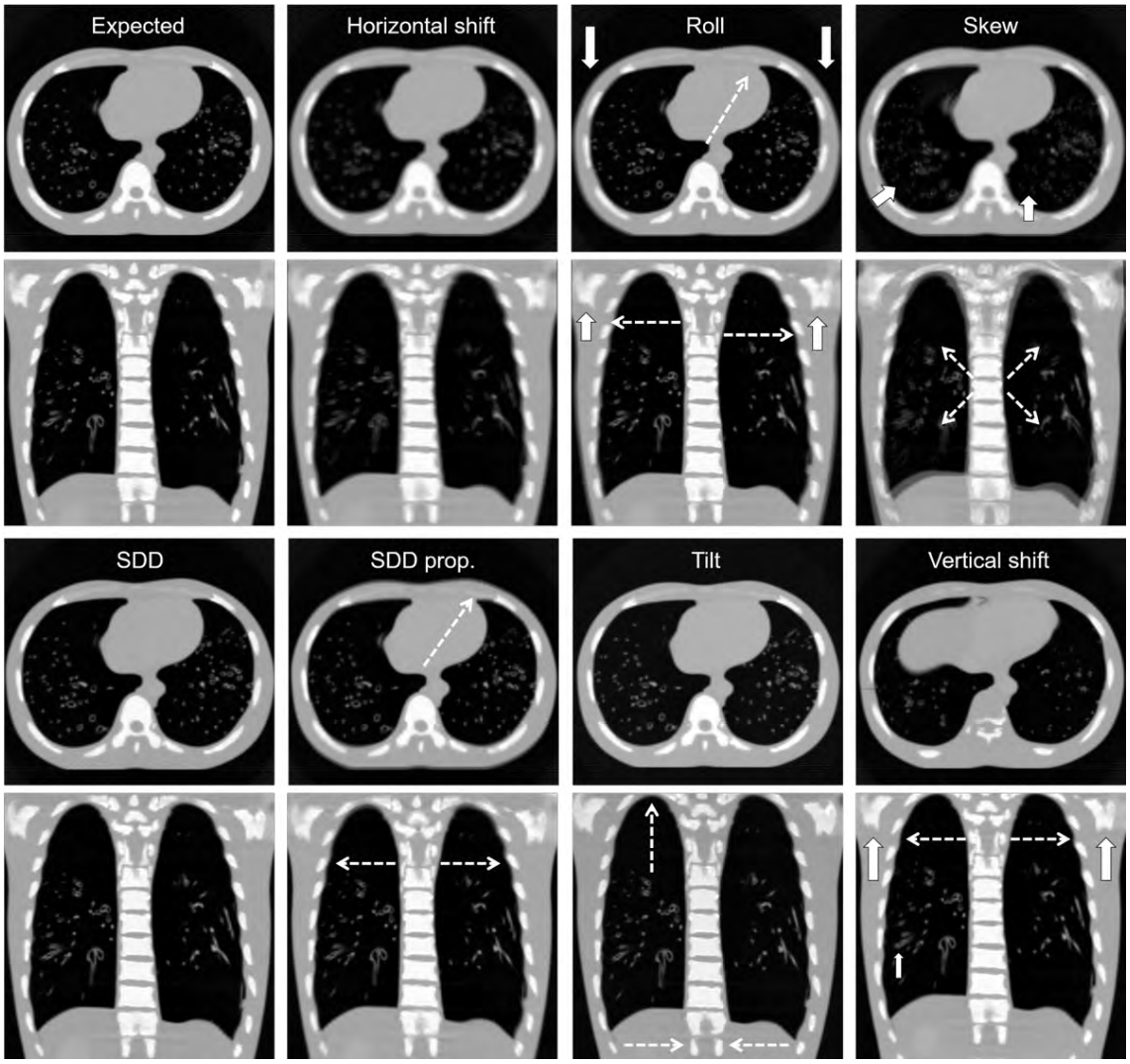

Figure 2.10: Coronal and axial views of an anthropomorphic phantom reconstructed with no errors and with systematic errors of 15 mm in horizontal shift, 5°in roll, 1.5°in skew, 15 mm in SDD, 10 mm in SDD proportional, 15°in tilt, and 15 mm in vertical shift. Source: [18].

2.4 Machine learning and Deep Learning

The advances in computational capacity with the new generations of GPU, together with an improvement of the algorithms, have risen the interest in Artificial Intelligence. AI provides a new way to solve complex problems, based on giving large amounts of data to a computer, so it can learn from them. This learning can be used to solve complex and specific problems such as segmentation, classification or regression [45].

This learning can be divided into three different approaches:

- Supervised learning: The training data comprise pairs of objects, the input data and the labeled data. The objective is the creation of a function able to predict the corresponding output after seeing the training data [46].
- Unsupervised learning: The training data do not include labeled data in contrast to the supervised learning. Instead, it provides the model with raw data. The algorithm processes the data and produces the labels and patterns [47].
- Reinforcement learning: The algorithm learns through the interaction of a dynamic environment [48].

2.4.1 Machine Learning and Neural Networks

Machine learning (ML) is the scientific study of algorithms and statistical models that computer systems use to perform a specific task without being explicitly programmed [49]. This kind of algorithms can be used for solving complex problems thanks to the detection of patterns and features in the data.

Artificial Neural Networks are computational models that consist of a set of units, called artificial neurons (see Figure 2.11), connected among them to transmit information. Basically, the input information traverses the neural network and suffers different operations to produce an output signal. Each neuron is linked to others through connections. The output values of the neuron are obtained by multiplying the input values and adding a bias. This result is introduced in a function, which modifies the output value or imposes a limit. These functions are known as activation functions and the most commonly used are:

- Rectified linear units (ReLU): It is a non-linear function that restricts the output values to 0 when the input is less than 0 and yields to an increasing fixed value when the input is greater than 0.

$$y = f(x) = max(0, x). \tag{2.19}$$

- Sigmoid function: It has an "S" shape and produces an output number between 0 and 1.

$$y = f(x) = \frac{1}{1 + e^{-x}}. \tag{2.20}$$

- Hyperbolic tangent: Similar to the sigmoid function but restricted the output to a number between -1 and 1.

$$y = f(x) = tanh(x) = \frac{2}{1 + e^{-2x}} - 1. \tag{2.21}$$

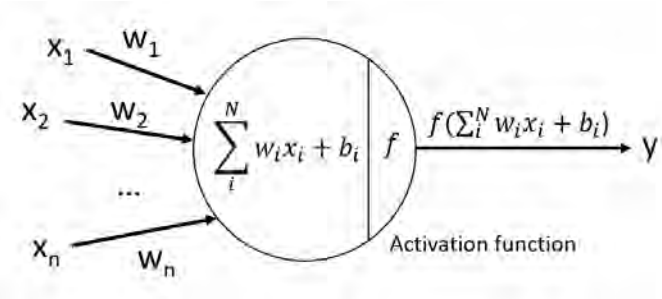

Figure 2.11: Basic scheme of a neuron where x_i are the inputs, b_i the bias, f the activation function and y the output.

A neural network is comprised of several stacks of these neurons, where each stack is known as layer. These stacks can be expressed in terms of composition functions that depend on each layer, i.e. for a two-layer network:

$$y = f(x) = f^2(f^1(x)) \tag{2.22}$$

Independently of the task or the learning approach, the performance of the neural network can be measured by using a cost function. The use of this cost function is similar to the one used in iterative methods, which creates a measurement between the label and the output of the network.

Cost functions

Several cost functions can be selected depending on the approach, the most basics are described here:

- Mean Absolute Error (MAE): The cost function results in the absolute difference between the predicted and the expected value. It is mainly used for regression.

$$MAE = \frac{1}{n} \sum_{i}^{N} |y_{predicted} - y_{expected}| \tag{2.23}$$

- Mean Squared error (MSE): This cost function is one of the most used and common in the literature. It averages the squared difference between the predicted and the expected value. It is also used for regression.

$$MAE = \frac{1}{n}\sum_{i}^{N}(y_{predicted} - y_{expected})^2 \tag{2.24}$$

Optimization algorithm

The objective of the neural network is to find the optimum parameters of each neuron that minimizes this cost function. As mentioned before, the algorithms used to find the minimum are called optimization algorithms. The most used optimization algorithm in Machine Learning is the stochastic gradient descent (SGC) method, which calculates the partial derivatives of each of the parameters of the network. However, this calculus has a high computational cost. A more efficient calculus of the partial derivatives can be done with the backpropagation algorithm. It is based on two stages, the first one propagates an initial information through the neural network and the second one compares this output with the expected one to generate an error. This error is backpropagated to modify the contribution of each neuron to the output information.

2.4.2 Deep Learning and convolutional neural networks

Deep Learning (DL) is a subset which derives from the Machine Learning. The main characteristic of DL is that it does not need any intervention to extract information from the data. From this technique, Convolutional Neural Networks (CNN) arises as a tool for this type of learning and they can be, basically, divided into [50]:

1. Convolutional layers: It convolves the pixels of the image to generate an activation map. These activation maps store all the characteristics features of a given image reducing the computational cost.

2. Pooling layers: These layers reduce the computational complexity by reducing the size of the activation maps.

3. Fully connected layers: All the neurons of these layers are fully connected to the previous and following layers. The main reasoning of the network is performed here.

One of the most simple CNN architecture for a classification task can be generated with an input layer, a convolutional layer and the corresponding activation layer, a pooling layer and a fully-connected layer (see Figure 2.12)

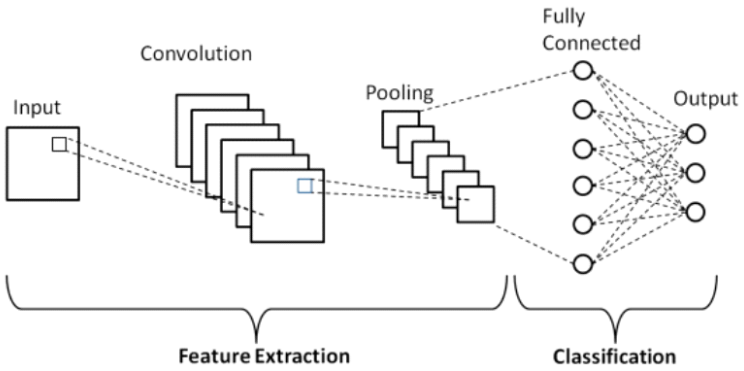

Figure 2.12: Basic CNN architecture for a classification task. Source: [51].

Since the main task of CNNs is the identification of patterns and relations between the input and the expected data of the training data, CNNs are composed of several layers that can reach millions of different parameters corresponding to each neuron [45]. Thus, the training of these networks needs a lot of information.

2.4.3 U-net

U-net, originally proposed by Ronnenberg et al. [52], arises from the need to solve certain problems such as image segmentation, since previously proposed CNNs work properly to classify the whole image but fail to classify each pixel individually. The main structure is composed of an encoder and a decoder, as shown in Figure 2.13. The former is usually composed of convolutional (blue lines) and pooling (red lines) layers that progressively reduce the size of the input image and the latter is composed of deconvolutions (green lines) that gradually recovers the original size of the image. Furthermore, the different levels of the encoder and decoder are related with a concatenation (gray lines), so it preserves some of the original features obtained by the encoder. Although it was originally designed for segmenting microscopic cells, it has demonstrated its potential with other tasks such as the correction of low-sampling artifacts [53] or metallic artifacts [54].

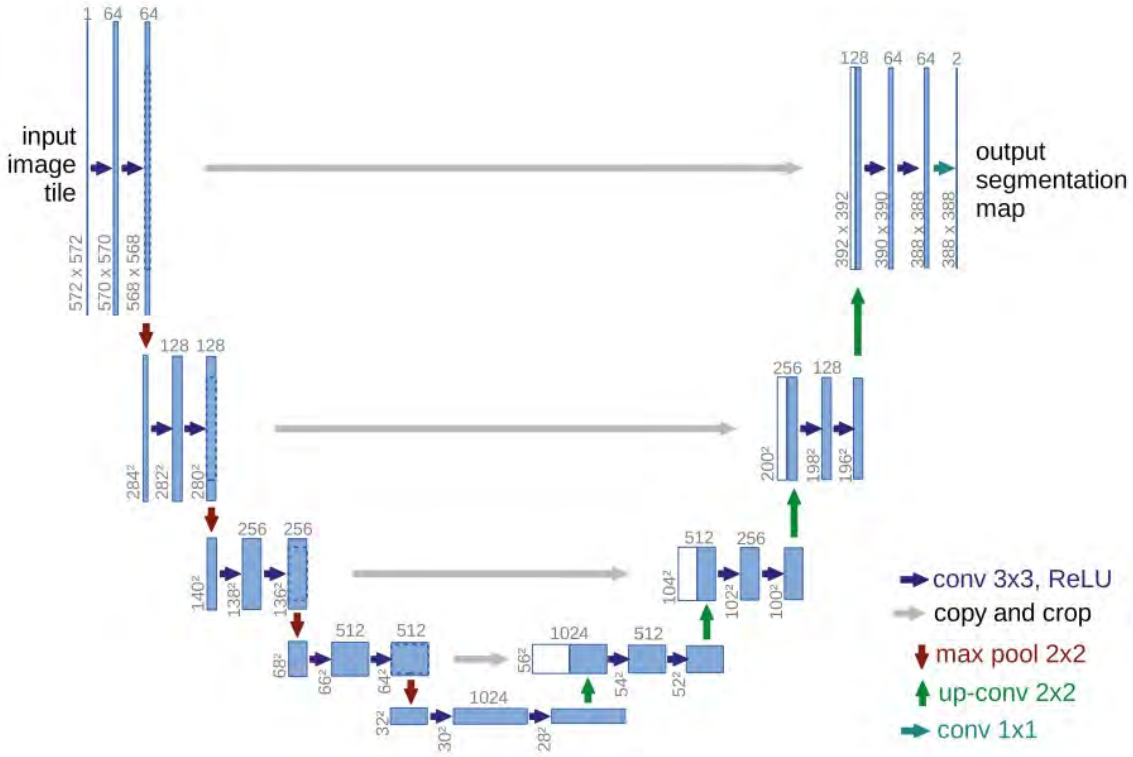

Figure 2.13: Original U-net architecture. Source [52].

Chapter 3

Proposed reconstruction strategies with beam-hardening compensation[2]

This chapter presents the reconstruction strategies proposed in this thesis to obtain CT images without beam-hardening artifacts for the common scenarios found in preclinical research. The chapter is divided in four sections:

1. A brief description of the beam-hardening effect and a review of the methods previously proposed in the literature.
2. Reconstruction strategy for standard-dose scenarios, based on analytical reconstruction followed by a post-processing step.
3. Reconstruction strategy for low-dose scenario, based on iterative reconstruction that incorporates the characterization of the beam-hardening effect in the forward model.
4. Deep-Learning approach valid for standard- and low-dose scenarios.

3.1 Introduction and literature review

As previously mentioned, CT characterizes the attenuation coefficients of the patient tissues through the relation between the number of photons that are emitted by the source and the number of photons that reach the detector. In the case of a monochromatic source and a single tissue, this relation can be modeled with the Beer-Lambert law:

$$I(\varepsilon_0) = I_0(\varepsilon_0)e^{-\rho mac(\varepsilon_0)L}, \tag{3.1}$$

[2]Part of the content of this chapter has been published in [55, 56, 57, 58, 59, 60].

where I and I_0 are the number of photons that are emitted the source and reach the detector, ε_0 the specific energy value of the monochromatic source, ρ the density, *mac* the mass attenuation coefficient and L the thickness traversed of the tissue. The total attenuation suffered by a beam can be cleared from the previous equation, defining the function:

$$F_{MONO}(L) = \ln \frac{I_0}{I} = \mu(\varepsilon_0)L. \tag{3.2}$$

Nevertheless, commercial scanners use polychromatic sources due to the lack of X-ray lasers as a usable alternative and X-ray detectors work in an integrating mode that impedes the discrimination of these photon energies. These circumstances and the fact that attenuation coefficients are roughly decreasing functions in the usual range of energies used in clinical and pre-clinical scenarios (Figure 3.1, left) impose a change in the previous Beer-Lambert law (equation 3.1):

$$I = \int I_0(\varepsilon) e^{\sum_{i=1}^{I} \rho_i mac_i(\varepsilon) L_i} d\varepsilon, \tag{3.3}$$

where ε spans the energy. Considering the energy dependence, we rewrite the equation 3.2 as:

$$F_{BH}(L) = \ln \frac{I_0}{I} = \ln \frac{\int I_0(\varepsilon) d\varepsilon}{\int I_0(\varepsilon_0) e^{-\mu(\varepsilon)L} d\varepsilon}. \tag{3.4}$$

Since the attenuation coefficients are higher for low energies, low-energy photons are preferentially absorbed, thus increasing the effective energy of the spectrum (see Figure 3.1, right). This effect is known as beam hardening.

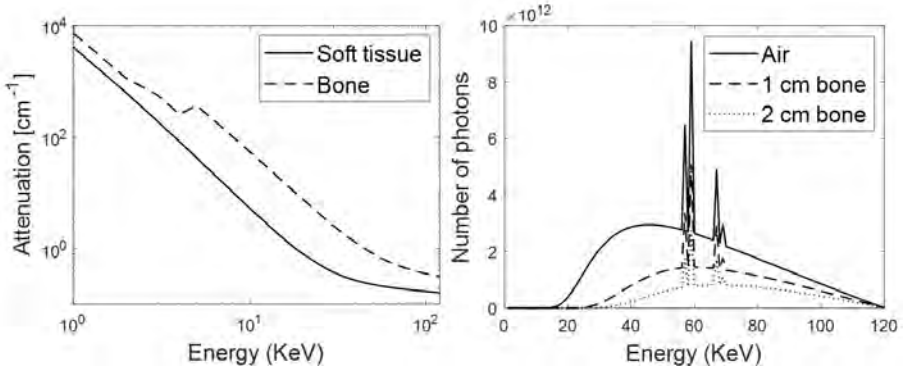

Figure 3.1: Left: Mass attenuation coefficient of the soft tissue and bone. Right: 120 kVp spectrum after traversing air, 1 cm of bone and 2 cm of bone.

The relation between the incident and the detected photons will depends on the length and the type of tissue traversed, leading to lower attenuation values as the beam traverses the object. Figure 3.2 shows the loss of linearity of the F_{BH} compared to the F_{MONO}, which creates inconsistencies in the projection domain and artifacts in the reconstructed images.

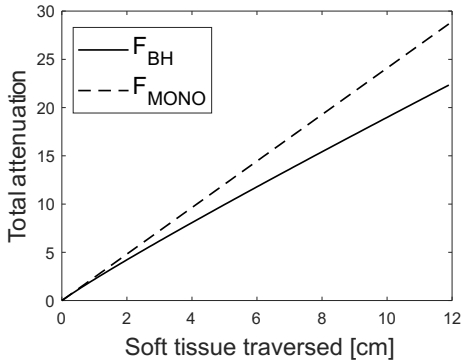

Figure 3.2: F_{MONO} and F_{BH} of soft tissue with a 60 kVp spectrum.

The simplest correction method, implemented in most commercial scanners, is water linearization [4, 61], which assumes that the object in the scan field is composed of only water. This assumption leads to a compensation of the cupping, but produces a suboptimal correction of the dark bands in heterogeneous objects. The water-linearization method is based on a function that replaces the energy-dependent attenuation values, the so-called beam-hardening function (equation 3.4), F_{BH}, with the corresponding monochromatic attenuation values, F_{MONO}. One can obtain F_{BH} both experimentally by a calibration step with a phantom made of soft-tissue equivalent material and analytically with the knowledge of the spectrum and the mass attenuation coefficient of the water. Then, as there is no beam-hardening effect when the amount of tissue traversed is zero [4], F_{MONO} can be calculated as the derivative of F_{BH} at 0.

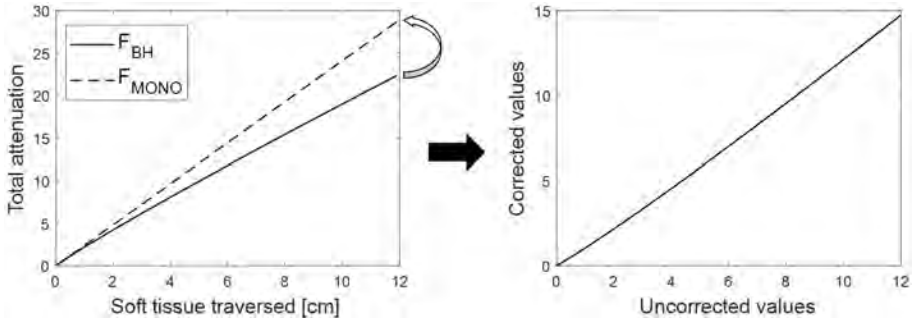

Figure 3.3: Workflow to obtain the 1D linearization function from F_{BH} and F_{MONO}.

Post-processing correction methods have been proposed to correct both cupping and dark bands. These methods estimate the bone and soft-tissue thicknesses traversed through a segmentation in a preliminary reconstruction and calculate a correction factor that depends on these thicknesses. Nalcioglu et al. [5] analytically obtained the equivalent monochromatic attenuation at the effective energy for each thickness of soft tissue and bone from the knowledge of the spectrum and the mass attenuation coefficients of these tissues. In Joseph et al. [6], cupping was corrected with the water-linearization method and afterwards dark bands were compensated including the bone thickness in a second-

order polynomial (Figure 3.4). These coefficients, which can be empirically found by visual inspection, control the compensation of the dark bands and the bone value on the image. However, this approximation is only valid for small areas of bone [6].

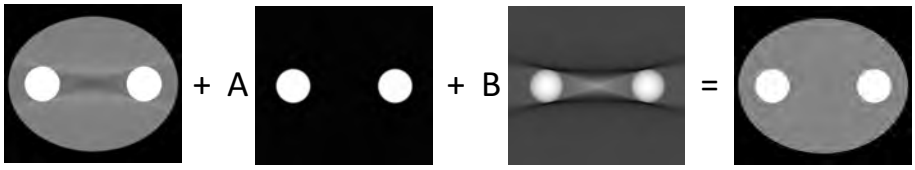

Figure 3.4: Correction scheme of the JS method.

As in the previous method, Kyriakou et al. [7] calculated the bone thickness through a segmentation in a preliminary reconstruction. This bone thickness is linearly combined with the original projections and reconstructed to obtain images with overcorrected dark bands (see Figure 3.5). These images are then combined with the water-corrected image. The coefficients of this combination are automatically calculated minimizing the image flatness. However, it has been shown to not completely correct the dark bands [62].

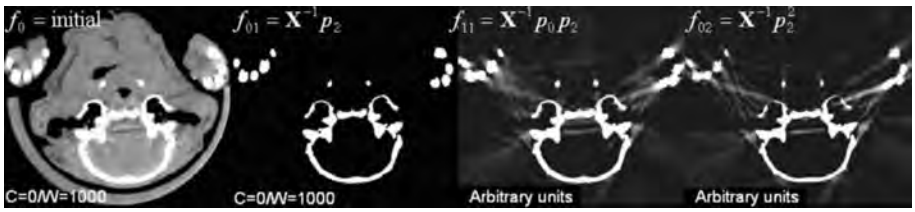

Figure 3.5: Initial image and the corresponding overcorrected images for the example of a rat head. X^{-1} is the reconstruction operator, p_0 the original projections and p_2 the bone thickness. Source: [7].

Following the same idea, Schuller et al. [8] increases the number of overcorrected images in the linear combination (see Figure 3.6) and substitute the segmentation step with a histogram spreading that increases the values above a threshold. Nevertheless, this method was shown to produce an overcorrection of the beam-hardening artifacts in real studies [8] and need for several projections and backprojections, which increases the execution time.

Recently, in the industrial field, two different methods appeared that make use of the redundancy in the projection domain and the epipolar consistency conditions to reduce beam hardening artifacts [63]. However, the resulting images showed a non-realistic texture of the tissues and authors comment that is unclear if the method performs as well as previous methods in medical imaging and also produce artifacts in the corrected images.

Post-processing methods may fail with low-dose studies because of the need of a tissue segmentation. To deal with these low-dose studies, iterative reconstruction methods are presented as a good alternative. Yan et al. [64] proposed a non-statistical method that

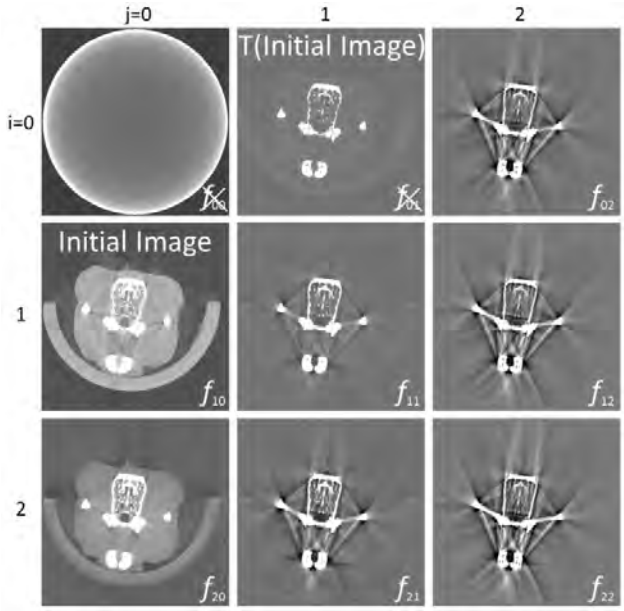

Figure 3.6: All of the overcorrected images obtained from the combinations of the bone thickness and the original projections [8].

iteratively computes the volume fraction of soft tissue and bone with the information of the spectrum and the attenuation coefficients of the tissues. However, it did not take into account the noise associated with the acquisitions. To improve the robustness against the noise, Man et al. [9] proposed a maximum-likelihood iterative algorithm that decomposed the linear attenuation coefficient into photoelectric and Compton scatter components. The weight of each component was constrained based on prior tissue assumptions. Following this line, Elbakri and Fessler [35] developed a statistical method based on Poisson distributions, which assumed the object is composed of known tissues that had to be segmented. The previous method was improved in [10] by allowing pixels to contain mixtures and including the segmentation in the cost function where it is iteratively updated. However, all these iterative reconstruction methods need the knowledge of the spectrum to characterize the beam-hardening effect produced by the soft tissue and bone. The need of the spectrum was substituted by Srivastava and Fessler in [12] with the same calibration data and tuning parameters as Joseph and Spital. However, the proposed model made an approximation that can lead to nonphysical negative values prone to cause convergence problems.

The high execution time of the iterative methods can be drastically reduced with the use of Deep Learning approaches. Zhou et al. [65] used a three-layer convolutional network, trained with reconstructed simulated data, to correct industrial-CT images. However, training and test data were very simple with images composed of only one material. Kalare et al. [16] proposed an end-to-end workflow that reconstructs images free of artifacts from the original projections. Nevertheless, the concatenation of three consecutive U-net networks hinders the reconstruction of high-resolution images and a huge amount

of training data is needed to avoid overfitting.

3.2 Reconstruction strategy for standard-dose scenarios

Since for standard-dose acquisitions image quality is not an issue, post-processing was the strategy selected in this scenario, due to the low computational cost in comparison to iterative methods. Following previous post-processing strategies proposed in the literature, we consider the sample to be composed of only two tissue types: bone (B) and soft tissue (ST). The rationale behind this assumption comes from the dependence of the attenuation properties on energy for different tissues in the body, as most tissues behave like water and only bone differs significantly (see Figure 3.7) [11].

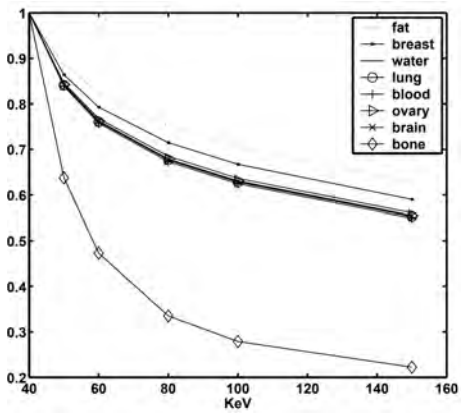

Figure 3.7: Mass attenuation coefficient of tissues normalized at 40 keV [11].

Under this assumption, equations 3.2 and 3.4 can be rewritten as:

$$F_{MONO}(L_B, L_{ST}) = \mu_B(\varepsilon_0)L_B + \mu_{ST}(\varepsilon_0)L_{ST}, \tag{3.5}$$

$$F_{BH}(L_B, L_{ST}) = \ln \frac{\int I_0(\varepsilon)d\varepsilon}{\int I_0(\varepsilon)e^{-\mu_B(\varepsilon_0)L_B - \mu_{ST}(\varepsilon)L_{ST}}d\varepsilon}. \tag{3.6}$$

The characterization of these two functions could be done analytically with the knowledge of the spectrum and the mass attenuation coefficients of the soft tissue and bone. However, as mentioned above, spectrum knowledge is not always available. To avoid the need of this knowledge, two different methods were explored. The first one uses a calibration phantom composed of equivalent materials to soft tissue and bone, and the second one is based on the information provided by the sample, extracted from a segmentation of the soft tissue and bone in a preliminary reconstruction. The following sections describe both methods in detail.

3.2.1 Calibration-based approach (2DCalBH)

The characterization of $F_{BH}(L_B, L_{ST})$ and $F_{MONO}(L_B, L_{ST})$ is experimentally done with a calibration phantom composed of equivalent materials to soft tissue and bone.

Figure 3.8 shows the calibration workflow. Each material is segmented in a preliminary reconstruction and then projected to obtain the bone and soft-tissue thicknesses, (L_B, L_{ST}), for each projection value, $F_{BH}(L_B, L_{ST})$. Typically, $F_{BH}(L_B, L_{ST})$ can be fitted with a polynomial function [66], however, these functions could lead to non-monotonically increasing values. To avoid it, $F_{BH}(L_B, L_{ST})$ is fitted to a logarithmic function:

$$F_{BH}(L_B, L_{ST}) = -\ln a * e^{-(b*L_{ST}+c*L_B)} + (1-a) * e^{-(d*L_{ST}+e*L_B)}, \tag{3.7}$$

where , a, b, c, d and e are the fitting coefficients, obtained with a non-linear least squares method, with random numbers between 0 and 1 as initial values of the coefficients.

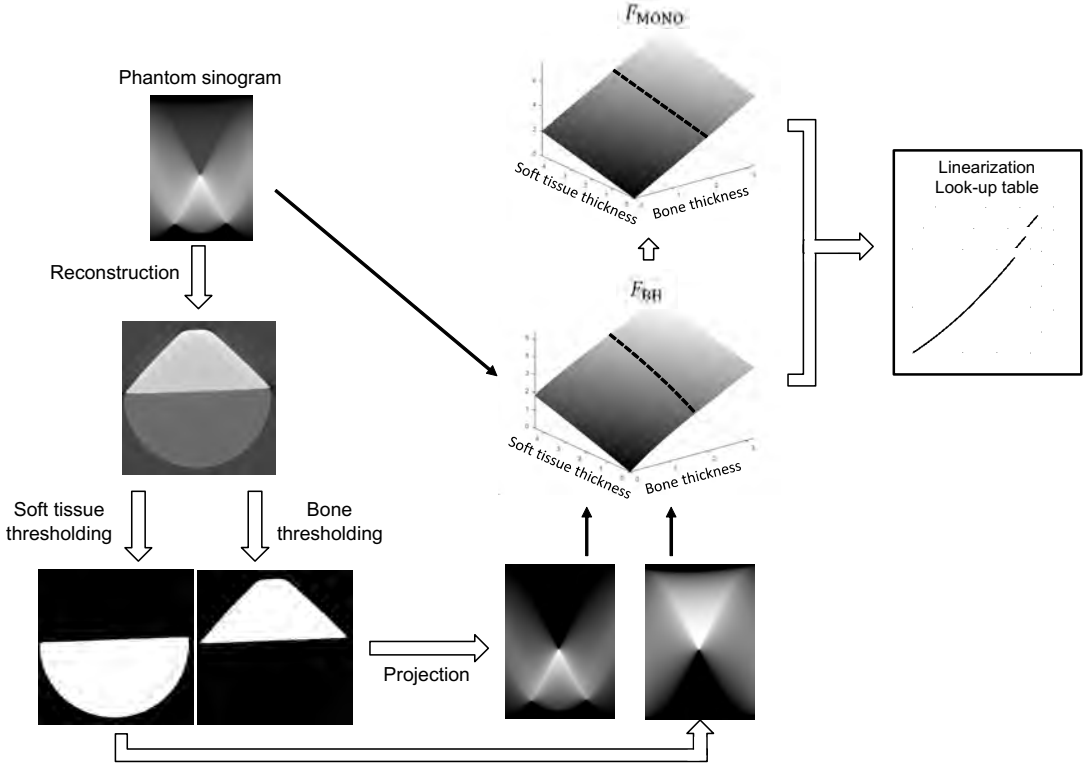

Figure 3.8: Workflow of the calibration to generate the correction parameters (example for one slice).

As there is no beam-hardening effect when the tissue traversed is zero [4], slope values $\mu_{ST}(\varepsilon_0)$ and $\mu_B(\varepsilon_0)$ in equation 3.5 are estimated as the partial derivatives of the beam-hardening function at the (0,0) point (i.e., $\frac{\partial F_{BH}(0,0)}{\partial L_{ST}}$ and $\frac{\partial F_{BH}(0,0)}{\partial L_{ST}}$). Algorithm 1 shows the pseudocode of the calibration process.

Ideally, the correction would be obtained with a linearization function that replaces the energy-dependent attenuation values, $F_{BH}(L_B, L_{ST})$, with the corresponding monochro-

Algorithm 1 Calibration step of 2DCalBH

```
phantom=fbp(projPhantom)
boneMask=segmentBone(phantom)
STMask=segmentST(phantom)
[ST_Trav,B_Trav]= project(STMask,boneMask)
bh_Function=fit(ST_Trav,B_Trav,projPhantom)
mono_Function=createPlane(deriv(bh_Function(0,0)))
for b = 1 to max(B_Trav)
LUT(b)=fit(bh_Function(:,b), mono_Function (:,b))
end
```

matic attenuation values, $F_{MONO}(L_B, L_{ST})$. However, this relation is not injective, i.e., there are multiple combinations of (L_B, L_{ST}) that result in the same $F_{BH}(L_B, L_{ST})$ value. To solve this non-uniqueness, we use the bone thickness, $\hat{L_B}$, as a constraint and generate multiple linearization functions obtained from the pairs $F_{BH}(\hat{L_B}, L_{ST}))$ - $F_{MONO}(\hat{L_B}, L_{ST}))$ (see dashed lines in Figure 3.8). These functions are fitted by second-order polynomial regressions, using linear least squares, and stored in a 1D look-up table (LUT) for each $\hat{L_B}$ value. A bone-thickness spacing in the LUT (sampling of $\hat{L_B}$) below the voxel size would prevent streak artifacts from a wrong selection of the correction function.

Figure 3.9 shows the workflow of the proposed calibration-based approach. The bone is segmented from a preliminary reconstruction and projected to obtain the bone thickness corresponding to each pixel in the projection. This bone thickness, interpolated by the nearest neighbor, is used to select the appropriate linearization function from the LUT, which will be applied to that pixel. Algorithm 2 shows the pseudocode of the correction step.

Algorithm 2 Correction step of 2DCalBH

```
fbpu=fbp(proj)
boneSeg=segmentBone(fbpu)
b_Trav=project(boneSeg)
for pix= 1 to NPixels
bonePix=b_Trav(pix)
fLinearization=LUT(bonePix)
projCorrected(pix)=fLinearization(proj(pix))
end
```

Tissue equivalent materials

The soft-tissue equivalent materials reported in the literature comprise polymethyl methacrylate [67, 68, 69], water [70], and plastic A-150 [68]. Nevertheless, water may lead to

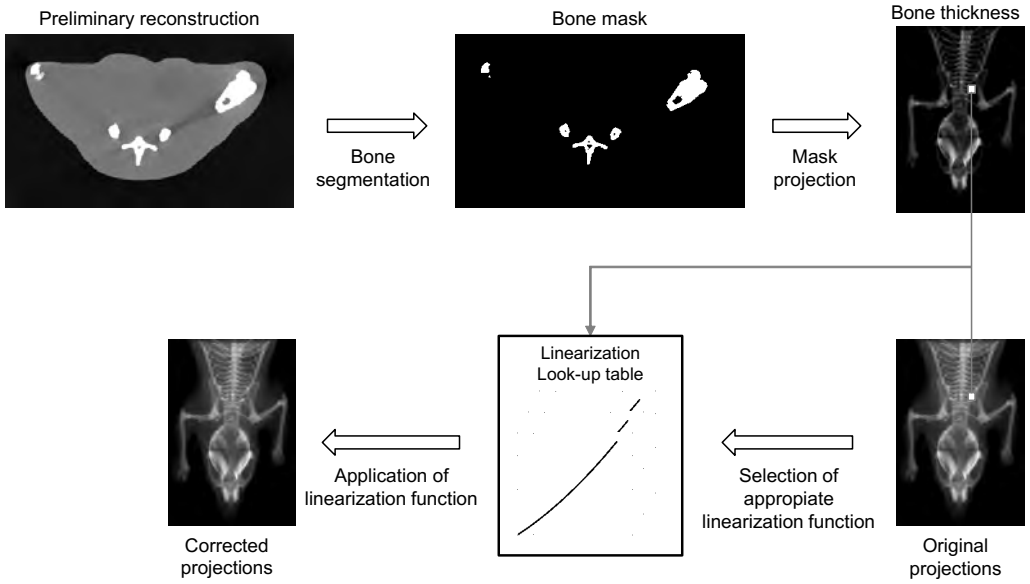

Figure 3.9: Workflow of the correction step.

evaporation or bubbkle formation and plastic A-150 is expensive and difficult to obtain [60]. In contrast, PMMA is an unexpensive and easily accesible material with a beam-hardening function similar to soft tissue (see Figure 3.10, right).

Regarding bone, the most common equivalent materials are aluminum [67, 69, 70, 71] and Teflon [72]. However, mass attenuation coefficient of Teflon is significantly different form that of bone [60] and manufacturing a pure aluminum phantom is not possible owing to its low machinability. To solve the drawback of aluminum machinability, different available alloys from the aluminum association with good machinability were evaluated. Alloy AL6082 was found to be very similar to pure aluminum (Z = 13), containing only very few iron impurities. Nevertheless, the beam-hardening function of AL6082 does not match with that corresponding to bone, due to the difference in density between cortical bone (1.92 g/cm3) and AL6082 (2.7 g/cm3). This deviation can be compensated by multiplying the bone thickness by a weighting factor equal to the ratio of densities, 2.7/1.92 (dotted line in Figure 3.10, right).

Taking into account the previous considerations, a realistic calibration phantom can be made up of PMMA and aluminum 6082 (AL6082) as an equivalent material of soft-tissue and bone respectively. For a small-animal scanner, we propose a phantom made up of a half-cylinder of soft-tissue equivalent material (radius of 3 cm) plus one triangular prism with rounded corners of bone equivalent material (height of 2.5 cm and width of 6 cm), as shown in Figure 3.11.

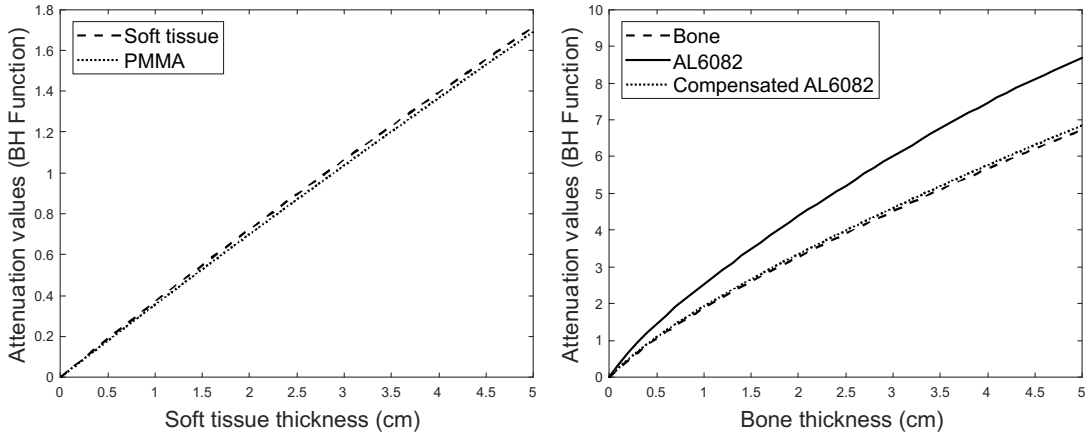

Figure 3.10: Beam-hardening function of soft tissue and PMMA (left), and beam-hardening function of bone and AL6082 before and after compensation (right).Beam-hardening functions were simulated with a 50 kVp spectrum.

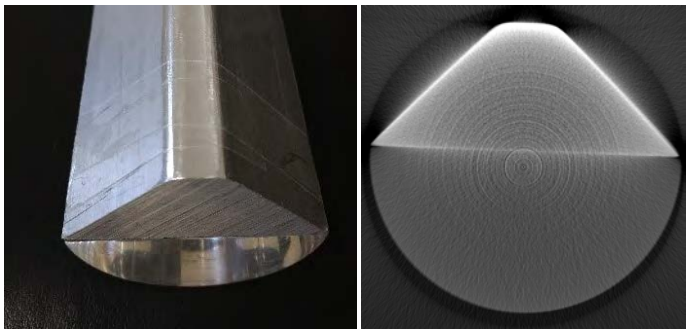

Figure 3.11: Photograph (left) and axial view of a CT reconstruction (right) of the proposed calibration phantom made up of PMMA and AL6082.

3.2.2 Sample-based method (FreeCalBH)

A possible drawback of the previous method is that it may restrict the sample to have similar attenuation properties to the equivalent materials in the calibration phantom. FreeCalBH avoids the use of equivalent materials, by characterizing $F_{BH}(L_B, L_{ST})$ and $F_{MONO}(L_B, L_{ST})$ empirically with the information provided by the sample.

Figure 3.12 shows the workflow of the FreeCalBH method. A preliminary reconstruction is performed (Figure 3.12, step 1) to separate the soft tissue and bone by simple thresholding. These masks are projected to obtain the tissue thicknesses in each pixel of the original projection (Figure 3.12, step 2). An uncomplete beam-hardening function is obtained using the soft tissue and bone thicknesses, as x and y-axis, respectively, and the acquired projection data, as the z-axis (Figure 3.12, step 3). $F_{BH}(L_B, L_{ST})$ is then fitted with the same equation used for 2DCalBH (equation 3.7) to extrapolate the missing combinations of soft tissue and bone (Figure 3.12, step 4). Similar to 2DCalBH, the calculus of the monochromatic attenuation coefficient is performed with the derivative of

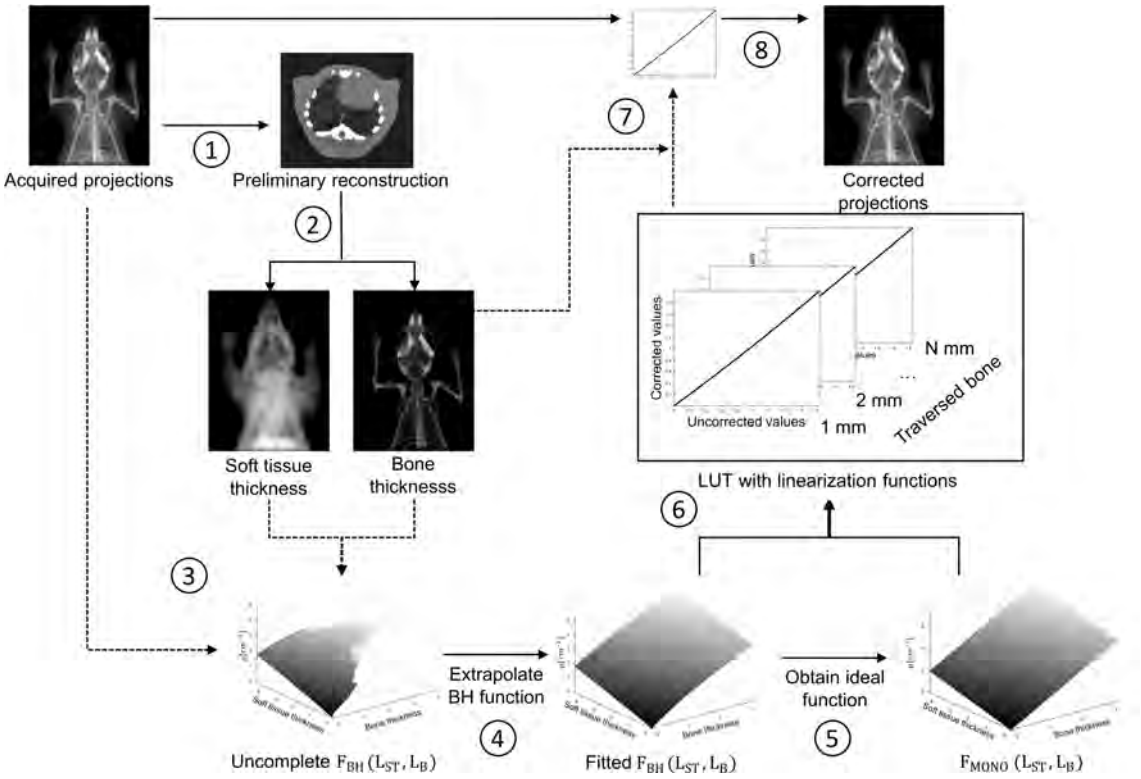

Figure 3.12: Workflow of the sampled-based approach.

$F_{BH}(L_B, L_{ST})$ at 0 (Figure 3.12, step 5).

As in 2DCalBH, one linearization function was created for each bone thickness (Figure 3.12, step 6) and stored in a look-up table that provides the 1D-linearization function corresponding to one particular bone thickness. For each pixel in the projection, the bone thickness, previously calculated, is used to select the appropriate 1D-linearization function (Figure 3.12, step 7) and applied it to the projection values (Figure 3.12, step 8).

The complete process of FreeCalBH involves one preliminary reconstruction to perform the bone and soft tissue segmentation and two projections to calculate the thickness of each tissue. The pseudo-code is shown in Algorithm 3.

3.3 Reconstruction strategy for low-dose scenarios

Since the post-processing strategies may fail with low-dose acquisitions, specially because of difficulties in the segmentation, the iterative strategies are a good alternative due to the possibility of incorporating a model of the noise and a regularization term to deal with streak artifacts. The proposed iterative strategy use the usual polyenergetic model

Algorithm 3 FreeCalBH

```
fbpSample=fbp(projSample)
boneMask=segmentBone(phantom)
STMask=segmentST(phantom)
[ST_Trav,B_Trav]= project(STMask,boneMask)
bh_Function=fit(ST_Trav,B_Trav, projSample)
monoFunction=createPlane(deriv(bh_Function(0,0)))
for b = 1 to max(B_Trav)
LUT(b)=fit(bh_Function(:,b),monoFunction(:,b))
end
for pix= 1 to NPixels
bonePix=B_Trav(pix)
fLinearization=LUT(bonePix)
projCorrected(pix)=fLinearization(projSample (pix))
end
```

[35] for the mean of the i-th measured sinogram data value:

$$\overline{Y}_i = \int I_i(\varepsilon) e^{-\int_{L_i} \mu(x,y,z,\varepsilon)} d\varepsilon + r_i, \tag{3.8}$$

where $\mu(x, y, z, \varepsilon)$ denotes the unknown energy-dependent attenuation coefficient map of the object. The integral in the exponent is taken over the path of the i-th ray, L_i, and the "spectrum" $I_i(\varepsilon)$ incorporates the energy dependence of both the incident ray, a bowtie filter, and the detector sensitivity. The term r_i can account for scatter and other background signals and is assumed known here. The goal is to reconstruct μ from the noisy measurements Y_i having mean given in equation 3.8.

3.3.1 Object model: Segmentation free implementation

For an object composed of K different substances, we express the attenuation coefficient at pixel j using the following model:

$$\mu_j(\varepsilon) = \sum_{k=1}^{K} m_k(\varepsilon) \rho_j f_k^j \tag{3.9}$$

where ρ_j denotes the unknown density, $m_k(\varepsilon)$ denotes the known mass attenuation coefficient of the k-th substance, and f_k^j denotes a unitless tissue fraction that quantifies the contribution of material k to attenuation in voxel j. As in the previous post-processing strategy, we assume that the object consists of only two substances: bone and soft tissue.

To prevent an increase of the number of unknowns and avoid preliminary segmentation, we define a model for the tissue-fraction value in the pixel, f_k^j, as a function of

the estimated density in that pixel, similarly to what was proposed in [11]. For the two-material case we assume

$$\begin{aligned}\mu_j(\varepsilon) \approx \sum_{k=1}^{2} m_k(\varepsilon)\rho_j f_k^j\left(\rho_j\right) = \\ \left(m_{\mathrm{s}}(\varepsilon) f_{\mathrm{s}}^j(\rho_j) + m_{\mathrm{b}}(\varepsilon) f_{\mathrm{b}}^j(\rho_j)\right)\rho_j,\end{aligned} \tag{3.10}$$

with tissue fraction functions, $f_{\mathrm{s}}^j(\rho_j)$ and $f_{\mathrm{b}}^j(\rho_j)$, shown in Fig 3.13, and given by:

$$f_s = \begin{cases} 1 & \rho \leq 1.1 \\ -54.29 + 133.6\rho - 105.5\rho^2 + 27.1\rho^3 & 1.1 \leq \rho \leq 1.5 \\ 0 & 1.5 \leq \rho \end{cases} \tag{3.11}$$

$$f_b = \begin{cases} 0 & 0 \leq \rho \leq 1.1 \\ 55.3 + 133.6\rho + 105.5\rho^2 - 27.1\rho^3 & 1.1 \leq \rho \leq 1.5 \\ 1 & 1.5 \leq \rho \end{cases} \tag{3.12}$$

where ρ has units g/cm^3 . Taking into account the values provided by NIST, we assume soft tissue density is below 1.1 g/cm^3 and set a threshold for bone density of 1.5 g/cm^3. The coefficients were obtained as the result of a third-order polynomial fitting using a linear least-squares regression.

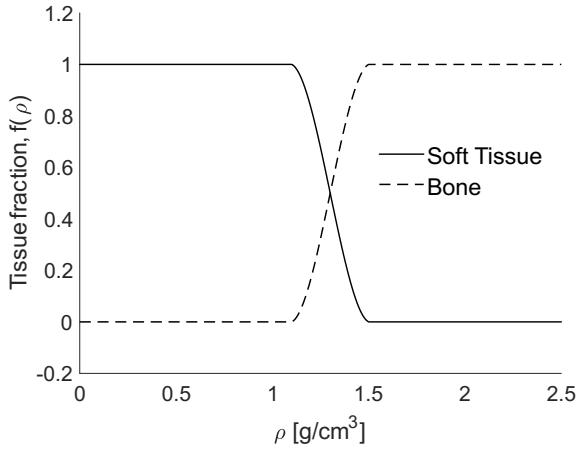

Figure 3.13: Third-order polynomial tissue-fraction functions for soft tissue, $f_{\mathrm{s}}(\rho)$, and bone, $f_{\mathrm{b}}(\rho)$.

This object model is included into the cost function and iteratively updated, leading to a better separation of the tissues along the iterations, as shown in Figure 3.14.

3.3.2 Algorithm

An accurate model of the physics of CT acquisition needs to account for the energy-integrating detection process and the additive detector read-out noise. On the other hand,

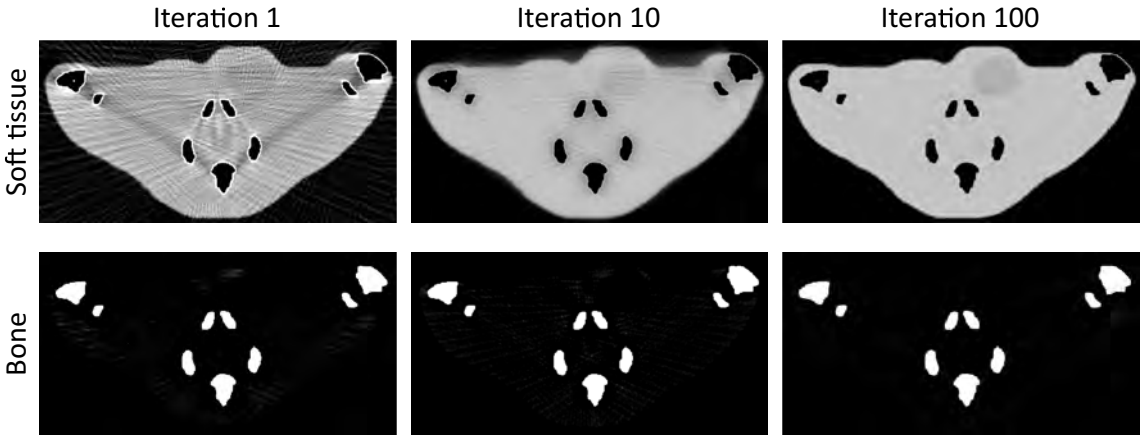

Figure 3.14: . Soft-tissue and bone segmentations for a low-dose and low-sampling case of a rodent simulation at different iterations.

sophisticated models often lead to more difficulties in optimizing the associated penalized-likelihood. For simplicity, in this work we approximate the measurement statistics as independently distributed Poisson random variables [43]:

$$Y_i \sim \text{Poisson}\left\{\overline{Y}_i\right\}, \quad i = 1, ..., N \tag{3.13}$$

The corresponding negative log-likelihood for independent Poisson measurements is given by:

$$-L(\rho) = \sum_{i=1}^{N} h_i \left(F_{\text{BH}}(t_{\text{ST}}(\rho), t_{\text{B}}(\rho))\right) \tag{3.14}$$

with:

$$h_i(l) = -Y_i \log\left(I_i e^{-l} + r_i\right) + I_i e^{-l} + r_i, \tag{3.15}$$

where r_i accounts for mean contamination by extra background counts caused primarily by scatter. Because data is noisy and tomography is an ill-posed problem, we use regularization by adding a penalty term to the likelihood function that controls how much the object ρ departs from prior assumptions about image properties. In this work a 3D roughness penalty function with the convex edge-preserving Huber potential was used:

$$\begin{aligned} R(\rho) &= \sum_{j=1}^{N_p} \frac{1}{2} \sum_{k \in N_j} w_{jk} \cdot \psi\left(\rho_j - \rho_k\right); \\ \psi(t) &= \begin{cases} \frac{|t|^2}{\delta} & |t| \leq \delta \\ \delta |t| - \frac{\delta}{2} & |t| > \delta \end{cases}, \end{aligned} \tag{3.16}$$

where N_j is a neighborhood of pixels near pixel j, w_{jk}=w_{kj} and ψ is the convex edge-preserving Huber potential. This penalty function is modified as described in [73] to improve spatial resolution uniformity. The penalized cost function is now:

$$\Phi(\rho) = -L(\rho) + \beta R(\rho), \tag{3.17}$$

where the scalar parameter β controls the tradeoff between the data-fit and penalty terms.

An iterative algorithm was derived based on separable quadratic surrogates using the principles of optimization transfer [43], resulting in the following update:

$$\rho^{n+1} = \rho^n - D^{-1}\nabla\Phi\left(\rho^n\right), \tag{3.18}$$

where D is a diagonal matrix that influences the rate of convergence. Instead of designing D to ensure that the algorithm monotonically decreases the cost function we choose the elements of D approximately as suggested in [35, 43] by using the following pre-computed curvature:

$$d_j = \left(Km_{\mathrm{s}}\left(\varepsilon_{\mathrm{eff}}\right)\right)^2 \sum_{i=1}^{N} a_{ij}\left(\sum_j a_{ij}\right) Y_i, \tag{3.19}$$

where we include K as a tuning parameter for the step size.

3.3.3 Forward model: Beam hardening function

With the model explained above, we express 3.8, i.e., the mean of the measured data along the path of the i-th ray, L_i, as:

$$\overline{Y}_i(\rho) = \int I_i(\varepsilon) e^{-m_{\mathrm{s}}(\varepsilon)t_{\mathrm{s}}^i(\rho) - m_{\mathrm{b}}(\varepsilon)t_{\mathrm{b}}^i(\rho)} d\varepsilon + r_i \tag{3.20}$$

where $t_{\mathrm{s}}^i(\rho)$ and $t_{\mathrm{b}}^i(\rho)$ denote the contributions of each tissue type to the line integral along the i-th ray having units g/cm^2 and given by:

$$t_{\mathrm{s}}^i(\rho) = \sum_{j=1}^{p} a_{ij} f_{\mathrm{s}}^j\left(\rho_j\right)\rho_j, \quad t_{\mathrm{b}}^i(\rho) = \sum_{j=1}^{p} a_{ij} f_{\mathrm{b}}^j\left(\rho_j\right)\rho_j, \tag{3.21}$$

where a_{ij} denotes elements of the system matrix (having units cm). Grouping the energy dependent terms into the exponent yields

$$\overline{Y}_i\left(\rho\right) = I_i e^{-F_{BH}\left(t_{\mathrm{s}}^i(\rho), t_{\mathrm{b}}^i(\rho)\right)} + r_i; \quad I_i \equiv \int I_i\left(\varepsilon\right) d\varepsilon. \tag{3.22}$$

Here, the beam-hardening function, F_{BH}, is characterized with the mass thickness as the x- and y-axis. This change is necessary since the objective of the iterative method is the estimation of the density. Following this line, the function can be defined as:

$$F_{BH}\left(t_{\mathrm{s}}, t_{\mathrm{b}}\right) = -\log\left(\int \frac{I\left(\varepsilon\right)}{I} \exp\ \left(-m_{\mathrm{s}}(\varepsilon)t_{\mathrm{s}} - m_{\mathrm{b}}(\varepsilon)t_{\mathrm{b}}\right) d\varepsilon\right), \tag{3.23}$$

where we drop the dependence on ray i for simplicity. One could calculate the F_{BH} analytically if the X-ray spectrum were known, however, it is often not the case, as previously mentioned. The following three sections describes the proposed methods to estimate this model.

Analytical method (1DIterBH)

The idea of 1DIterBH is inspired by the post-reconstruction correction method proposed by Joseph and Spital [6], which uses the concept of 'effective density', that is, the amount of water that would produce the same beam-hardening effect as the given amount of bone traversed. The 1D version of F_{BH}, equation 3.4, corresponding to water, which has attenuation properties similar to soft tissue, is usually available for most scanners (Figure 3.15). This method approximates the complete 2D beam-hardening function by using the 1D function corresponding to water plus two additional parameters that we tune empirically. This concept is introduced in the forward model of an iterative algorithm by rewriting the beam hardening function as

$$F_{BH}\left(t_{\mathrm{s}}, t_{\mathrm{b}}\right) = F_{BH}\left(t_{\mathrm{s}} + \sigma\left(t_{\mathrm{s}}, t_{\mathrm{b}}\right), 0\right) = F_{w}(t_{\mathrm{e}}), \tag{3.24}$$

where $F_{w}(t) = F_{BH}(t, 0)$ is the beam hardening function corresponding to water and t_{e} is the line integral of the effective density, i.e. water equivalent.

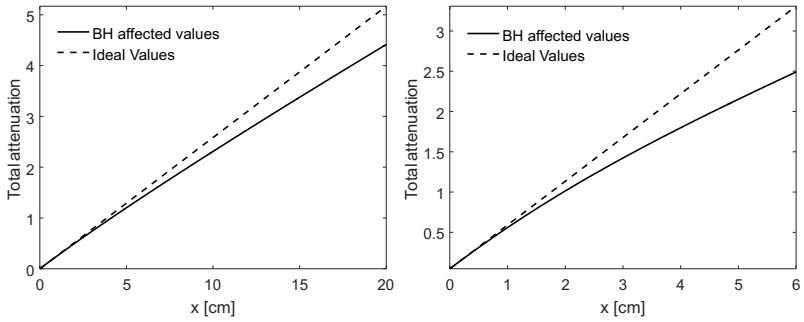

Figure 3.15: Beam-hardening (BH) function used for the so-called water correction (linearization). Left: Simulation corresponding to water for a 100 kVp spectrum. Right: Calibration of the real scanner ARGUS/CT using a PMMA phantom for a 40 kVp spectrum.

The full X-ray spectrum would be needed to determine $\sigma\left(t_{\mathrm{s}}, t_{\mathrm{b}}\right)$ exactly, just like for the function $F_{BH}\left(t_{\mathrm{s}}, t_{\mathrm{b}}\right)$. Figure 3.16 shows calculated plots of $\sigma\left(t_{\mathrm{s}}, t_{\mathrm{b}}\right)$ for a typical polyenergetic spectrum.

As we can see in the left panel of Figure 3.16, the dependence on t_{s} can be considered negligible when the amount of bone in the object is small, which is the case in clinical studies. Joseph and Spital suggested a power series approximation of the function that defines the measured projection depending only on t_{b} [6]. Hsieh [74] described a similar approach, based on

$$\sigma_{1}\ \left(t_{\mathrm{b}}\right) = A t_{\mathrm{b}} - B t_{\mathrm{b}}^{2}, \tag{3.25}$$

where A and B are parameters that one can tune. Although approximation of equation 3.25 works adequately for FDK reconstruction, it can fail when used in the forward model of a statistical reconstruction method because it can yield negative values.

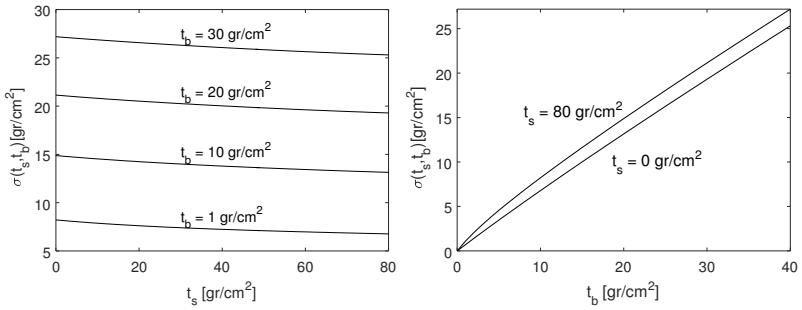

Figure 3.16: Simulation of $\sigma(t_s, t_b)$. Left: profiles versus t_s where each line corresponds to different values of t_b. Right: profiles versus t_b corresponding to the minimum and maximum t_s values.

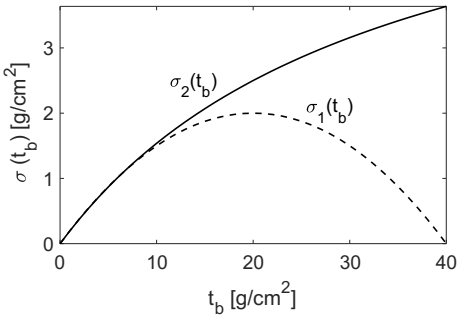

Figure 3.17: Two examples of approximations for $\sigma(t_s, t_b)$.

Furthermore, one can verify that $\sigma(t_s, t_b)$ is a monotone increasing function of both of its arguments, whereas 3.25 is not (see Figure 3.17). To overcome this drawback of equation 3.25, we investigated the following alternative approximation:

$$\sigma_2(t_b) = \frac{A t_b}{1 + \frac{B}{A} t_b}, \tag{3.26}$$

where, as in 3.25, A is unitless and B has units cm^2/g. This function is monotone non-negative and matches equation 3.24 for small values of t_b. Substituting 3.26 into equation 3.24 and 3.22 leads to our proposed forward model:

$$\overline{Y}_i(\rho) = I_i e^{-F_w\left(t_s^i(\rho) + \frac{A t_b^i(\rho)}{1+\frac{B}{A} t_b^i(\rho)}\right)} + r_i = I_i e^{-F_w\left(\sum_{j=1}^{p} a_{ij} f_s^j(\rho_j)\rho_j + \frac{A \sum_{j=1}^{p} a_{ij}\left(f_b^j(\rho_j)\right)\rho_j}{1+\frac{B}{A}\sum_{j=1}^{p} a_{ij}\left(f_b^j(\rho_j)\right)\rho_j}\right)} + r_i. \tag{3.27}$$

Calibration-based method (CalIterBH)

To generalize the previous model, only valid when small quantities of bone are traversed, CalIterBH empirically characterizes the model with a phantom composed of equivalent soft tissue and bone materials, similar to 2DCalBH, proposed in the subsection 3.2.1.

However, the independent variable used in 2DCalBH, i.e. the traversed thickness of each tissue, cannot be used in an iterative algorithm which objective is the estimation of the density. For this reason, we use instead the mass thickness of soft-tissue and bone as x- and y-axis, respectively, in the beam-hardening function. This approximation cannot be used in an iterative algorithms, which objective is the estimation of the density. For this reason, we use instead the mass thickness as x- and y-axis in the beam-hardening function. The transformation to the mass thicknesses, t_s and t_b, is done by adding an additional step to the calibration: we multiply each mask by the density of the material (Figure 3.18) extracted from the National Institute of Standard Technologies (NIST).

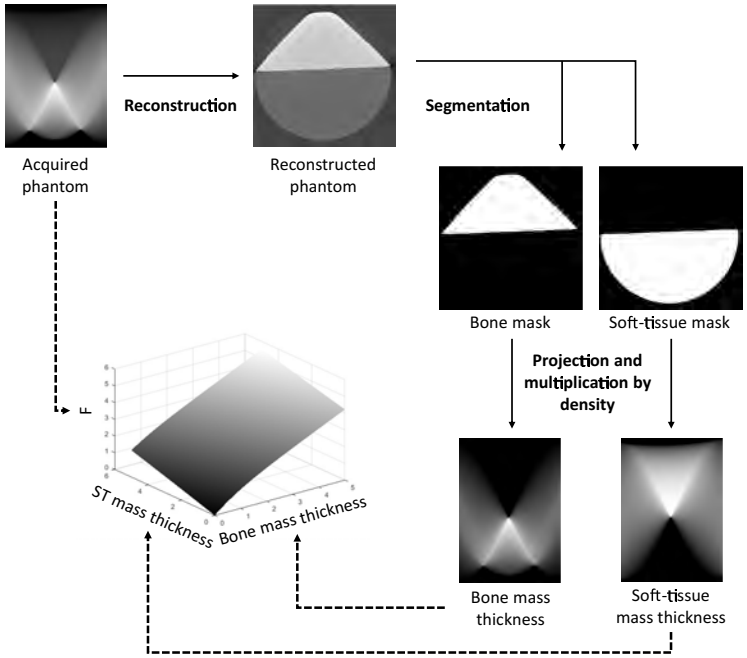

Figure 3.18: Workflow of the beam-hardening function characterization for the 2DIterBH.

Sample-based method (FreeIterBH)

To eliminate the constraint of the equivalent materials, with the idea of fine-tuning $F_{BH}(t_s, t_b)$ to the specific attenuation values of the sample, FreeIterBH determines the function experimentally using the acquired data as in FreeCalBH, explained in subsection 3.2.2. The process to characterize $F_{BH}(t_s, t_b)$ (Figure 3.19) is similar to the process found in FreeCalBH. The differences are the elimination of the generation of F_{MONO} and the correction parameters and the addition of a step to multiply each tissue by the corresponding density previously found in NIST. The generated $F_{BH}(t_s, t_b)$ will not cover the whole space, since a specific acquisition will not have all possible combinations of soft tissue and bone. To completely characterize the beam- hardening function, we extrapolate the incomplete function FBH using the equation 3.7.

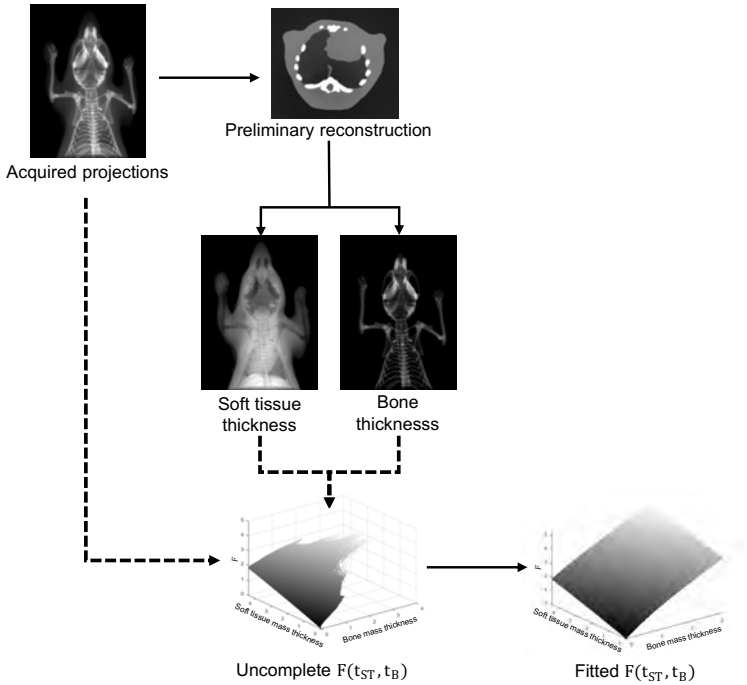

Figure 3.19: Workflow of the beam-hardening function characterization for the 2DStatBH-Sample.

3.4 Proposed Deep-Learning approach for standard- and low-dose scenarios (DeepBH)

Although the iterative strategy results in a good correction of the beam-hardening artifacts as well as the low-sampling artifacts, the execution time is very high. The use of Deep-Learning attempts to reduce the computational time while maintaining the good performance of the iterative strategies. The proposed method, DeepBH, uses a U-net architecture [52] since it allows to maintain the matrix size of the input and output image. Instead of using classical U-net network, we decided to use U-net++, which re-designed the classic U-net architecture connecting the encoder and decoder sub-networks. The rationale behind choosing this network is that it has been shown to produce better results than the classic U-net in medical imaging applications, where more fine details are needed [75].

VGG has been used for the encoder of U-net++ due to the performance of this CNN in a wide variety of tasks [76]. We tested VGG-13 and VGG-16 since the memory requirements for newest one, VGG-19, are too high for the current general-purpose GPUs, like RTX 3060 with 8 GB. Since VGG-16 and VGG-13 showed similar performance, VGG-13 was selected due to its lower number of convolutional layers and thus lower computational cost. The optimization is performed with the Adam optimizer, which provides both faster convergence and more stability than previous methods [77]. The learning rate chosen was

0.0001 after testing a range between and 0.00001. The mean-squared error (MSE) was used as the cost function [78] during 100 epochs.

We have used eight rodent studies, five head and three abdomen studies, acquired with the micro-CT scanner ARGUS/CT of SEDECAL under a standard-dose scenario (360 projections in an angular span of 360 degrees). Low-dose acquisitions were generated by removing one every two projections from these studies. Input images were obtained with FDK reconstruction for both standard- and low-dose scenarios while target images were generated from the reconstruction of the standard dose acquisition using CalIterBH. We have eliminated the slices affected by the cone-beam artifacts from all the reconstructions, resulting in volumes of 512×512×375 voxels and 0.121×0.121×0.121 mm3 of voxel size. Four experiments were carried out depending on the dose scenario and the anatomical part under study. This yielded four datasets:

- Head & standardDose: Five head studies under the standard-dose scenario. Divided into:
  - Training set: A total of 1500 images from four of the studies.
  - Validation set: A total of 375 images from the fifth sudy.
- Head & low-dose: Five head studies under the low-dose scenario. Divided into:
  - Training set: A total of 1500 images from four of the studies.
  - Validation set: A total of 375 images form the fifth study.
- Abdomen & standard-dose: Three abdomen studies of standard-dose scenario. Divided into:
  - Training set: A total of 750 images from two of the studies.
  - Validation set: A total of 375 images from the third study.
- Head & low-dose: Three abdomen studies of low-dose scenario. Divided into:
  - Training set: A total of 750 images from two of the studies.
  - Validation set: A total of 375 images from the third study.

Chapter 4

Evaluation methodology

Simulations used the 3D mouse atlas (digimouse [79]) with soft tissue (1.06 g/cm3), fat (0.95 g/cm3), muscle (1.05 g/cm3) and bone (1.92 g/cm3). Acquisition was based on the CT subsystem of ARGUS PET/CT (SEDECAL) [17], a cone-beam micro-CT scanner based on a flat-panel detector with 0.2 mm of pixel size. The geometry of the system is 226 mm of DSO and 144.95 mm of DOD with a magnification factor of 1.64. The detector was modeled as a simple photon-counting device and the projection data covered a span of 360 degrees with a projection size of 512×200 pixels. Two different scenarios were simulated changing the number of projections and the blank scan value (detector measurement with no sample): A standard-dose scenario, with 360 projections and a blank scan value of 10^6 counts per detector element and a low-dose scenario with 180 projections and 10^5 counts per detector element.

Figure 4.1 shows the workflow to generate the polychromatic projections. It starts with the segmentation of the soft tissues and bone to generate the masks of each tissue. These masks tissues are projected with the FuxSim toolbox [26], generating the mass thickness of each volume (t_{ST} and t_B). Finally, the polychromatic projection is generated incorporating the mass thickness of each tissue in the Beer-Lambert law, equation 3.3, together with the spectrum, $I_0(\varepsilon)$, and the mass attenuation coefficients of each tissue.

We used a 50 kVp polyenergetic spectrum with 0.25 cm aluminum filtration, obtained with the Spektr tool [80], which generate the desired spectrum based on real measurements. The monochromatic source had an energy of 33.1 keV (effective energy of the previous 50 kVp polyenergetic spectra). The mass attenuation coefficients of the tissues were obtained from the NIST.

Figure 4.2 shows two axial slices of the simulated data reconstructed with an FDK-based algorithm [81] and obtaining volumes with 512×512×200 voxels and 0.121 mm of isotropic voxel size.

Evaluation on real data was based on two rodent studies, abdomen and head, and a

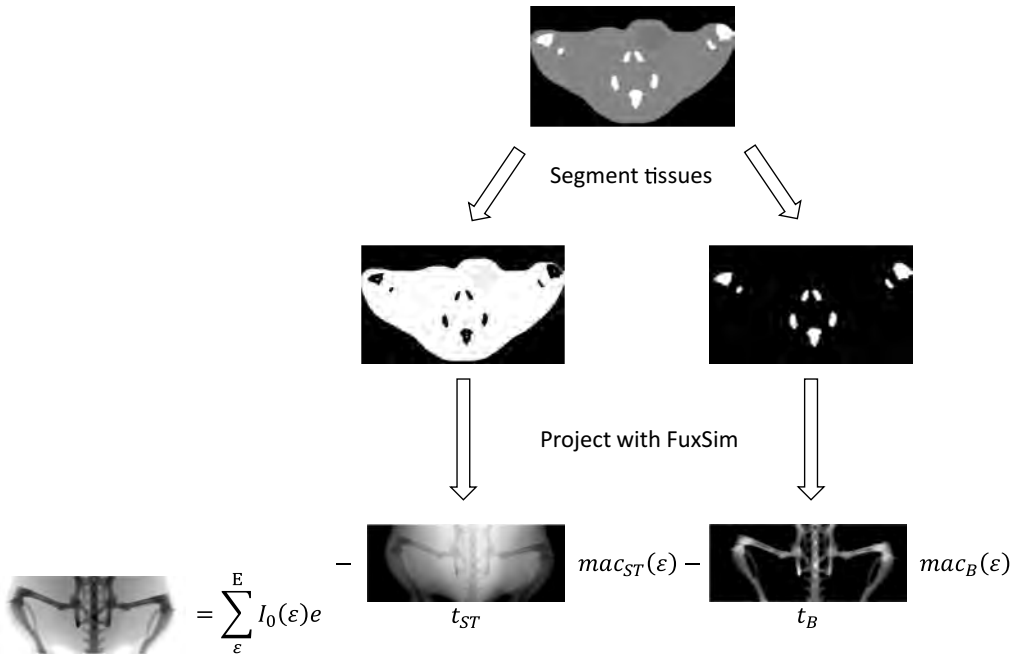

Figure 4.1: Workflow to simulate projections.

mouse study with an intraperitoneal administration of contrast agent composed of iopamidol, iopamiro®. These studies were acquired with the CT subsystem of ARGUS PET/CT (SEDECAL) [17] previously described. Studies were carried out with a current of 200 μA and 50 kVp of source voltage. Projection data, with a size of 514×574 pixels, were acquired in a span angle of 360 degrees pixels and reconstructed with the FDK-based algorithm to obtain a volume of 514×514×574 voxels with a voxel size of 0.121 mm^3. Figure 4.3 shows two reconstructed axial slices of the standard (left) and low (right) dose acquisitions.

Figure 4.4 shows two reconstructed axial slices of the mouse study with the standard-dose scenario, the left one with no contrast agent and the right one with contrast agent in the bladder.

The proposed reconstruction strategies are compared with the water-linearization (WL), the method proposed by Joseph et al. [6] (JS method), sfEBHC proposed by Schuller et al. [8] and a penalized weighted least square (PWLS) method [43]. Evaluation in simulation was done in terms of visual inspection and root-mean-square error (RMSE) with respect to the monochromatic reconstruction. Evaluation in real data was assessed only by visual inspection since there is no ground truth available.

The calibration needed for characterize the beam-hardening effect of the water [4] was generated following two different approaches: (1) an acquisition of an ideal phantom composed of soft tissue only, used for simulations; and (2) the acquisition of a realistic phantom composed of PMMA both for simulations and real data (Figure 4.5). The linearization function obtained was fitted to a second-order polynomial [4].

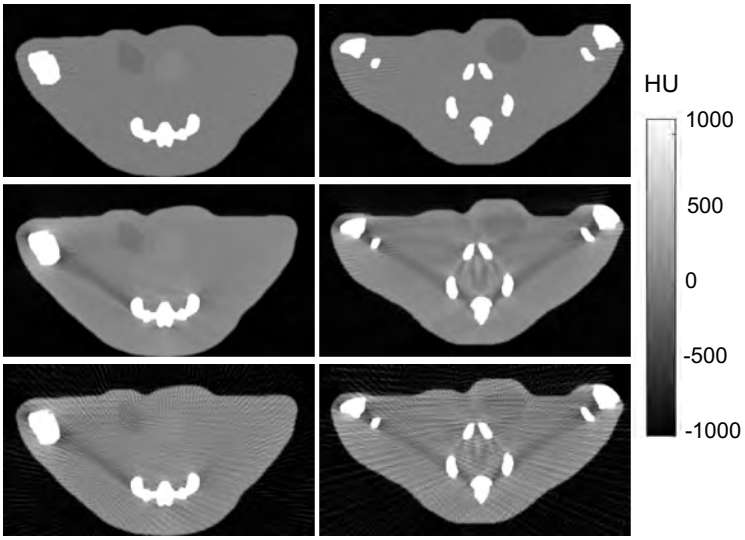

Figure 4.2: Monochromatic (top), standard-dose (middle) and low-dose (bottom) reconstructions of the digimouse.

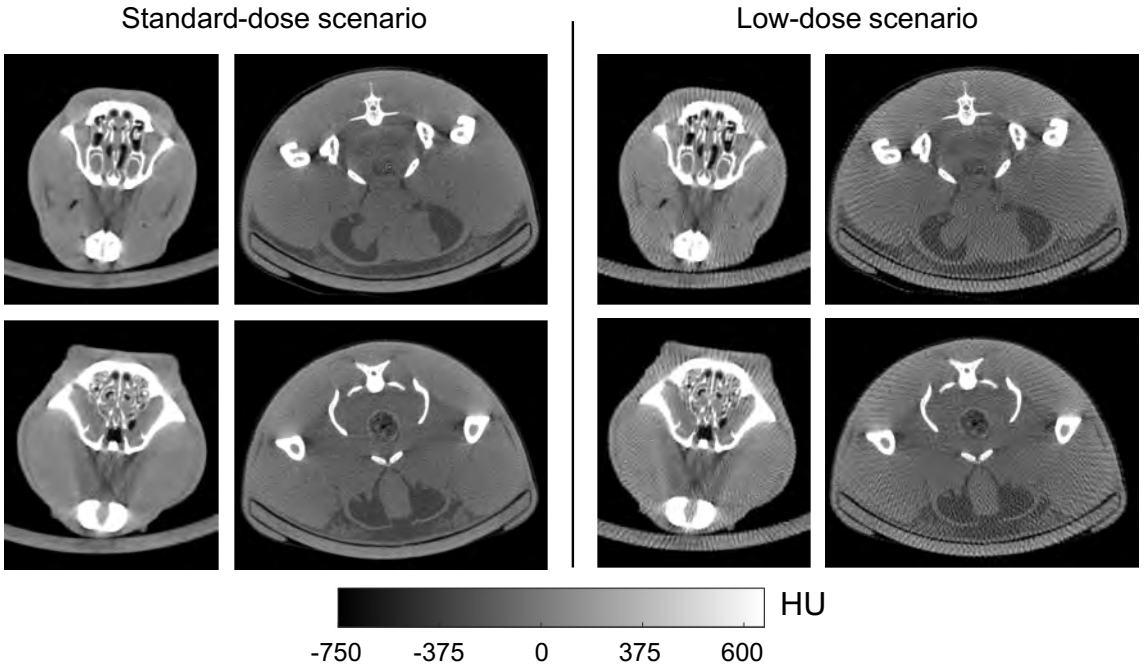

Figure 4.3: Standard and low-dose scenario of the head (left) and abdomen (right) showing the calibration (top) and another slice with a different bone distribution (bottom).

The JS method was implemented according to the following polynomial:

$$p_{JS} = p_W + AL_B + BL_B^2, \tag{4.1}$$

where p_{JS} is the JS-corrected data, p_W is the water-corrected data, and L_B the bone thickness obtained from a preliminary reconstruction, A the parameter to recover the monochromatic bone values and B the parameter that controls the dark-band correction. Parameters were selected heuristically as those that visually reduced the dark bands. Since it was

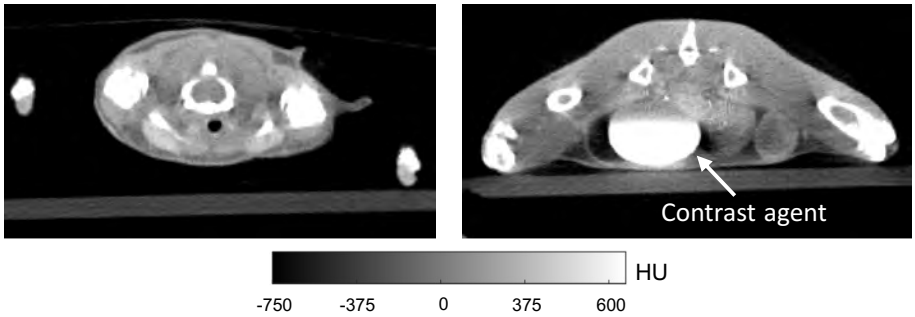

Figure 4.4: Axial slices used to optimize the JS and 1DStatBH parameters (left), with no presence of iodine, and a second slice of the same study (right) with the bladder full of iodine.

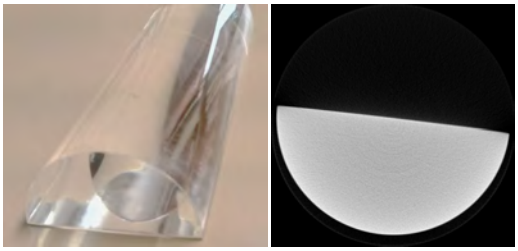

Figure 4.5: Photograph (left) and axial view of the CT reconstruction (right) of the calibration phantom used for the water linearization, made of PMMA.

not possible to find a set of parameters that result in an optimum correction for the whole volume, we took into account the slice with the most conspicuous dark bands, from here on "calibration slice" (Figure 4.3, top). Table 4.1 shows the JS parameters selected.

Table 4.1: JS parameters for simulations and real data

	Simulations		Real data
	ST	PMMA	PMMA
A	0.2	0.15	0.1
B(g/cm^2)	0.18	0.16	0.74

For the sfEBHC method, we performed an initial reconstruction, corrected with water linearization. The values above a certain threshold (f_{LOW}=0) in this initial reconstruction, mainly bone, were increased based on a non-linear transformation controlled by a parameter (η=0.001). The transformed reconstruction was projected (q) and combined with the original acquisition (p) into nine monomials, $p^i q^j$, with 0 ≤i,j≤ 2. These monomials were reconstructed (f_{ij}) and linearly combined according to

$$f_c = f_{10} + \sum_{ij}{}' c_{ij} f_{ij}, \tag{4.2}$$

where f_c is the corrected image and c_{ij} the coefficients, which were automatically calculated by minimizing the entropy f_c. The primed sum indicates that f_{00}, f_{10} and f_{01} are

excluded from the linear combination.

Both the JS method and sfEBHC were evaluated with the different options for prior water-linearization step: using both ideal (soft tissue) and realistic (PMMA) calibration phantoms in simulations and the phantom made of PMMA shown in Figure 4.5 in real data.

1DIterBH was also evaluated with the two options used for the JS method: using both ideal (soft tissue) and realistic (PMMA) calibration phantoms in simulations and the phantom made of PMMA in real data. Parameters selected for 1DIterBH were similar to those of the JS method (Table4.2).

Table 4.2: DStatBH parameters for simulations and real data

	Simulations		Real data
	ST	PMMA	PMMA
A	3.7	3.66	0.1
B(g/cm^2)	0.13	0.13	0.73

The calibration needed for 2DCalBH and CalIterBH used the geometry proposed in subsection 3.2.1 and evaluation was also done for two phantoms: (1) an ideal phantom made up of soft tissue and bone, for simulations and (2) the more realistic phantom made up of PMMA and AL6082 both for simulations and real data described in subsection 3.2.1.

Table 4.3 shows the regularization parameters and the number of iterations and subsets used for each iterative method.

Table 4.3: Regularization parameters for reconstruction iterative methods

	Simulated data		Real data	
	Standard dose	Low dose	Standard dose	Low dose
Beta	1	10	10	20
Delta	0.01	0.01	0.01	0.01
iterations	50	50	20	20
Subsets	12	12	12	12

Chapter 5

Results

This chapter presents the results in simulated and real rodent data for standard- and low-dose scenarios.

5.1 Simulated data

Figure 5.1 shows the calibration slice in the digimouse study reconstructed with the implemented post-processing methods for the standard-dose scenario. Since FDK+WL only accounts for the beam-hardening effect of water, it only corrects the cupping artifacts, leaving the dark bands uncorrected (see white arrows in Figure 5.1). In contrast, FDK+sfEBHC shows a certain overcorrection of the dark bands with both calibrations. FDK+JS, FDK+2DCalBH and FDK+FreeCalBH result in a good correction of both cupping and dark bands, independently of the calibration phantom used.

When evaluating slices with a different bone distribution than that of the calibration slice, we can see that FDK+JS performs an overcorrection of the dark bands (see white arrows in Figure 5.2). FDK+sfEBHC also shows a worse performance (stronger overcorrection of the dark bands) for this slice in comparison to the calibration slice. In contrast, FDK+2DCalBH and FDK+FreeCalBH result in an optimum correction of both artifacts independently of the distribution of bone and soft tissue in the slice.

Table 5.1 shows the RMSE with respect to the monochromatic reconstruction for all the post-processing strategies in the standard-dose scenario. As expected, FDK+WL does not recover the ideal attenuation values, showing the highest error of all the methods, especially in bone. FDK+JS has a lower error than FDK+WL but does not completely recover the ideal values of soft tissue due to the undercorrection in some slices. FDK+sfEBHC has a higher error than FDK+JS due to the overcorrection of the dark bands and an overestimation of bone. In contrast, both FDK+2DCalBH and FDK+FreeCalBH are the methods that best recover the attenuation values of the soft tissue, with the lowest RMSE of all the

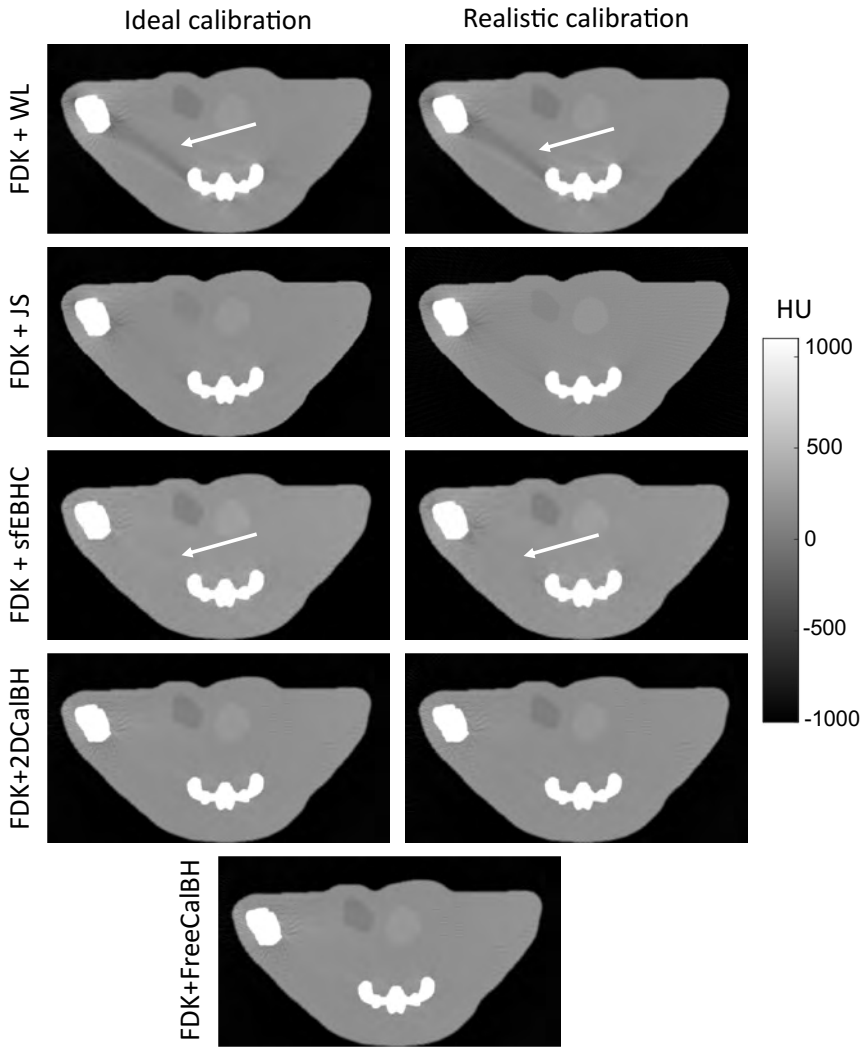

Figure 5.1: Calibration slice reconstructed with the different post-processing methods in the standard- dose scenario. White arrows indicate dark-band artifacts.

compared methods. The slightly higher error in bone for FDK+FreeCalBH compared to FDK+2DCalBH might be due to the lack of data for obtaining the beam-hardening and monochromatic functions.

Figure 5.3 shows the calibration slice and another slice with a different distribution of bone reconstructed with the iterative methods. PWLS assumes a monochromatic source, thus, it does not correct any of the beam-hardening artifacts nor recovers the true density values of the tissues (Table 5.2). FreeIterBH corrects the beam-hardening artifacts and recovers the true density, resulting in the lowest RMSE values. Similar results are found with CalIterBH with the ideal calibration phantom, whereas using the realistic one results in a bias in soft tissue (Figure 5.3 and Table 5.2). 1DIterBH is not able to correct the beam-hardening artifacts in the whole volume (see white arrow in Figure 5.3) resulting in an RMSE similar to CalIterBH with the realistic calibration phantom.

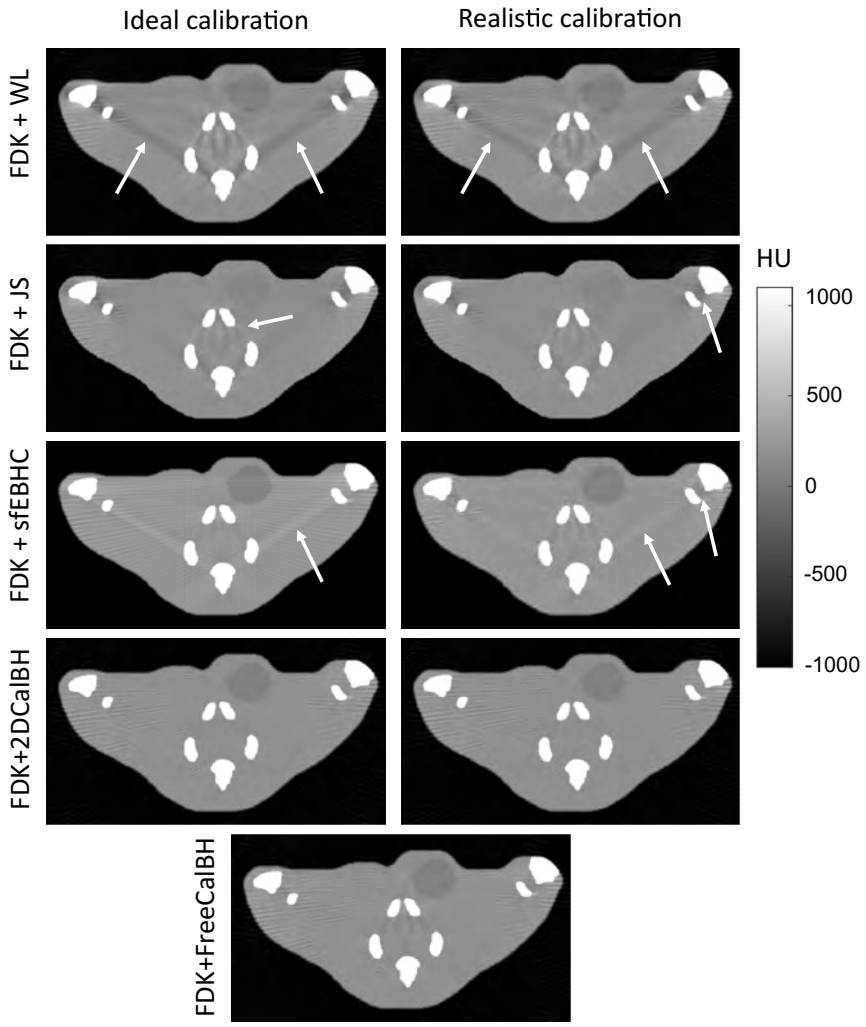

Figure 5.2: Slice with a different bone distribution than the calibration slice reconstructed with the different post-processing methods in the standard-dose scenario. White arrows indicate dark-band artifacts.

The correction of the beam-hardening artifacts in the low-dose scenario is similar to that for the standard-dose scenario, with FDK+2DCalBH and FDK+FreeCalBH being the only methods that are able to correct the beam-hardening artifacts independently of the bone distribution (see Figures 5.4 and 5.5). Nevertheless, as expected, all post-processing methods showed an enhancement of the streak artifacts probably due to the wrong segmentation of the bone, with a 25% increase of the RMSE (Table 5.3). This enhancement of the streak artifacts hinders the detection of other tissues such as muscle (see Figure 5.4).

Table 5.1: RMSE of the post-processing methods in the standard-dose scenario with respect to the true attenuation values (HU)

Method		ST	Bone	Image
FDK	-	117.68	571.56	226.84
FDK+WL	ST	62.16	295.97	116.47
	PMMA	63.07	289.01	115.13
FDK+JS	ST	41.53	145.56	62.23
	PMMA	38.20	150.19	62.89
FDK+sfEBHC	ST	49.54	1722.98	571.65
	PMMA	48.32	1372.31	455.95
FDK+2DCalBH	ST-Bone	19.28	145.15	50.58
	PMMA-AL6082	35.05	121.38	50.14
FDK+FreeCalBH	-	19.26	177.64	61.54

Table 5.2: RMSE of the iterative strategies in the standard-dose scenario with respect to the true-density values (HU)

Method		ST	Bone	Image
FDK	-	148.54	282.3	788.64
PWLS	-	132.4	294.3	860.3
1DIterBH	ST	93.9	97.3	92.7
	PMMA	100.95	66.5	100.02
CalIterBH	ST-Bone	37.9	50.5	45.1
	PMMA-AL6082	100.2	65.2	100.1
FreeIterBH	-	25.7	58.2	32.3

Table 5.3: RMSE of the post-processing methods in the low-dose scenario with respect to the true attenuation values (HU)

strategy		ST	Bone	Image
FDK	-	152.78	583.44	239.25
FDK+WL	ST	186.35	350.75	210.70
	PMMA	184.97	343.46	208.35
FDK+JS	ST	189.80	266.51	199.73
	PMMA	172.51	221.92	178.76
FDK+sfEBHC	ST	222.89	2021.74	688.94
	PMMA	223.84	2063.18	701.99
FDK+2DCalBH	ST-Bone	190.21	203.85	191.82
	PMMA-AL6082	196.81	185.50	195.74
FDK+FreeCalBH	-	183.51	256.98	192.9

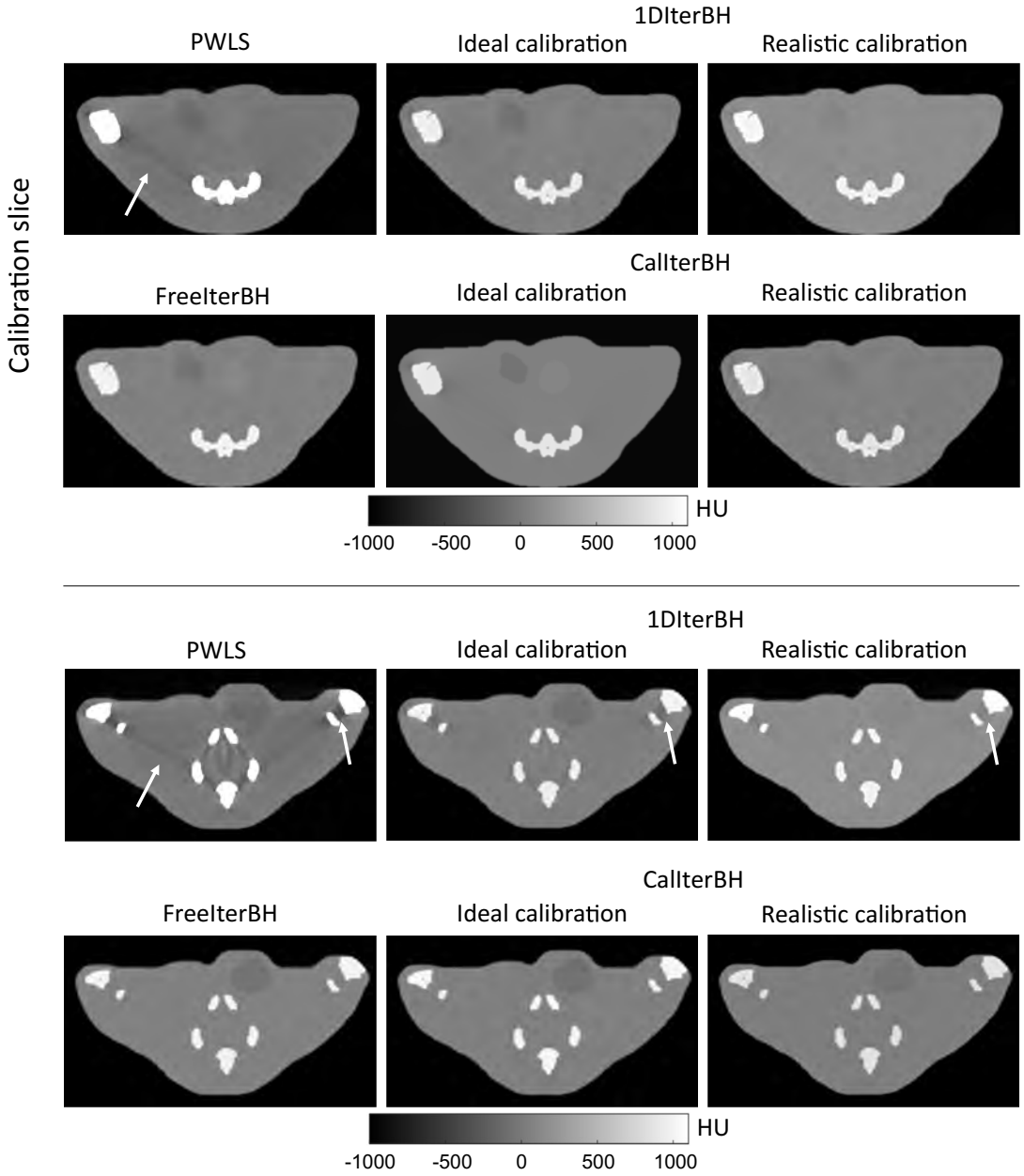

Figure 5.3: Calibration slice and another axial slice with a different bone distribution reconstructed with the iterative methods in the standard-dose scenario. White arrows indicate dark-band artifacts.

Figure 5.6 shows the results of the digimouse for the low-dose scenario reconstructed with the iterative methods. The model of the noise and the regularization term used in these methods achieve a complete elimination of the streaks and noise. Correction of the beam-hardening artifacts is similar to the one found in the standard-dose scenario, visually (Figure 5.6) and quantitatively (Table 5.4).

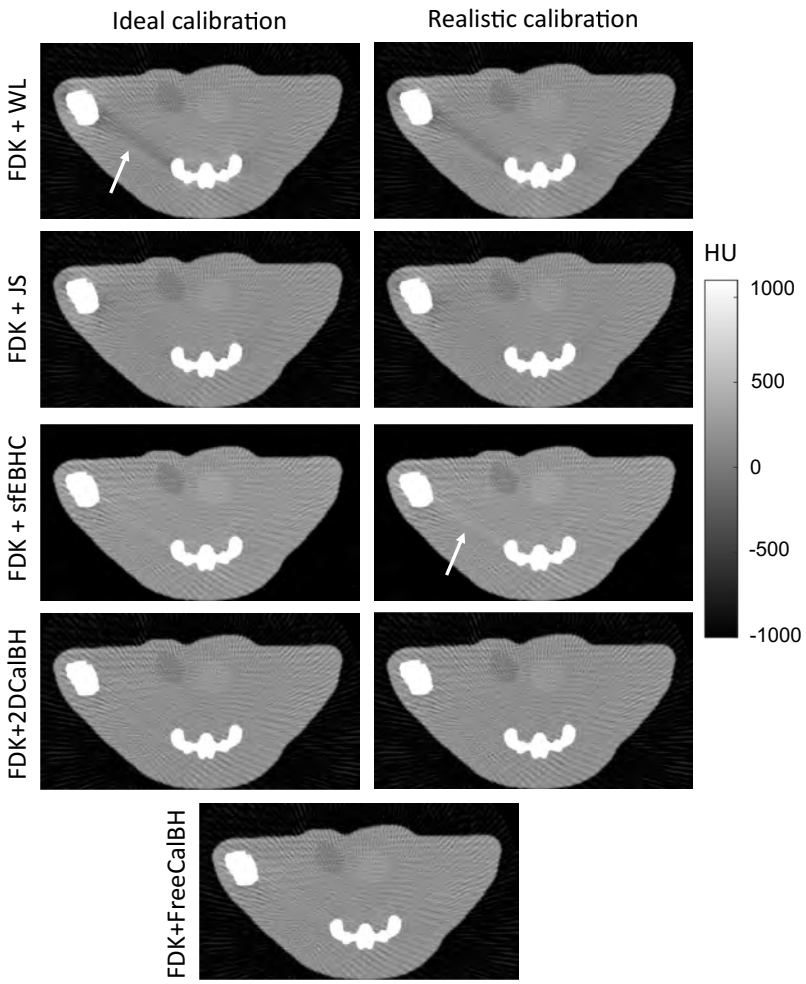

Figure 5.4: Calibration slice reconstructed with the different post-processing methods in the low-dose scenario. White arrows indicate dark-band artifacts.

Table 5.4: RMSE of the iterative strategies in the low-dose scenario with respect to the true-density values (HU)

strategy		ST	Bone	Image
FDK	-	169.93	2852.3	793.1
PWLS	-	119.51	2962.4	284.97
1DIterBH	ST	28.8	63.55	37.23
	PMMA	106.88	64.53	106.92
CalIterBH	ST	20.24	48.39	27.22
	PMMA-AL6082	102.57	65.91	101.22
FreeIterBH	-	28.36	63.40	35.2

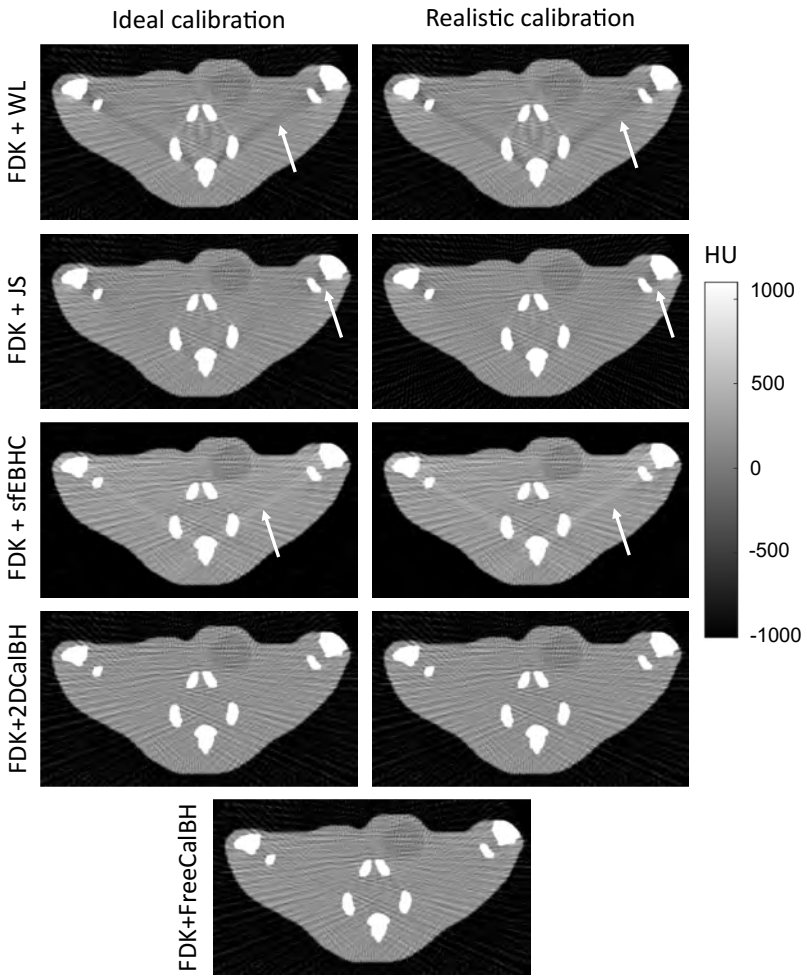

Figure 5.5: Axial slice with a different bone distribution than the calibration slice reconstructed with the different post-processing methods in the low-dose scenario. White arrows indicate dark-band artifacts.

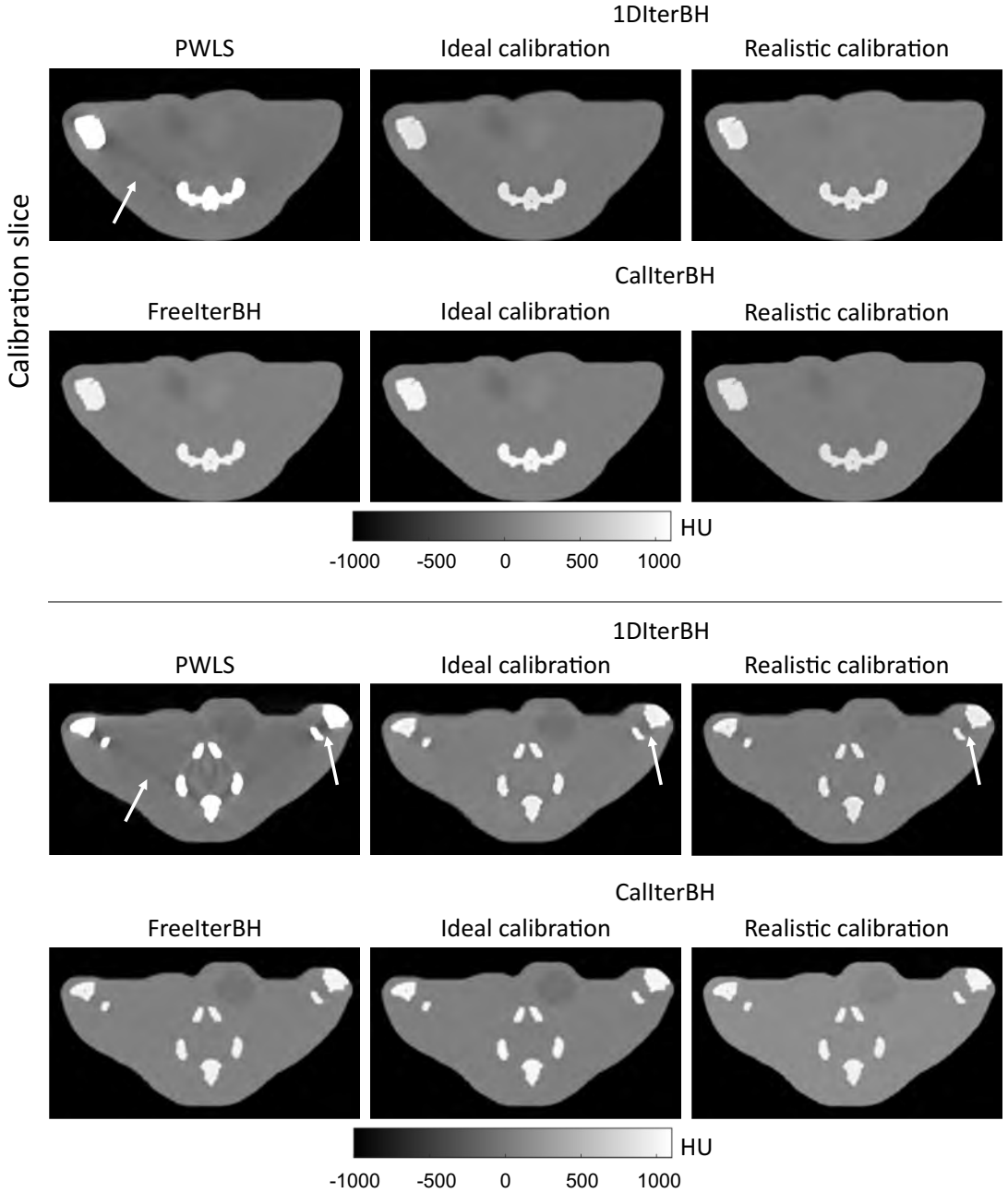

Figure 5.6: Calibration slice and another axial slice with a different bone distribution reconstructed with the iterative methods in the low-dose scenario. White arrows indicate dark-band artifacts.

5.2 Real data

Figures 5.7 and 5.8 show the results of the post-processing methods and DeepBH for the standard-dose scenario. As in the simulated data, FDK+WL does not correct the dark bands (see white arrows in Figures 5.7 and 5.8). FDK+JS corrects the dark bands in the calibration slice but undercorrects the slices with a different bone distribution. FDK+sfEBHC produces a bias in the soft tissue and corrects the calibration slice, but results in an overcorrection in slices with different bone distribution. FDK+2DCalBH, FDK+FreeCalBH and FDK+DeepBH perform a good correction of the dark bands independently of the bone distribution for the head study. Nevertheless, FDK+FreeCalBH produces an overcorrection of the dark bands in the calibration slice for the abdomen study. FDK+DeepBH is the only strategy that achieves a reduction of noise in the image.

Figures 5.9 and 5.10 show the results of the iterative strategies for the standard-dose scenario. As expected, PWLS does not correct the dark bands while 1DIterBH corrects the dark bands of the calibration slice and slightly undercorrects slices with a different bone distribution (see white arrows in Figures 5.9 and 5.10). CalIterBH completely corrects the dark bands in all the slices of the two studies, but FreeIterBH slightly overcorrects the calibration slice in the abdomen study.

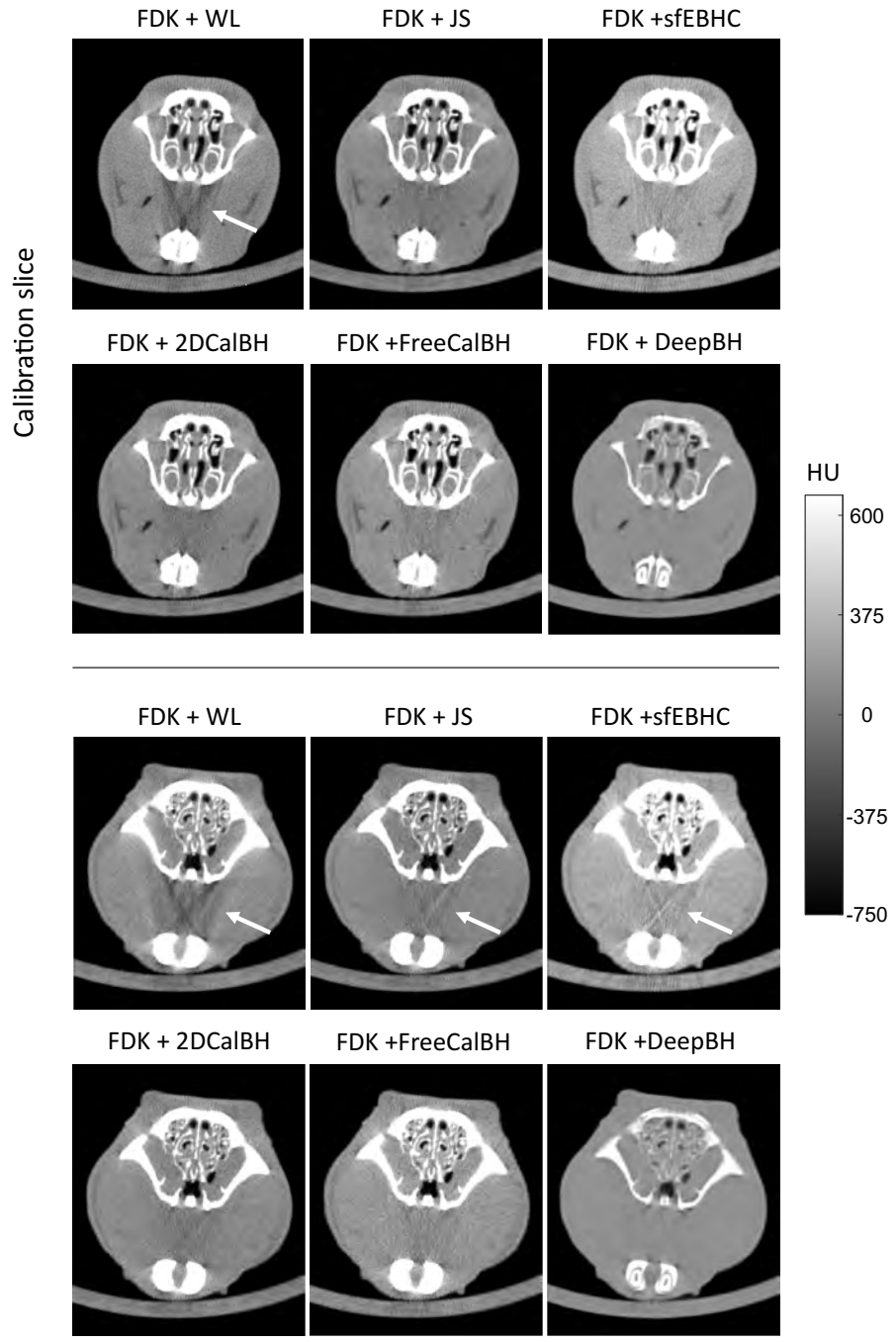

Figure 5.7: Calibration slice and another slice with a different distribution of bone of the head study reconstructed with the different post-processing methods and FDK+DeepBH in the standard-dose scenario. White arrows indicate dark-band artifacts.

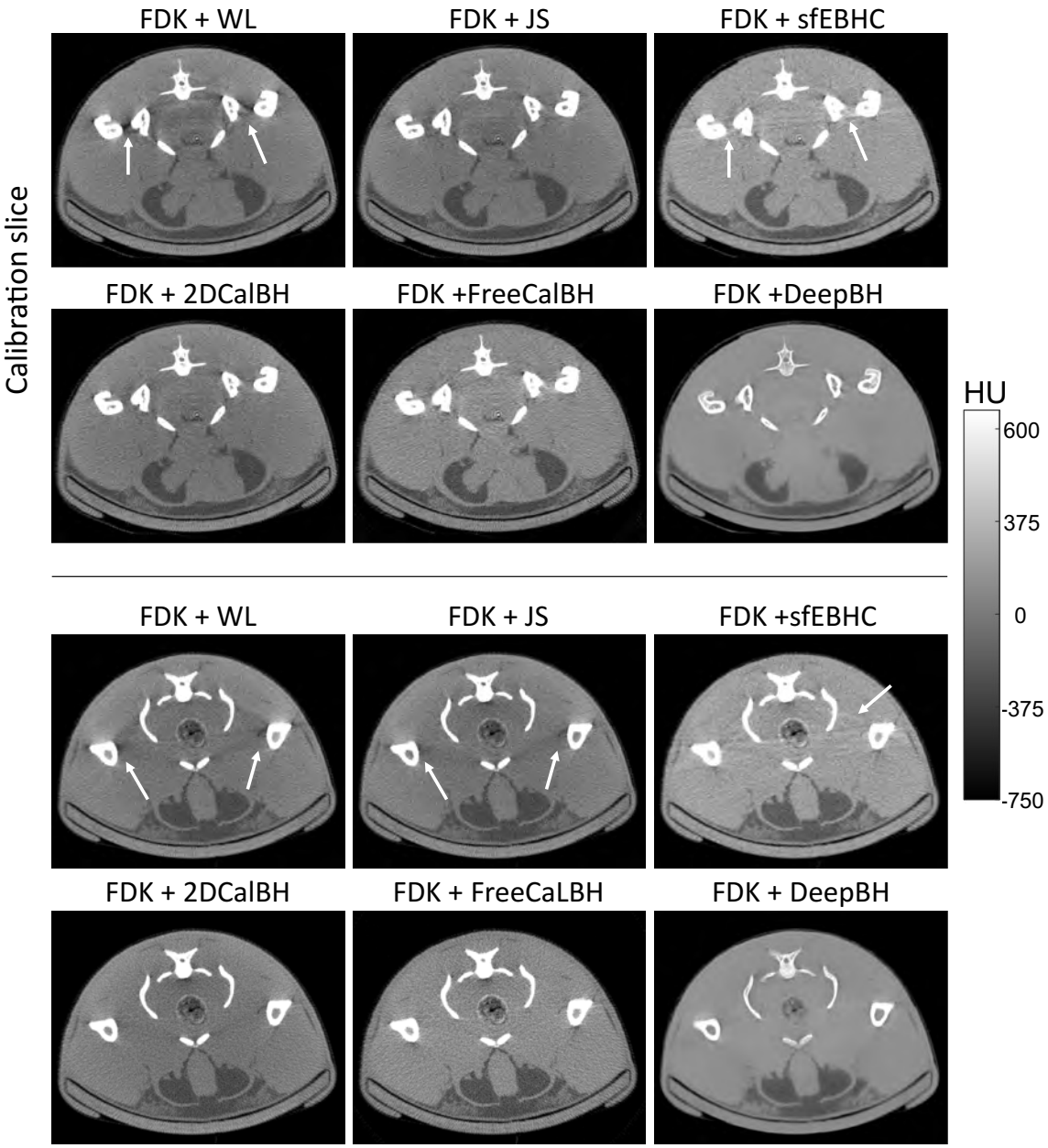

Figure 5.8: Calibration slice and another slice with a different distribution of bone of the abdomen study reconstructed with the different post-processing methods and FDK+DeepBH in the standard-dose scenario. White arrows indicate dark-band artifacts.

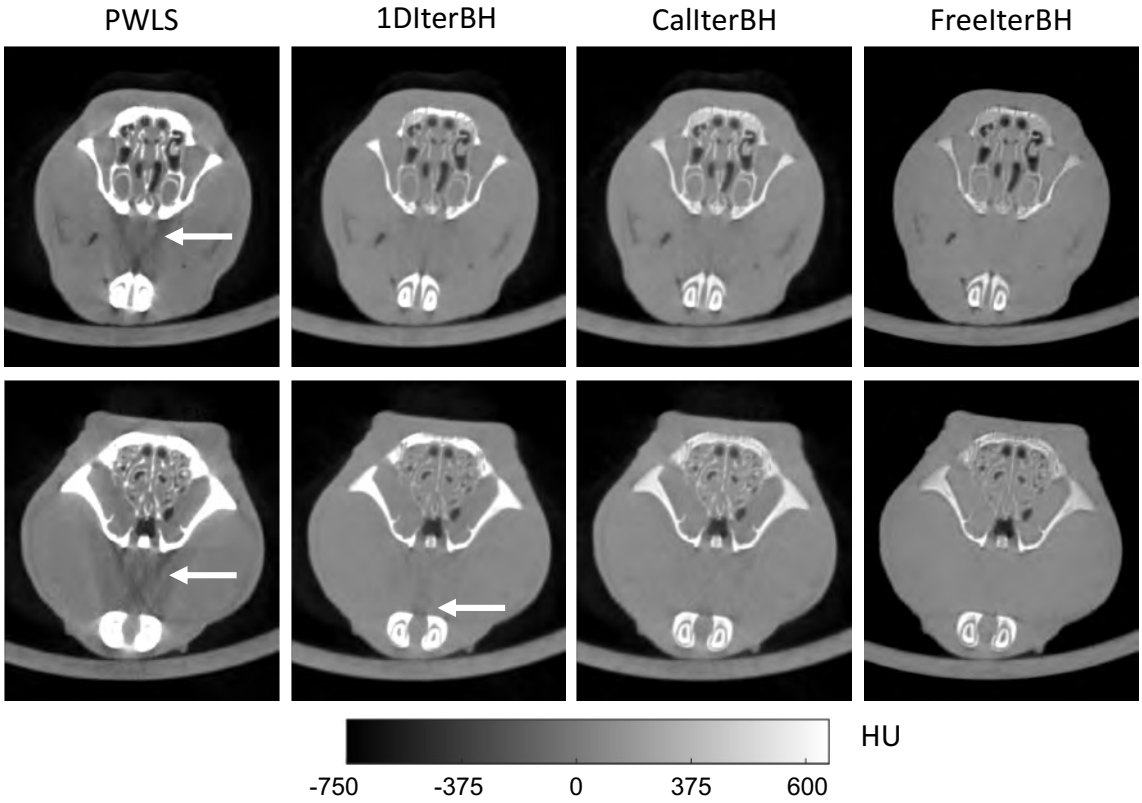

Figure 5.9: Calibration slice and another slice with a different distribution of bone of the head study reconstructed with the different reconstruction iterative methods in the standard-dose scenario. White arrows indicate dark-band artifacts.

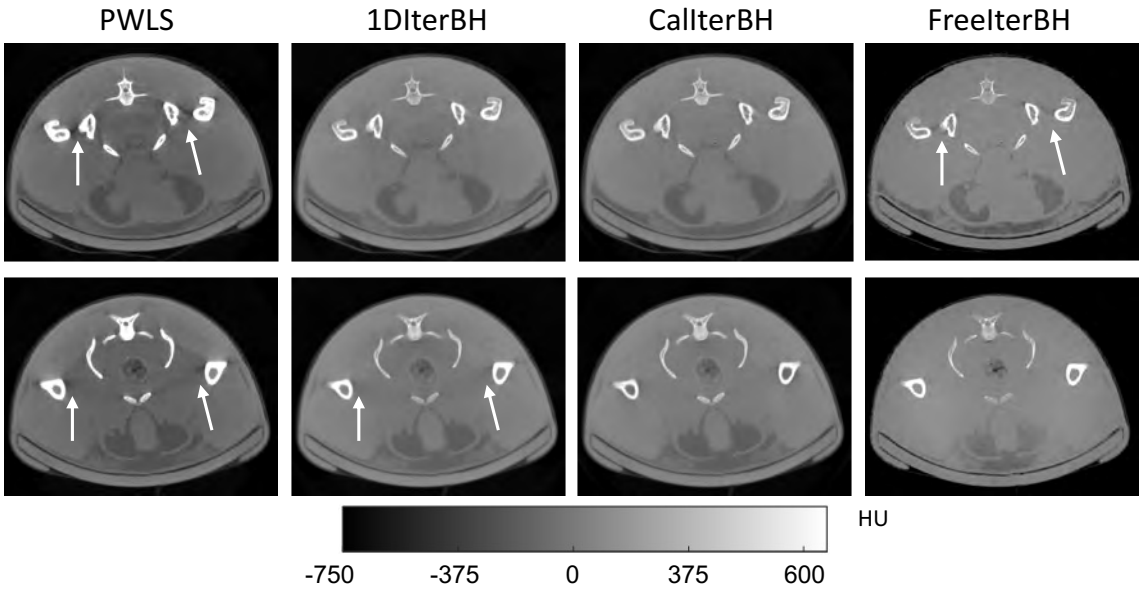

Figure 5.10: Calibration slice and another slice with a different distribution of bone of the abdomen study reconstructed with the different reconstruction iterative methods in the standard-dose scenario. White arrows indicate dark-band artifacts.

Figure 5.11 shows the axial slices with and without contrast agent reconstructed with the post-processing strategy and FDK+DeepBH. FDK+JS fails in the slices with contrast agent (see white arrows in Figure 5.11), while it corrects the dark bands of the slices without contrast agent. FDK+sfEBHC overcorrects some of the dark bands and produces a visible bias in the whole volume. FDK+2DCalBH corrects the dark bands produced by bone but overcorrects the dark bands associated with the contrast agent. The beam-hardening model of FDK+FreeCalBH seems to be affected by the contrast agent, resulting in a suboptimal correction of all the dark bands. The streaks due to the contrast agent are enhanced by all post-processing methods. In contrast, DeepBH shows the best dark-band correction while completely removing the streaks.

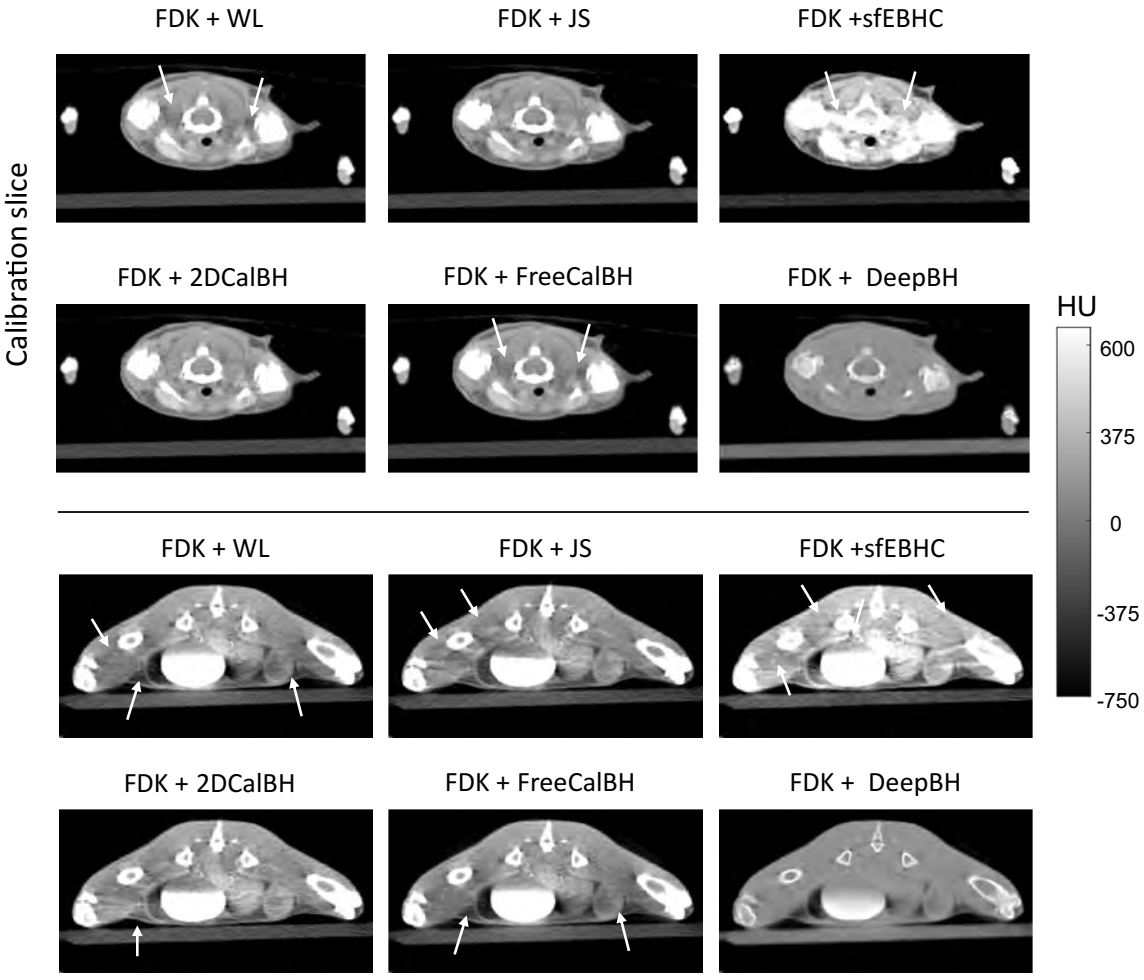

Figure 5.11: Calibration slice and another slice with a different distribution of bone of the mouse with contrast study reconstructed with the different post-processing methods and FDK+DeepBH in the standard-dose scenario. White arrows indicate dark-band artifacts.

Figure 5.12 shows the axial slice of the mouse study with and without the agent contrast reconstructed with the iterative strategies. As expected, PWLS is not able to correct the dark bands (see white arrows in Figure 5.12). 1DIterBH corrects the dark bands

produced by bone but undercorrects the ones produced by the contrast agent while FreeIterBH fails to correct any dark bands regardless of the origin. All the iterative strategies, reduce the noise and the streak artifacts produced by the contrast agent.

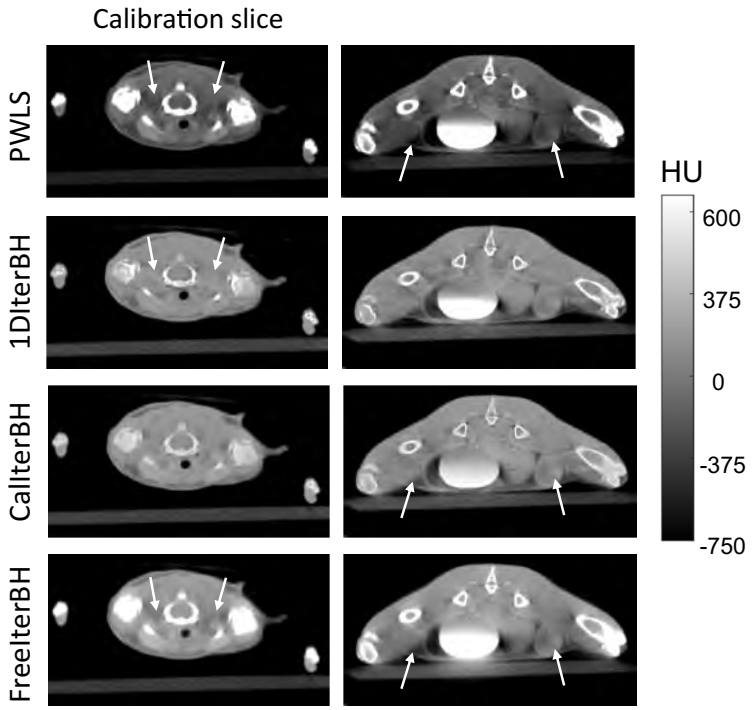

Figure 5.12: Calibration slice and another slice with a different distribution of bone of the mouse with contrast study reconstructed with the iterative methods in the standard-dose scenario. White arrows indicate dark-band artifacts.

Figures 5.13 and 5.14 show the result of the post-processing methods and FDK+ DeepBH for the low-dose scenario. In this case all the post-processing strategies enhance the low-sampling artifacts. Similar to the standard-dose scenario, FDK+WL does not correct the dark bands and FDK+JS fully corrects the dark bands of the calibration but undercorrects the other slice (see white arrows in Figures 5.13 and 5.14). FDK+sfEBHC is the strategy with more enhancement the low-sampling artifacts. This strategy also produces an overcorrection of the dark bands in several slices and a bias in all tissues (Figures 5.13 and 5.14). FDK+2DCalBH obtains a good correction of the dark bands independently of the bone distribution while FDK+FreeCalBH slightly overcorrects the dark bands depending of the slice. In contrast, FDK+DeepBH is able to cope with the low-sampling artifacts while providing a full correction of the dark bands.

Figures 5.15 and 5.16 show the reconstruction with the iterative methods in the low-dose scenario. While PWLS is able to cope with the low-sampling artifacts, it does not correct the dark bads (see white arrows in Figures 5.15 and 5.16). 1DIterBH achieves a good correction in the calibration slice but it seems to undercorrect several slices in the head study and 5.16). CalIterBH shows an optimal correction independently of the bone distribution while FreeIterBH seems to undercorrect the calibration slice in the abdomen study.

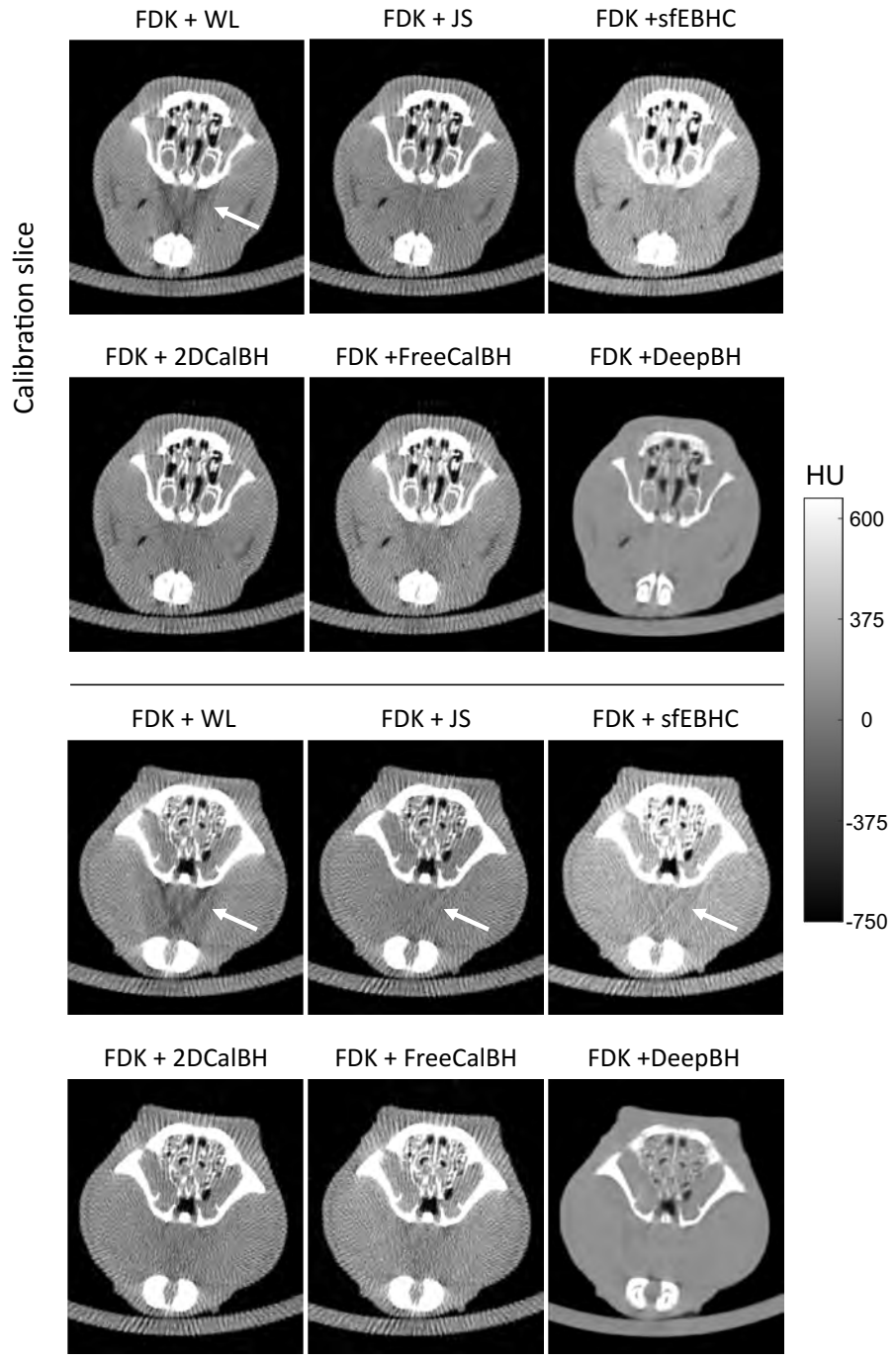

Figure 5.13: Calibration slice and another slice with a different distribution of bone of the head study reconstructed with the different post-processing methods and FDK+DeepBH in the low-dose scenario. White arrows indicate dark-band artifacts.

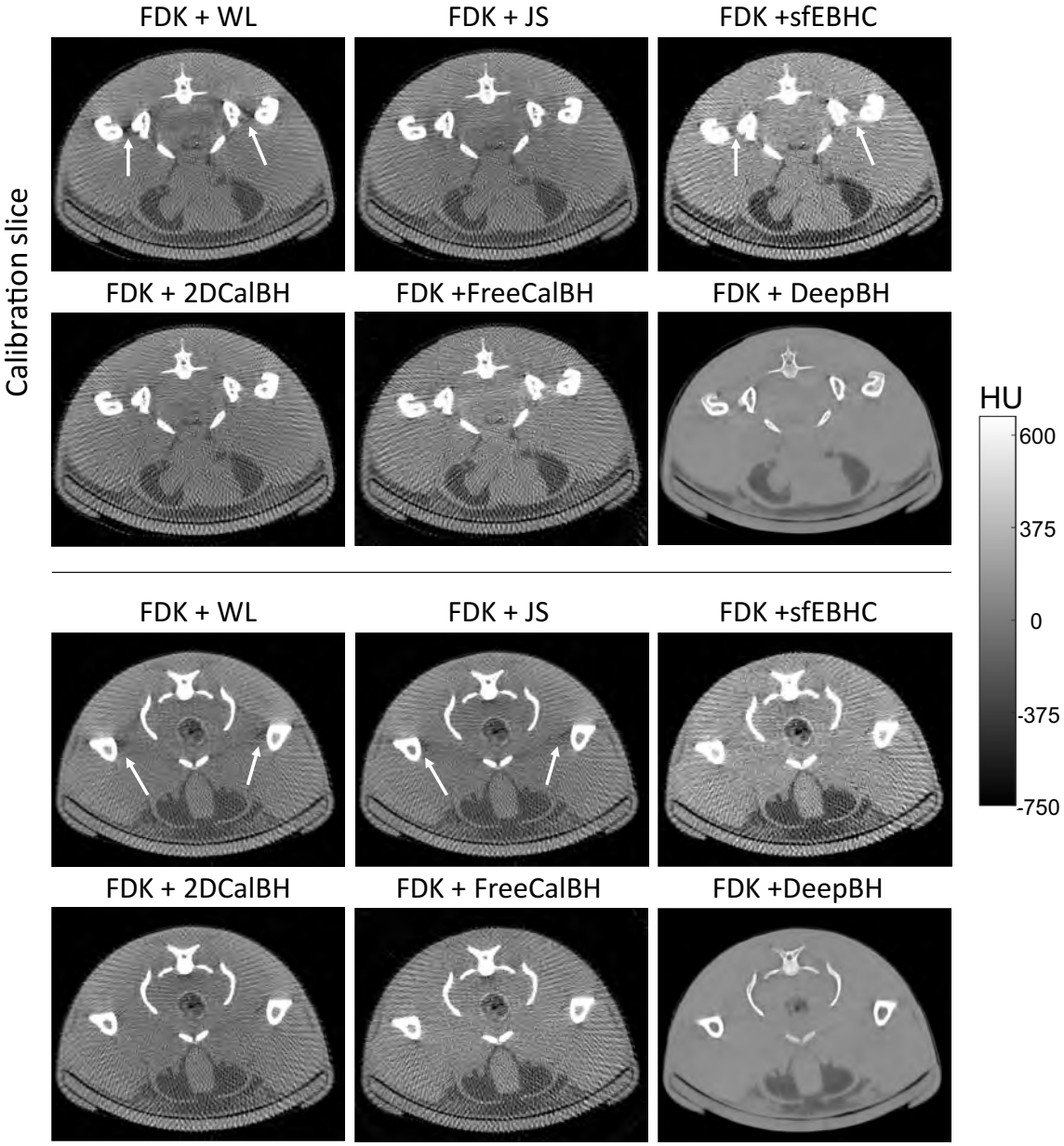

Figure 5.14: Calibration slice and another slice with a different distribution of bone of the head study reconstructed with the different post-processing methods and FDK+DeepBH in the low-dose scenario. White arrows indicate dark-band artifacts.

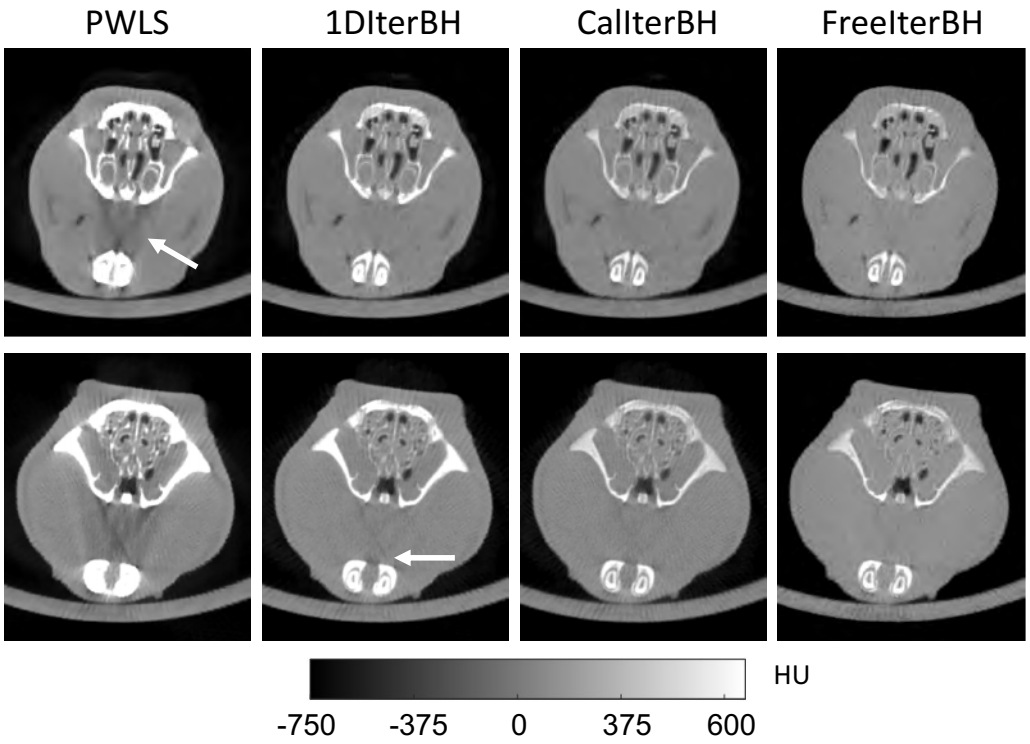

Figure 5.15: Calibration slice (top) and another slice with a different distribution of bone of the head study reconstructed with the different reconstruction iterative methods in the low-dose scenario. White arrows indicate dark-band artifacts.

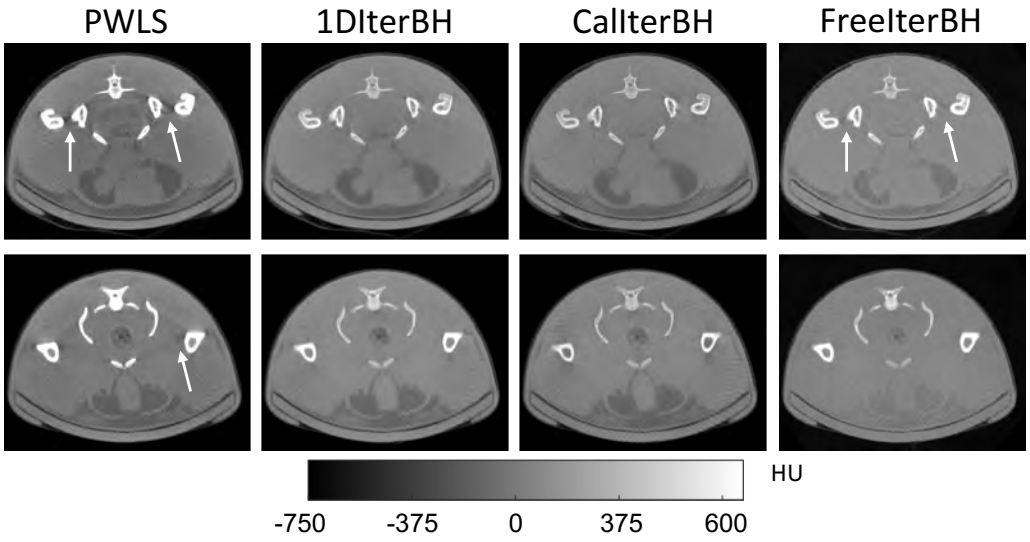

Figure 5.16: Calibration slice (top) and another slice with a different distribution of bone of the abdomen study reconstructed with the different reconstruction iterative methods in the low-dose scenario. White arrows indicate dark-band artifacts.

5.3 General comparison

This section provides a comparison of the strategies proposed in this thesis: post-processing, iterative and Deep-Learning.

Figure 5.17 and Figure 5.18 show the results of all the strategies for the standard- and low-dose scenarios. All the methods perform a good correction of the dark bands for the head study, with 1DIterBH slightly undecorrecting the artifacts since is not the calibration slice. In contrast, the abdomen study shows the calibration slice, which result in a properly correction of the dark bands of all the methods except for FDK+FreeCalBH and FreeIterBH. An increment of the streaks is observed when using the post-processing strategies in the low-dose scenarios while, as expected, iterative reconstruction methods and FDK+DeepBH showed the best performance in terms of noise and streaks.

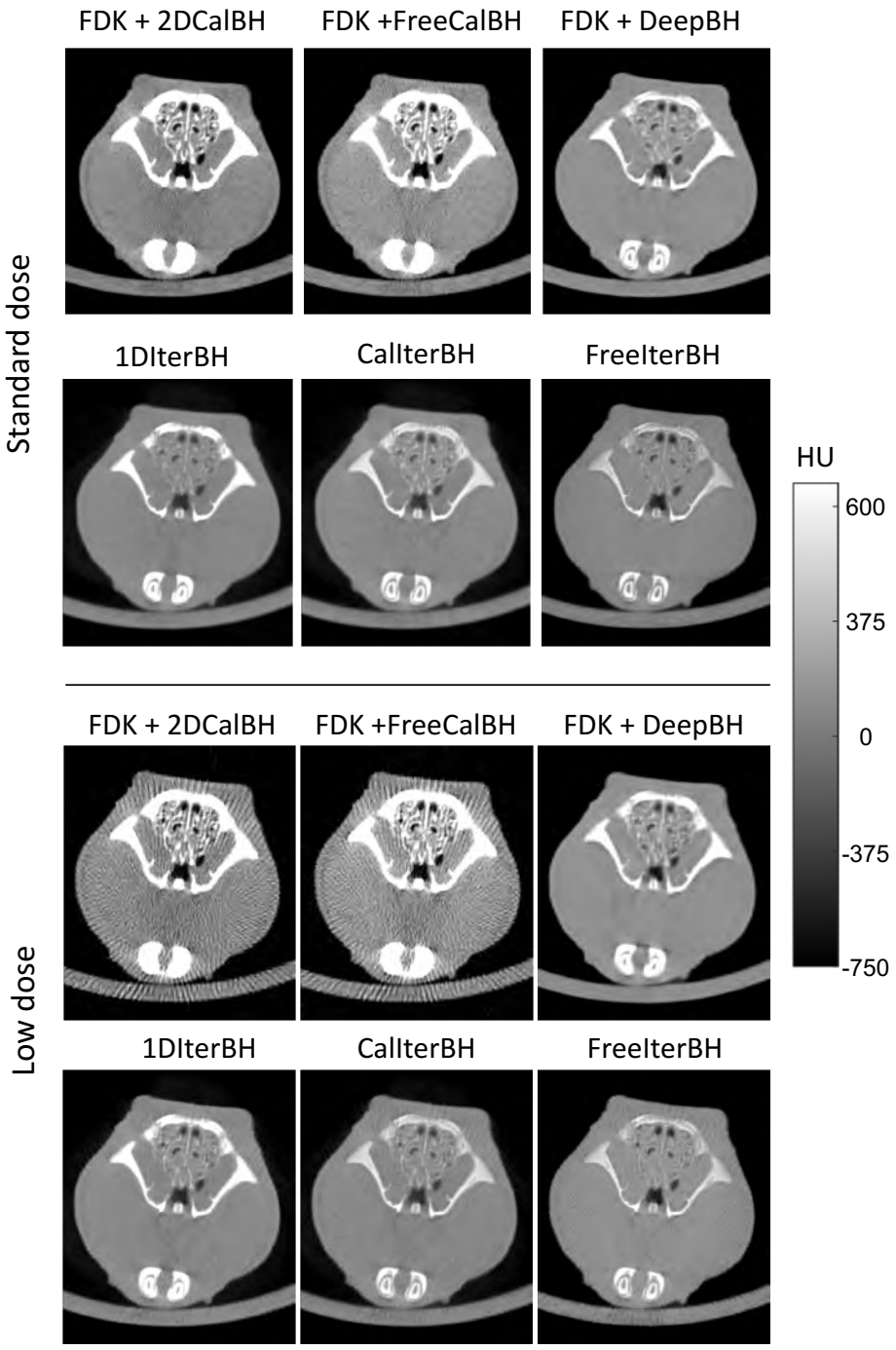

Figure 5.17: Calibration slice of the head study for the standard- and low-dose scenario reconstructed with the proposed strategies.

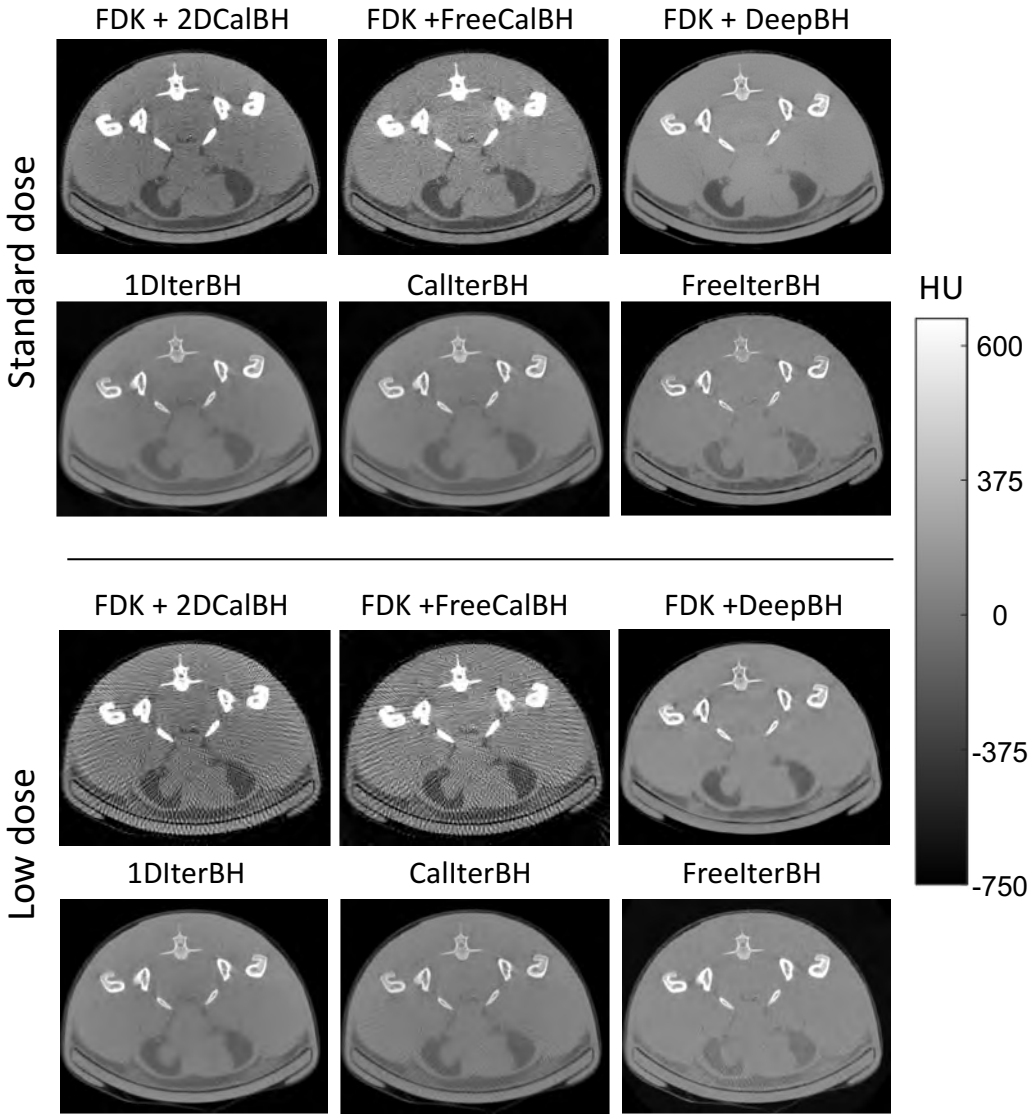

Figure 5.18: Axial slice of the head study for the standard- and low-dose scenario reconstructed with the proposed strategies.

5.3.1 Execution time

Table 5.5 shows the computational time needed for each strategy, running on a computer with an Intel Core i7-8700 CPU, 32 GB RAM, and an NVIDIA GeForce RTX2060. No effort was made to optimize the execution time. Since FDK+WL only applies a simple algebraic operation to the projections, it results in the lowest computational time. FDK+JS adds a preliminary reconstruction followed by a projection of a bone segmentation, which results in the second or third lowest execution time depending on the number of projections. The application of the linearization function to each projection pixel in FDK+2DCalBH adds 70 % of execution time with respect to FDK+JS. FDK+FreeCalBH includes an extra projection and the generation of the linearization functions, which result in an increment of a 50 % of execution time with respect to FDK+2DCalBH. In FDK+sfEBHC there are seven extra projections and backprojections together with an iterative optimization method, which in our case run for 16 iterations (25 seconds per iteration), resulting in a execution increase of 500 % with respect to FDK+FreeCalBH. All iterative strategies have higher computational times. PWLS is the iterative method with the lowest computational time, since it does not account for the beam-hardening effect and only needs a projection and a backprojection at each subset . In contrast, FreeIterBH and CalIterBH need three extra projections to account for the energy effect, which increase the execution time in a 75 %. The update of the beam-hardening function at each iteration takes 78 seconds, resulting in an extra a 5 % of execution time with respect to FreeIterBH and CalIterBH. FDK+DeepBH results in one of the lowest execution time together with the JS method, taking only 0.5 seconds per slice to correct the preliminary reconstruction.

Table 5.5: Execution time of each strategy (seconds)

	Standard dose	Low dose
FDK	10.4	6.3
FDK+WL	10.4+0.2	6.3+0.1
FDK+JS	10.4+33.3	6.3+22.4
FDK+sfEBHC	10.4+209.6	6.3+160.4
FDK+2DCalBH	10.4+59.9	6.3+42.7
FDK+FreeCalBH	10.4+95.4	6.3+52.9
FDK+DeepBH	10.4+28.7	6.3+28.7
PWLS	16800	16560
1DIterBH	28800	28080
CalIterBH	28800	28080
FreeIterBH	30360	29380

Chapter 6

Discussion, conclusions, and future lines

This thesis proposes a bundle of reconstruction strategies with beam-hardening compensation for the common scenarios found in preclinical research: cross-sectional and longitudinal studies.

For the cross-sectional studies, where the radiation dose is not an issue and allows the use of standard-dose protocols, the proposed strategy is an analytical reconstruction followed by a fast post-processing step. The proposed post-processing methods extend the water-linearization to correct both cupping and dark-bands, based on the characterization of the beam-hardening effect for soft-tissue and bone from empirical measurements. The characterization of the beam-hardening effect is based on two approaches: 1) 2DCalBH, which uses a calibration phantom composed of bone and soft-tissue equivalent materials, and 2) FreeCalBH, which uses the information provided by the sample, with the idea of fine-tunning the correction to the specific attenuation coefficients of the sample that may differ from those of the equivalent materials in the calibration phantom. Both methods avoid the need for knowledge of the spectrum [5], the tuning parameters [6] or extra projections and backprojections [7, 8] of previous works.

Despite of an exhaustive search of optimum parameters for the whole volume with the classical post-processing strategy proposed by Joseph and Spital [6], (JS), no unique set of parameters resulted in a proper correction of all the slices; thus, the parameters for simulated and real data were obtained taking into account one representative slice of each study. This might indicate that the two-parameter model proposed in the JS method cannot fully characterize different combinations of soft tissue and bone thicknesses. In contrast, results in simulations and real data showed that the two proposed post-processing methods generate a better correction model that resulted in proper compensation of the dark bands for the whole volume independently of the combination of soft tissue and bone in each slice.

Evaluation of the proposed post-processing methods also showed a better correction

of the dark bands in comparison to one of the latest and most cited method found in the literature, sfEBHC, proposed by Schuller et al [8]. Apart from an overcorrection of the dark bands, as reported by the authors, we found that sfEBHC is highly dependent on the initial weights of the optimization problem, in contrast to the proposed strategy that only relies on empirical measurements. Both proposed post-processing methods, 2DCalBH and FreeCalBH, showed similar correction of the dark bands in simulated data, but evaluation on real data showed that FreeCalBH had a slightly lower performance in the abdomen study. This may be due to a lack of soft-tissue and small bone combinations to extrapolate a proper model of the beam-hardening effect. Therefore, 2DCalBH would be the prefered option for most studies, while FreeCalBH could be a good alternative when the attenuation properties of the bone in the sample greatly differs from the equivalent material used in the calibration (e.g., in the presence of osteoporosis or osteopetrosis). The main limitation of the proposed post-processing methods, shared by previous post-processing schemes, is the need for a preliminary bone segmentation. Evaluation of low-dose studies showed that errors in this bone segmentation hinder the selection of the appropriate linearization functions, which leads to inconsistent data in the corrected projection values. In particular, streaks produced by low-sampling may have similar values than bone and, thus, be included in the bone mask. Since an optimum post-processing method would increase the bone values because they are underestimated due to the beam-hardening effect, the streak artifacts will be enhanced.

For the longitudinal studies, where the reduction of radiation dose is advisable to assure the survival of the animal and to avoid confounding factors, the proposed reconstruction strategy is based on an iterative method with three different characterizations of the beam-hardening effect into the forward model, also avoiding the need of the knowledge of the spectrum of previously proposed polychromatic iterative methods [11, 35]. The first approach, 1DIterBH, explores the idea of the JS method, which characterizes the beam-hardening effect with the 1D function corresponding to water, already available in most scanners, plus two empirical parameters. The second (CalIterBH) and third (FreeIterBH) approaches empirically obtain the beam-hardening function of the soft tissue and bone, similar to 2DCalBH and FreeCalBH, respectively. Finally, Deep-Learning was explored with the idea of obtaining a joint solution that would require low-computational time while compensating the beam-hardening artifacts regardless the dose scenario, like that of iterative methods. The proposed Deep-Learning approach, DeepBH, eliminates the limitations due to memory constraints found in the only method alike in the literature [16].

As expected, the proposed iterative reconstruction strategy reduced the low-sampling artifacts outperforming the post-processing strategy in the low-dose scenario. 1DIterBH did not correct the beam-hardening artifacts in the whole volume with unique set of parameter values, expected as it used a similar approximation to the JS method. CalIterBH and FreeIterBH achieve a global optimum correction, with slightly lower performance in

the abdomen study of the latter, similar to FreeCalBH.

Despite the good results obtained with the proposed iterative strategy, it requires high computational time, hindering its use for real-time applications. DeepBH showed to be a viable alternative for any dose scenario, combining the good artifact compensation of the iterative reconstruction with a considerable reduction of computational time. However, the selection of the simple cost function MSE may be responsible for the slight loss of spatial resolution that can be appreciated in the results. Future work will explore if it would be interesting the use of more complex cost function such as perceptual loss [82] or Structural Similarity Index (SSSIM) [83]. The CalIterBH method, which showed the best correction of all the iterative methods, was used as the gold standard, since acquiring the rodent studies with a monochromatic source was not possible. A different model was needed for each dose scenario, probably because the small size and low variability of the training set did not allow the network to generalize the correction of the dark bands with and without the presence of low-sampling artifacts. The low variability of the training data may also be the reason why a different model was needed for each anatomical part. Future work will evaluate if an increase in the amount of training data would enable a single model to work independently of the dose scenario or the anatomical part under study.

Evaluation on a mouse study contrast agent showed a worst performance of the post-processing and iterative strategies. This lack of correction is especially seen in the sample-based methods, probably due to the assumption of only two tissues, which assigned the contrast agent as bone in the beam-hardening model. Therefore, a three-class model could be necessary when contrast agents are present. The calibration phantom could add the third equivalent material in the following geometry: the same semicircle of PMMA and two halves of rounded triangles, one of AL6082 and one of contrast agent. Nonetheless, bone and iodine have similar reconstructed values and a simple threshold may be insufficient to separate both, being necessary to use other approaches, such as dynamic segmentation [84]. In contrast to proposed post-processing and iterative strategies, DeepBH also corrected the dark bands in this study, showing a good generalization of the correction independently of the tissue or material present in the sample. These results rise the interest of further exploring this path in the future to obtain single joint solution that would require low-computational time and, at the sametime, compensate the beam-hardening artifacts regardless the dose scenario.

Regarding the model of the object, the most common approach is to assume that each voxel can only be either bone or soft tissue and to segment bone from a preliminary reconstruction obtained with a fast algorithm such as filtered back-projection. This segmentation can be challenging, especially in the case of low-dose scans, which suffer from low SNR and possibly photon starvation. Furthermore, this model neglects partial volume effects, as voxels are not allowed to contain a mixture of bone and soft tissue. Our

iterative strategy addresses these problems, since we model the attenuation at each voxel by defining piecewise density-dependent tissue fractions, which are updated at each iteration, similarly to what was done in [10]. This eliminates possible segmentation problems in low-dose studies. In the proposed iterative strategy, the selection of the intervals for these functions was based on the typical densities for soft-tissue and cortical bone found in NIST. Further evaluation of the effect of the definition of these intervals on the recovered density values for both clinical and preclinical data is warranted.

The selected materials for the calibration phantom used in 2DCalBH and FreeCalBH, previously used as soft tissue and bone equivalent materials [60, 67, 70], showed a very good artifact correction both in simulations and real data. Evaluation on simulated data also showed a good recovery of the ideal values, even for bone, which was not possible in the previous literature without the knowledge of the spectrum. Future work will evaluate the quantification in real data using exvivo experiment to find out if there is a need for more sophisticated equivalent materials [85, 86, 87].

To conclude, this thesis presents a comprehensive bundle of reconstruction strategies able to cope with the beam-hardening artifacts in the common scenarios found in preclinical research: cross-sectional (standard dose) and longitudinal studies (low-dose). The incorporation of this bundle in a real scanner only needs a small modification of the calibration step already implemented in the commercial scanners. Compared to previous methods in the literature, the proposed reconstruction strategies:

- Do not need the knowledge of the spectrum.
- Are quantitative, providing real attenuation coefficients, not only for soft tissue like several previously proposed methods, but also for bone.
- Enable a fast correction of the beam-hardening artifacts in standard-dose studies with no need of heuristic selection of parameters.
- Correct the dark bands in the whole volume, independently of the combination of soft tissue and bone in each slice.
- Compared to the only one previously proposed approach with Deep Learning, the proposed DL strategy overcomes the memory constraints with the use of a simpler architecture.

The proposed bundle of reconstruction strategies will be incorporated in the new generation of micro-CT scanners commercialized by the company SEDECAL. Currently, it is also being tested in a new multipurposed C-arm system for veterinary applications developed by the same company.

Bibliography

[1] Allan Macleod Cormack. “Representation of a function by its line integrals, with some radiological applications”. In: *Journal of applied physics* 34.9 (1963), pp. 2722–2727.

[2] Godfrey Newbold Hounsfield. “A method of and apparatus for examination of a body by radiation such as X-ray or gamma radiation”. In: *Patent Specification 1283915* (1972).

[3] Julia F Barrett and Nicholas Keat. “Artifacts in CT: recognition and avoidance”. In: *Radiographics* 24.6 (2004), pp. 1679–1691.

[4] Gabor T Herman. “Correction for beam hardening in computed tomography”. In: *Physics in Medicine & Biology* 24.1 (1979), p. 81.

[5] O Nalcioglu and RY Lou. “Post-reconstruction method for beam hardening in computerised tomography”. In: *Physics in Medicine & Biology* 24.2 (1979), p. 330.

[6] Peter M Joseph and Robin D Spital. “A method for correcting bone induced artifacts in computed tomography scanners.” In: *Journal of computer assisted tomography* 2.1 (1978), pp. 100–108.

[7] Yiannis Kyriakou, Esther Meyer, Daniel Prell, and Marc Kachelrieß. “Empirical beam hardening correction (EBHC) for CT”. In: *Medical physics* 37.10 (2010), pp. 5179–5187.

[8] Sören Schüller et al. “Segmentation-free empirical beam hardening correction for CT”. In: *Medical physics* 42.2 (2015), pp. 794–803.

[9] Bruno De Man, Johan Nuyts, Patrick Dupont, Guy Marchal, and Paul Suetens. “An iterative maximum-likelihood polychromatic algorithm for CT”. In: *IEEE transactions on medical imaging* 20.10 (2001), pp. 999–1008.

[10] Idris A Elbakri and Jeffrey A Fessler. “Segmentation-free statistical image reconstruction for polyenergetic x-ray computed tomography with experimental validation”. In: *Physics in Medicine & Biology* 48.15 (2003), p. 2453.

[11] Idris A Elbakri. “Statistical reconstruction algorithms for polyenergetic X-ray computed tomography”. PhD thesis. Citeseer, 2003.

[12] Somesh Srivastava and Jeffrey A Fessler. “Simplified statistical image reconstruction for polyenergetic X-ray CT”. In: *IEEE Nuclear Science Symposium Conference Record, 2005*. Vol. 3. IEEE. 2005, 5–pp.

[13] Muhammad Usman Ghani and W Clem Karl. “Deep learning based sinogram correction for metal artifact reduction”. In: *Electronic Imaging* 2018.15 (2018), pp. 472–1.

[14] Shipeng Xie et al. “Artifact removal using improved GoogLeNet for sparse-view CT reconstruction”. In: *Scientific reports* 8.1 (2018), pp. 1–9.

[15] Shaojie Chang, Xi Chen, Jiayu Duan, and Xuanqin Mou. “A CNN-Based Hybrid Ring Artifact Reduction Algorithm for CT Images”. In: *IEEE Transactions on Radiation and Plasma Medical Sciences* 5.2 (2020), pp. 253–260.

[16] Kailash Kalare, Manish Bajpai, Shubhabrata Sarkar, and Prabhat Munshi. “Deep neural network for beam hardening artifacts removal in image reconstruction”. In: *Applied Intelligence* (2021), pp. 1–20.

[17] JJ Vaquero et al. “Assessment of a new high-performance small-animal X-ray tomograph”. In: *IEEE transactions on nuclear science* 55.3 (2008), pp. 898–905.

[18] Monica Abella, Cristobal Martinez, Ines Garcia, Patricia Moreno, Claudia De Molina, and Manuel Desco. “Tolerance to geometrical inaccuracies in CBCT systems: A comprehensive Study”. In: *Medical Physics* (2021).

[19] Jeffrey A Fessler and ISBI Tutorial. “Iterative methods for image reconstruction”. In: *ISBI Tutorial. Arlington Virginia: April* (2006).

[20] A.C. Kak and M. Slaney. *Principles of Computerized Tomographic Imaging*. Classics in Applied Mathematics. Society for Industrial and Applied Mathematics, 2001.

[21] M Abella. “Contributions to Image Reconstruction in High-Resolution Multimodality Systems for Preclinical Applications”. In: *Unidad de Medicina y Cirugia Experimental. Hospital General Universitario Gregorio Marañon, Universidad Politecnica de Madrid, Madrid* (2010).

[22] Jiang Hsieh. *Computed tomography: principles, design, artifacts, and recent advances*. Vol. 114. SPIE press, 2003.

[23] Faycal Kharfi. “Mathematics and physics of computed tomography (CT): demonstrations and practical examples”. In: *Imaging and radioanalytical techniques in interdisciplinary research-fundamentals and cutting edge applications* (2013), pp. 82–106.

[24] Carl R Crawford. “CT filtration aliasing artifacts”. In: *IEEE transactions on medical imaging* 10.1 (1991), pp. 99–102.

[25] Yi Du, Gongyi Yu, Xincheng Xiang, and Xiangang Wang. “GPU accelerated voxel-driven forward projection for iterative reconstruction of cone-beam CT”. In: *Biomedical engineering online* 16.1 (2017), pp. 1–11.

[26] Monica Abella et al. “FUX-Sim: Implementation of a fast universal simulation/reconstruction framework for X-ray systems”. In: *PloS one* 12.7 (2017), e0180363.

[27] Kunio Tanabe. “Projection method for solving a singular system of linear equations and its applications”. In: *Numerische Mathematik* 17.3 (1971), pp. 203–214.

[28] Qiaoqiao Ding, Yong Long, Xiaoqun Zhang, and Jeffrey A Fessler. “Modeling mixed Poisson-Gaussian noise in statistical image reconstruction for x-ray CT”. In: *Arbor* 1001 (2016), p. 48109.

[29] Bruce R Whiting, Parinaz Massoumzadeh, Orville A Earl, Joseph A O’Sullivan, Donald L Snyder, and Jeffrey F Williamson. “Properties of preprocessed sinogram data in x-ray computed tomography”. In: *Medical physics* 33.9 (2006), pp. 3290–3303.

[30] Jeffrey A Fessler and Hakan Erdogan. “A paraboloidal surrogates algorithm for convergent penalized-likelihood emission image reconstruction”. In: *1998 IEEE Nuclear Science Symposium Conference Record. 1998 IEEE Nuclear Science Symposium and Medical Imaging Conference (Cat. No. 98CH36255)*. Vol. 2. IEEE. 1998, pp. 1132–1135.

[31] Bruce R Whiting. “Signal statistics in x-ray computed tomography”. In: *Medical Imaging 2002: Physics of Medical Imaging*. Vol. 4682. International Society for Optics and Photonics. 2002, pp. 53–60.

[32] Jingyan Xu and Benjamin MW Tsui. “Electronic noise modeling in statistical iterative reconstruction”. In: *IEEE Transactions on Image Processing* 18.6 (2009), pp. 1228–1238.

[33] Marcel Beister, Daniel Kolditz, and Willi A Kalender. “Iterative reconstruction methods in X-ray CT”. In: *Physica medica* 28.2 (2012), pp. 94–108.

[34] Bruno De Man and Samit Basu. “Distance-driven projection and backprojection in three dimensions”. In: *Physics in Medicine & Biology* 49.11 (2004), p. 2463.

[35] Idris A Elbakri and Jeffrey A Fessler. “Statistical image reconstruction for polyenergetic X-ray computed tomography”. In: *IEEE transactions on medical imaging* 21.2 (2002), pp. 89–99.

[36] Ken Sauer and Charles Bouman. “A local update strategy for iterative reconstruction from projections”. In: *IEEE Transactions on Signal Processing* 41.2 (1993), pp. 534–548.

[37] Jean-Baptiste Thibault, Ken D Sauer, Charles A Bouman, and Jiang Hsieh. “A three-dimensional statistical approach to improved image quality for multislice helical CT”. In: *Medical physics* 34.11 (2007), pp. 4526–4544.

[38] Jeffrey A Fessler, M Sonka, and J Michael Fitzpatrick. “Statistical image reconstruction methods for transmission tomography”. In: *Handbook of medical imaging* 2 (2000), pp. 1–70.

[39] Kenneth Lange, Mark Bahn, and Roderick Little. “A theoretical study of some maximum likelihood algorithms for emission and transmission tomography”. In: *IEEE Transactions on Medical Imaging* 6.2 (1987), pp. 106–114.

[40] Jeffrey A Fessler and Scott D Booth. “Conjugate-gradient preconditioning methods for shift-variant PET image reconstruction”. In: *IEEE transactions on image processing* 8.5 (1999), pp. 688–699.

[41] Hakan Erdogan and Jeffrey A Fessler. “Monotonic algorithms for transmission tomography”. In: *5th IEEE EMBS International Summer School on Biomedical Imaging, 2002.* IEEE. 2002, 14–pp.

[42] Kenneth Lange, Richard Carson, et al. “EM reconstruction algorithms for emission and transmission tomography”. In: *J Comput Assist Tomogr* 8.2 (1984), pp. 306–16.

[43] Hakan Erdogan and Jeffrey A Fessler. “Ordered subsets algorithms for transmission tomography”. In: *Physics in Medicine & Biology* 44.11 (1999), p. 2835.

[44] F Edward Boas, Dominik Fleischmann, et al. “CT artifacts: causes and reduction techniques”. In: *Imaging Med* 4.2 (2012), pp. 229–240.

[45] Mingyu Kim et al. “Deep learning in medical imaging”. In: *Neurospine* 16.4 (2019), p. 657.

[46] Sotiris B Kotsiantis, I Zaharakis, P Pintelas, et al. “Supervised machine learning: A review of classification techniques”. In: *Emerging artificial intelligence applications in computer engineering* 160.1 (2007), pp. 3–24.

[47] Thomas Hofmann. “Unsupervised learning by probabilistic latent semantic analysis”. In: *Machine learning* 42.1 (2001), pp. 177–196.

[48] Leslie Pack Kaelbling, Michael L Littman, and Andrew W Moore. “Reinforcement learning: A survey”. In: *Journal of artificial intelligence research* 4 (1996), pp. 237–285.

[49] Batta Mahesh. “Machine Learning Algorithms-A Review”. In: *International Journal of Science and Research (IJSR).[Internet]* 9 (2020), pp. 381–386.

[50] Neena Aloysius and M Geetha. “A review on deep convolutional neural networks”. In: *2017 International Conference on Communication and Signal Processing (ICCSP)*. IEEE. 2017, pp. 0588–0592.

[51] Van Hiep Phung, Eun Joo Rhee, et al. "A high-accuracy model average ensemble of convolutional neural networks for classification of cloud image patches on small datasets". In: *Applied Sciences* 9.21 (2019), p. 4500.

[52] Olaf Ronneberger, Philipp Fischer, and Thomas Brox. "U-net: Convolutional networks for biomedical image segmentation". In: *International Conference on Medical image computing and computer-assisted intervention*. Springer. 2015, pp. 234–241.

[53] Yoseob Han and Jong Chul Ye. "Framing U-Net via deep convolutional framelets: Application to sparse-view CT". In: *IEEE transactions on medical imaging* 37.6 (2018), pp. 1418–1429.

[54] Mohamed AA Hegazy, Myung Hye Cho, Min Hyoung Cho, and Soo Yeol Lee. "U-net based metal segmentation on projection domain for metal artifact reduction in dental CT". In: *Biomedical engineering letters* 9.3 (2019), pp. 375–385.

[55] Monica Abella, Cristobal Martinez, Manuel Desco, Juan Jose Vaquero, and Jeffrey A Fessler. "Simplified Statistical Image Reconstruction for X-ray CT With Beam-Hardening Artifact Compensation". In: *IEEE transactions on medical imaging* 39.1 (2019), pp. 111–118.

[56] Cristobal Martinez, Claudia de Molina, Manuel Desco, and Monica Abella. "Simple method for beam-hardening correction based on a 2D linearization function". In: *The 4th International Meeting on Image Formation in X-Ray Computed Tomography (CTMeeting 2016)*. 2016.

[57] Cristobal Martinez, Claudia de Molina, Manuel Desco, and Monica Abella. "Calibration-free method for beam-hardening compensation: preliminary results". In: *2017 IEEE Nuclear Science Symposium and Medical Imaging Conference (NSS/MIC)*. IEEE. 2017, pp. 1–3.

[58] Cristobal Martinez, Jeffrey A Fessler, Manuel Desco, and Monica Abella. "Statistical image reconstruction with sample-based beam-hardening compensation for X-ray CT". In: *Proc. 5th Int. Conf. Image Formation X-Ray Computed Tomography*. 2018, pp. 11–14.

[59] Crisotbal Martinez, Carlos Fernandez Del Cerro, Manuel Desco, and Monica Abella. "New method for correcting beam-hardening artifacts in CT images via deep learning". In: *16th International Meeting on Fully Three-Dimensional Image Reconstruction in Radiology and Nuclear Medicine*. 2021.

[60] Cristobal Martinez, Claudia de Molina, Manuel Desco, and Monica Abella. "Optimization of a calibration phantom for quantitative radiography". In: *Medical Physics* 48.3 (2021), pp. 1039–1053.

[61] Rodney A Brooks and Giovanni Di Chiro. "Beam hardening in x-ray reconstructive tomography". In: *Physics in medicine & biology* 21.3 (1976), p. 390.

[62] Pengchong Jin, Charles A Bouman, and Ken D Sauer. "A model-based image reconstruction algorithm with simultaneous beam hardening correction for X-ray CT". In: *IEEE Transactions on Computational Imaging* 1.3 (2015), pp. 200–216.

[63] Tobias Würfl, Mathis Hoffmann, André Aichert, Andreas K Maier, Nicole Maaß, and Frank Dennerlein. "Calibration-free beam hardening reduction in x-ray CBCT using the epipolar consistency condition and physical constraints". In: *Medical physics* 46.12 (2019), e810–e822.

[64] Chye Hwang Yan, Robert T Whalen, Gary S Beaupre, Shin Yi Yen, and Sandy Napel. "Reconstruction algorithm for polychromatic CT imaging: application to beam hardening correction". In: *IEEE Transactions on medical imaging* 19.1 (2000), pp. 1–11.

[65] Zhou Li-ping, Sun Yi, Cheng Kai, and Yu Jian-qiao. "Deep Learning Based Beam Hardening Artifact Reduction in Industrial X-ray CT". In: *CT Theory and Applications* (2018), pp. 227–240.

[66] Robert E Alvarez and Albert Macovski. "Energy-selective reconstructions in x-ray computerised tomography". In: *Physics in Medicine & Biology* 21.5 (1976), p. 733.

[67] LA Lehmann et al. "Generalized image combinations in dual KVP digital radiography". In: *Medical physics* 8.5 (1981), pp. 659–667.

[68] J Heinzerling and M Schlindwein. "Non-linear techniques in multi-spectral x-ray imaging". In: *IEEE Transactions on Nuclear Science* 27.2 (1980), pp. 961–968.

[69] H Neale Cardinal and Aaron Fenster. "An accurate method for direct dual-energy calibration and decomposition". In: *Medical physics* 17.3 (1990), pp. 327–341.

[70] William R Brody, Glenn Butt, Anne Hall, and Albert Macovski. "A method for selective tissue and bone visualization using dual energy scanned projection radiography". In: *Medical physics* 8.3 (1981), pp. 353–357.

[71] Keh-Shih Chuang and HK Huang. "Comparison of four dual energy image decomposition methods". In: *Physics in Medicine & Biology* 33.4 (1988), p. 455.

[72] Bruce H Hasegawa et al. "Object-specific attenuation correction of SPECT with correlated dual-energy x-ray CT". In: *IEEE Transactions on Nuclear Science* 40.4 (1993), pp. 1242–1252.

[73] Jeffrey A Fessler. "Mean and variance of implicitly defined biased estimators (such as penalized maximum likelihood): Applications to tomography". In: *IEEE Transactions on Image Processing* 5.3 (1996), pp. 493–506.

[74] Jiang Hsieh, Robert C Molthen, Christopher A Dawson, and Roger H Johnson. "An iterative approach to the beam hardening correction in cone beam CT". In: *Medical physics* 27.1 (2000), pp. 23–29.

[75] Zongwei Zhou, Md Mahfuzur Rahman Siddiquee, Nima Tajbakhsh, and Jianming Liang. "Unet++: A nested u-net architecture for medical image segmentation". In: *Deep learning in medical image analysis and multimodal learning for clinical decision support*. Springer, 2018, pp. 3–11.

[76] Karen Simonyan and Andrew Zisserman. "Very deep convolutional networks for large-scale image recognition". In: *arXiv preprint arXiv:1409.1556* (2014).

[77] Diederik P Kingma and Jimmy Ba. "Adam: A method for stochastic optimization". In: *arXiv preprint arXiv:1412.6980* (2014).

[78] Mohamed M Zahra, Mohamed H Essai, and Ali R Abd Ellah. "Performance functions alternatives of MSE for neural networks learning". In: *International Journal of Engineering Research & Technology (IJERT)* 3.1 (2014), pp. 967–970.

[79] Belma Dogdas, David Stout, Arion F Chatziioannou, and Richard M Leahy. "Digimouse: a 3D whole body mouse atlas from CT and cryosection data". In: *Physics in medicine & biology* 52.3 (2007), p. 577.

[80] J Punnoose, J Xu, A Sisniega, W Zbijewski, and JH Siewerdsen. "spektr 3.0—A computational tool for x-ray spectrum modeling and analysis". In: *Medical physics* 43.8Part1 (2016), pp. 4711–4717.

[81] Lee A Feldkamp, Lloyd C Davis, and James W Kress. "Practical cone-beam algorithm". In: *Josa a* 1.6 (1984), pp. 612–619.

[82] Qingsong Yang et al. "Low-dose CT image denoising using a generative adversarial network with Wasserstein distance and perceptual loss". In: *IEEE transactions on medical imaging* 37.6 (2018), pp. 1348–1357.

[83] Hang Zhao, Orazio Gallo, Iuri Frosio, and Jan Kautz. "Loss functions for image restoration with neural networks". In: *IEEE Transactions on computational imaging* 3.1 (2016), pp. 47–57.

[84] Philip Stenner, Bernhard Schmidt, Thomas Allmendinger, Thomas Flohr, and Marc Kachelrie. "Dynamic iterative beam hardening correction (DIBHC) in myocardial perfusion imaging using contrast-enhanced computed tomography". In: *Investigative radiology* 45.6 (2010), pp. 314–323.

[85] Mitchell M Goodsitt. "Evaluation of a new set of calibration standards for the measurement of fat content via DPA and DXA". In: *Medical physics* 19.1 (1992), pp. 35–44.

[86] AK Jones, DE Hintenlang, and WE Bolch. "Tissue-equivalent materials for construction of tomographic dosimetry phantoms in pediatric radiology". In: *Medical physics* 30.8 (2003), pp. 2072–2081.

[87] DR White, RJ Martin, and R Darlison. "Epoxy resin based tissue substitutes". In: *The British journal of radiology* 50.599 (1977), pp. 814–821.